Bangor University

DOCTOR OF PHILOSOPHY

Controls on exchange in a subtropical tidal embayment, Maputo Bay

Lencart e Silva, Jaoa

Award date:
2007

Awarding institution:
University of Wales, Bangor

Link to publication

Controls on Exchange in a

Subtropical Tidal Embayment,

Maputo Bay

Dissertation submitted for the degree of PhD in physical

oceanography at the School of Ocean Sciences,

University of Wales, Bangor.

João D. A. A. Lencart e Silva, 2007

Para a Sara, o André e o Pedro

Abstract

Maputo Bay is a tidally-energetic, subtropical embayment in a region subjected to strong seasonal rainfall. Observational data are analysed alongside modelling outputs to explain the mechanisms controlling the physical environment inside Maputo Bay. Moored current meters, tide gauges and monthly bay-wide surveys were used to characterise the evolution of the density structure and flow field on seasonal, fortnightly and semi-diurnal time scales. The bay is subjected to large seasonal variations in freshwater input ($\sim 10 - 10^3$ m^3.s^{-1}) and pronounced fortnightly variations in tidal stirring power input ($\sim 10^{-3} - 1$ W.m^{-3}). During the dry season, the water column was found to be continuously, fully mixed, with weak horizontal density gradient and a residual circulation, which was mainly due to tidally-rectified currents. By contrast, during the wet season, freshwater buoyancy was observed to induce marked horizontal salinity gradient and stratification, which is pronounced around the time of neap tides. This stratification is largely eroded at spring tides but semi-diurnal periodic stratification, a sum of local production and advection from offshore, was still apparent. A simple potential energy anomaly model shows that the local stratification terms were tidal straining and estuarine circulation. The flushing time of the Bay is investigated using the observed bay averaged salinity and a modified tidal prism model, estimating the wet season mean between 9 and 17 days depending on the retention coefficient used. A series of experiments with a high resolution 3d model of the bay show that an initial increase in tidal currents, during a period of significant freshwater input, decreased the efficiency of the density driven circulation thus increasing flushing time. Under high runoff and tides, both forcing mechanisms collaborated to decrease flushing time. Depending on the variation of these two parameters, the 3d model predicted a flushing time minimum of 35 days and a maximum of 160 days. The main control of exchange during the dry season is tidal forcing mainly through rectified currents that increase in direct proportion to tidal range. During the wet season, tidal forcing and estuarine circulation generate a neap to spring cycle of the efficiency of exchange, which decreases with the amount of tidal forcing.

Acknowledgements

Institutional acknowledgements

People

My warmest thanks to:

- John H. Simpson for keeping me in bounds of science facts and away from science fiction with its thorough and dedicated supervision and for the

formulation of the diffuse box model in Section 8.3;

Table of contents

Table of contents

List of Figures

List of Tables

1 Introduction

1.1 Background and motivation

Coastal systems where freshwater is input in a monsoon-like regime are characteristic features of semi-arid subtropical latitudes. In such systems, a sudden increase in rainfall induces large river runoff and creates the conditions for a change in circulation patterns. Sub-tropical monsoonal regimes of this kind have seldom been the object of physical oceanographic studies, which have tended to concentrate on mid-latitude locations which are more accessible and easier to study from a logistical point of view. Freshwater inflow in mid-latitude tidal embayments and large plain estuaries tends to be rather regular partly because of a climate with less seasonally variable rainfall and in some cases because of engineering controls in the rivers.

A system with a marked seasonal variability in freshwater supply and subjected to a wide range of tidal stirring constitutes a good observational testing ground for the theories of buoyancy-stirring interaction and the control of exchange characteristics of estuaries and Regions of Freshwater Influence, ROFIs (Simpson, 1997). The exchange resulting from the interaction between a horizontal density gradient and stirring has been studied, for example, in a series of laboratory experiments by Linden and Simpson (1988). These authors showed how vertical mixing inhibits the development of density currents and that when mixing is switched on and off for equal times, the exchange through a cross-gradient section increases with the period of the mixing cycles. Maputo Bay possesses the attributes by being a tidal energetic embayment subjected to large seasonal freshwater and tidal variations.

The city of Maputo is Mozambique's capital city and is built on the margins of Maputo Bay. Its population of about one million people uses the bay's water for waste disposal, and mangrove firewood production. The bay is also host to a number of

industries including the production of aluminium ingots and salt harvesting. The port of Maputo is of regional importance and the bay supports a substantial semi-industrial fishery. These activities have considerable areas of conflict in terms of water uses and sustainability. Without a thorough characterisation of the exchange between bay and shelf, no robust insight can be developed as to the persistence within the bay of pollutants from domestic and industrial waste disposal. As well as being vulnerable to adverse effects from pollutants, it has been postulated that sustainability of the fishing and the maintenance of the mangrove ecosystem are dependant on a minimum freshwater supply to the bay.

The ecosystem dependence on freshwater was the principal focus of study of the Catchment2Coast project within which this dissertation is rooted. This European Union funded programme aimed at improving the scientific knowledge concerning the link between the river catchments' hydrology and the response of the fish catch in Maputo Bay, targeting specifically the economically important shrimp *Penaeus Indicus*.

Prior to the Catchement2Coast project, the only physical studies of the bay concerned mainly its tidal character. Observational work was undertaken by Saide (1995) and Hoguane et. al,(1999) for 3 months mainly during the dry season. Additionally, some episodic density surveys were performed at the time of the year 2000 catastrophic floods. A 2-dimensional model of the bay, calibrated from the tidal survey data, was developed by Hidroprojecto Engenharia e Gestão, S. A. and the Instituto de Investigação Pesqueira (IIP) with the results presented in IIP (2001). To understand fully the exchange regime in the bay, data had to be collected for a full hydrological year and analysed in its semi-diurnal, subtidal, seasonal and event scale frequencies.

1.2   Problem definition

Forcing by tidal action in Maputo Bay increases markedly from neap (range ~0.5 m)

to spring tide (range ~3 m) with corresponding changes in the energetic tidal currents. Freshwater flow can be nearly absent in the dry season, peaking abruptly from virtually no flow to ~10^3 m^{3}s^{-1} following intensive rains in the winter season The bathymetry in the bay changes rapidly from the mouth (depth ~ 30 m) to the inner bay (depth <5m) and shows a marked cross-bay depth gradient at the outer bay (Figure 2:2, page 7). The bay is on the margin of the monsoonal regime with expected large variations of atmospheric pressure and high winds. The bay's oceanographic context is complex as it is situated between the Agulhas Current and the Mozambique Channel eddy system.

In this context, the candidate exchange controls are postulated to be:

- tidal shear diffusion from the interaction between the tidal velocity vertical profile and the distribution of the property being diffused;

- residual currents from the interaction between tides and the shoaling bathymetry;

- residual currents from density gradients set either by surface heating or by river runoff;

- residual currents from slopes imposed remotely either by along-shore winds or by variability in the off-shore current and eddy structures.

Does a subset of these candidate controls prevail over the rest? Is there a marked seasonal cycle in the characteristics of the bay-shelf exchange? Is the density field controlled mainly by the seasonal heat or freshwater cycles or both? How persistent is stratification and what is its influence on exchange? How does tidal action interact with the density field to influence exchange between the bay and the adjacent shelf?

These questions are contained in the aim of this dissertation, which is to determine the predominant controls of exchange between Maputo Bay and the adjacent shelf at tidal,

subtidal, and seasonal frequencies.

1.3 Research activity and reporting

To answer the questions posed above, an observational programme was designed to monitor the density field, currents and sea surface elevation. Throughout this dissertation, the observational results were analysed in search of responses to changes in atmospheric and hydrological conditions.

The uncertainties in successfully completing an observational campaign are considerable in developing countries such as the present day Mozambique which is in the process of developing a basic scientific infra-structure. Hardware (i.e. vessels, instrumentation, mooring apparatus, land vehicles, construction materials, fuel, etc.) and human resources (technicians, boat crews, divers and research personnel) are overcommitted or non-existent. In addition, the heavily bureaucratic nature of the relations between institutions makes it very hard to perform simple tasks such as obtaining historical and ancillary data or importing an instrument from abroad.

With the aim of developing a locally coordinated campaign management, the author established a programme of observational work skills transfer to personnel of the two Mozambican institutions involved: UEM (Universidade Eduardo Mondlane) and IIP. The training included: i) an introduction to the instrumentation used; ii) instruction on the design and implementation of a sampling routine; iii) implementation of a data archive structure and training in the calibration of instruments and position finding procedures. Furthermore, during the 6 months spent on-site, the author participated actively in the sampling programme by coordinating the CTD survey team in several initial bay wide campaigns and by coordinating and participating in the deployment of both tide gauge units.

Despite these efforts, the outcome of the observational campaign was short of what

was expected and data were insufficient, on their own, to provide the answers needed. To overcome these limitations, the modelling programme of the Catchment2Coast project was expanded and a number of dedicated modelling experiments were undertaken. This aspect of the study involved a state-of-the-art 3-dimensional numerical modelling platform which was used to provide a fuller picture of the behaviour of the bay, in regions and at times where no observations were available. In addition, a set of schematic models were used to analyse specific features of the bay's dynamics.

This dissertation starts by presenting Maputo Bay's in its context and by describing the observational and numerical modelling methods used. In Chapter 5, the responses of the currents and sea surface elevation at tidal and subtidal frequencies are analysed, relating them to tidal, atmospheric and hydrologic forcing. In Chapter 6, the seasonal cycles of salinity, temperature and density structure are related to forcing by heat and freshwater. In Chapter 7, tides and buoyancy are analysed together and the mechanisms leading to the observed density structure identified. In Chapter 8, a measure of the renovation capability of the water in Maputo Bay is calculated. Here, several modelling strategies are utilised to determine the dependence of system's flushing on the main controls on exchange identified in the previous chapters. Finally, the results are discussed to determine the dry and wet season main controls on exchange and the results of their interaction at seasonal, fortnightly and semidiurnal frequencies.

2 Maputo Bay

2.1 Site description
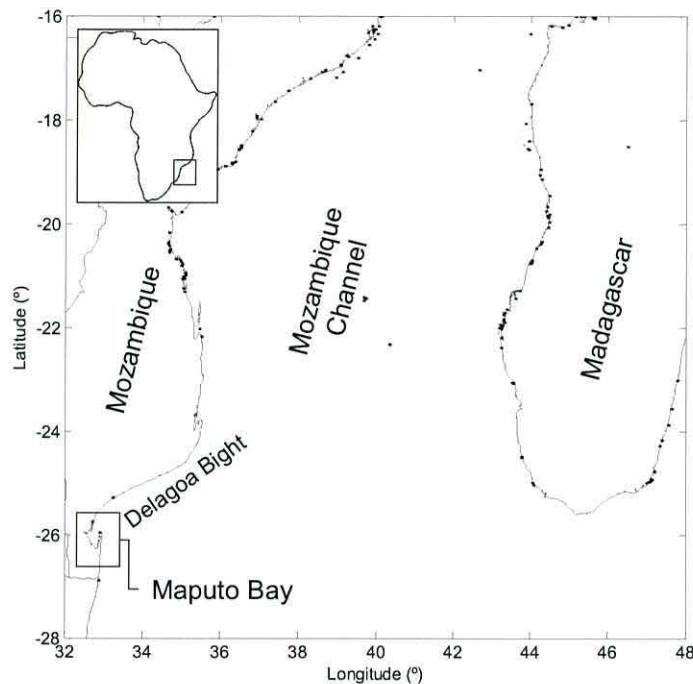
Figure 2:1 – Position of Maputo bay within Africa and in the Mozambique Channel context.

Maputo Bay is a tidally energetic embayment located in the south of Mozambique with its centre at 32° 47'E, 26° 03'S (Figure 2:2). Its bathymetry is shallow with an average of ~5 m reaching ~30 m at the ocean boundary. The bay opens to the shelf through an 18 km wide inlet, spanning from the Macaneta sand spit on the northwest side to Ilha dos Portugueses on the southeast side.
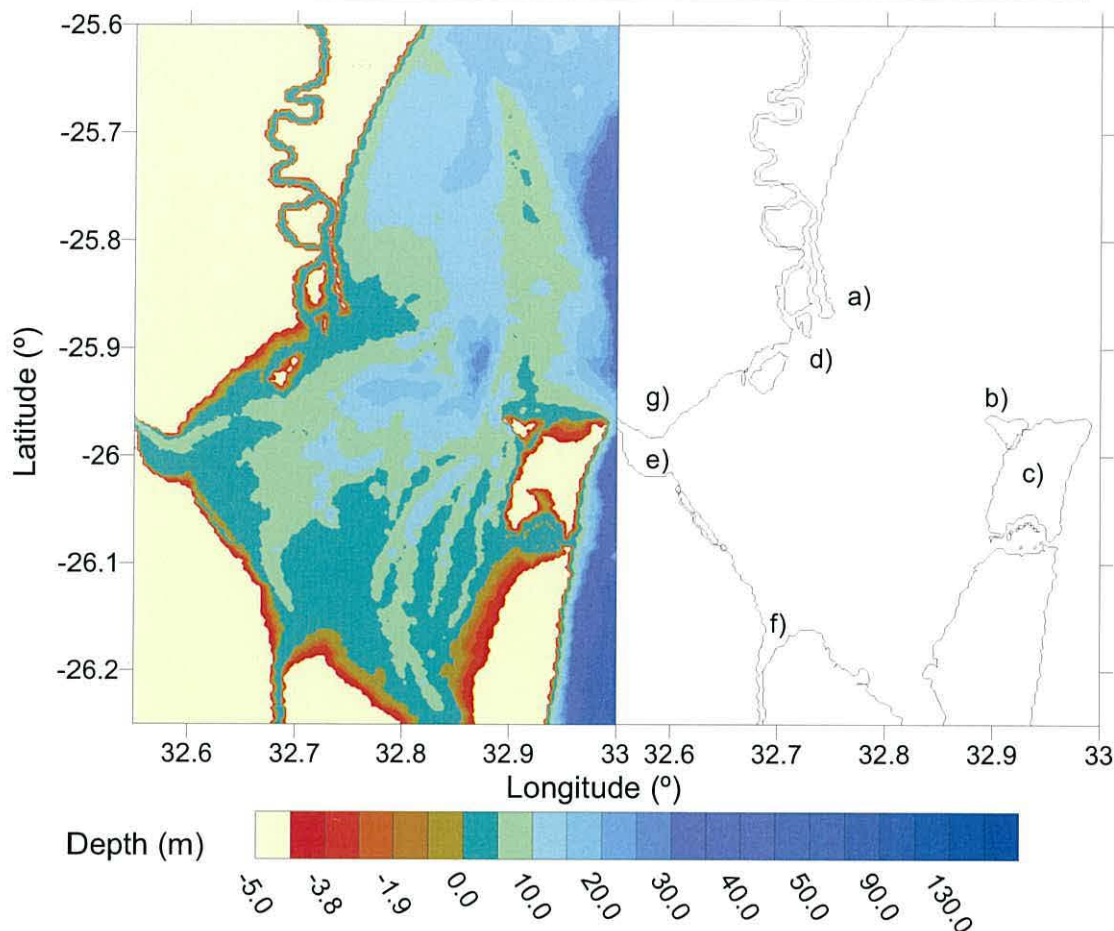
Figure 2:2 – Bathymetry and overview of Maputo Bay's main features: a) Macaneta sand spit; b) Ilha dos Portugueses; c) Inhaca Island; d) Incomati river mouth; e) Umbeluzi river mouth; f) Maputo river mouth; g) city of Maputo.

According to Mussa *et. al.* (2003), Maputo Bay evolved from the interaction between the Maputo River delta and the tidal inlet north of it. The bay opened to the shelf when sea level rose to 20 m below present level around 8000 – 9000 years BP. The channels still visible today in the bay's bathymetry were formed from the interaction between tides and an estuarine system. Tidal action and Aeolian deposition formed a barrier island, the precursor of the present day Inhaca, thus protecting the river delta from the shelf. The sea level rise to present level around 5000 – 7000 years BP drowned this tidal estuarine system, creating the today's bathymetric layout. In terms of present day morphodynamics, Cooper and Pilkey (2002) note that the current bathymetry shows an extensive flood-tidal delta and a very small ebb-tidal delta, hinting at a possible flood dominant transport.

The bathymetry in Figure 2:2, results from a compilation of surveys and independent

ship soundings ranging from the nineteen-sixties through to the nineteen-eighties. Two different regions can be observed in Maputo Bay: south and west mudflats lead to high water column turbidity (Secchi depth less than 0.2 m); to the northeast a sandy bottom leads to low water column turbidity (Secchi depth greater than 15 m) and seagrass cover (de Boer, 2000). The shores are either sandy beaches near populated areas or mangrove patches in different stages of conservation (de Boer, 2002).

Maputo Bay is subject to impacts from several types of anthropogenic activities. The greater Maputo area houses approximately 1 million people in the cities of Maputo and Matola (FCO Foreign and Commonwealth office, 2007). Their main impacts in the bay are through wastewater disposal, artisanal fishing and mangrove cutting for firewood.

Several industrial and semi-industrial activities are linked to the bay: with an expected capacity of 10^7 tons.year^{-1} in 2011, Maputo Port exchanged in 2007 6.7×10^6 tons of cargo (Roberts, 2007) and the heavy aluminium smelter, Mozal, produces 5.8×10^5 tons.year^{-1}, exporting ingots mainly to Europe (BHP Billiton Aluminium, 2007).

The bay is subjected to significant fishing effort with an average 3000 tons.year^{-1} of catch taking only shrimp fishing into account (Monteiro and Mathews, 2003). Additionally, intensive salt farming occurs in the intertidal flats between the Maputo and Umbeluzi river mouths.

2.2   Freshwater inputs

Maputo Bay receives water from 3 catchments: Incomati, Maputo and Umbeluzi. These are represented in Figure 2:3. The Incomati and Maputo have large catchments while the Umbeluzi encompasses a relatively small area. In terms of the regularisation of the flow, the Incomati has the most dams with 2060 Mm^3 storage, followed by the Maputo and the Umbeluzi (Vaz and Zaag, 2003). The same study estimates that the

Incomati has an average yearly flow of 3587 $Mm^3.y^{-1}$ 50% of which is extracted for agriculture and exotic timber production. The volume of water extracted from the basin has been rising. The peak discharge of the Incomati at the South African – Mozambican border was reduced by half between 1953-1979 and 1980-1999. This study also notes that the Incomati's inter-annual variation in flow can reach values between 50-65 % on average. Historical data shows that, during the wet season, the mean flow in the Incomati was 80.69 $m^3.s^{-1}$ with a recorded maximum 6827 $m^3.s^{-1}$ during the catastrophic floods of 2000.
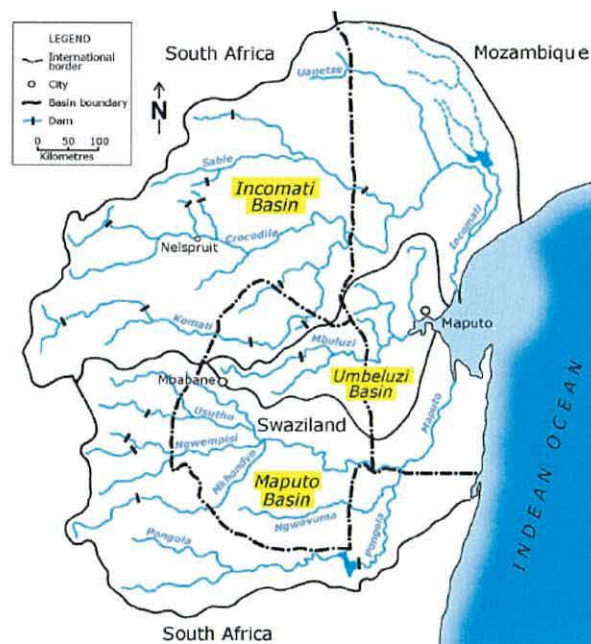
Figure 2:3 – Catchments draining into Maputo Bay (Vaz and Zaag, 2003).

The top panel of Figure 2:4 represents the flow into the bay from each of the basins in terms of available flow entering the bay, calculated for the full available record (**Table 2:1**). There is a marked seasonality, with most of the flow concentrated in the period from October to April.
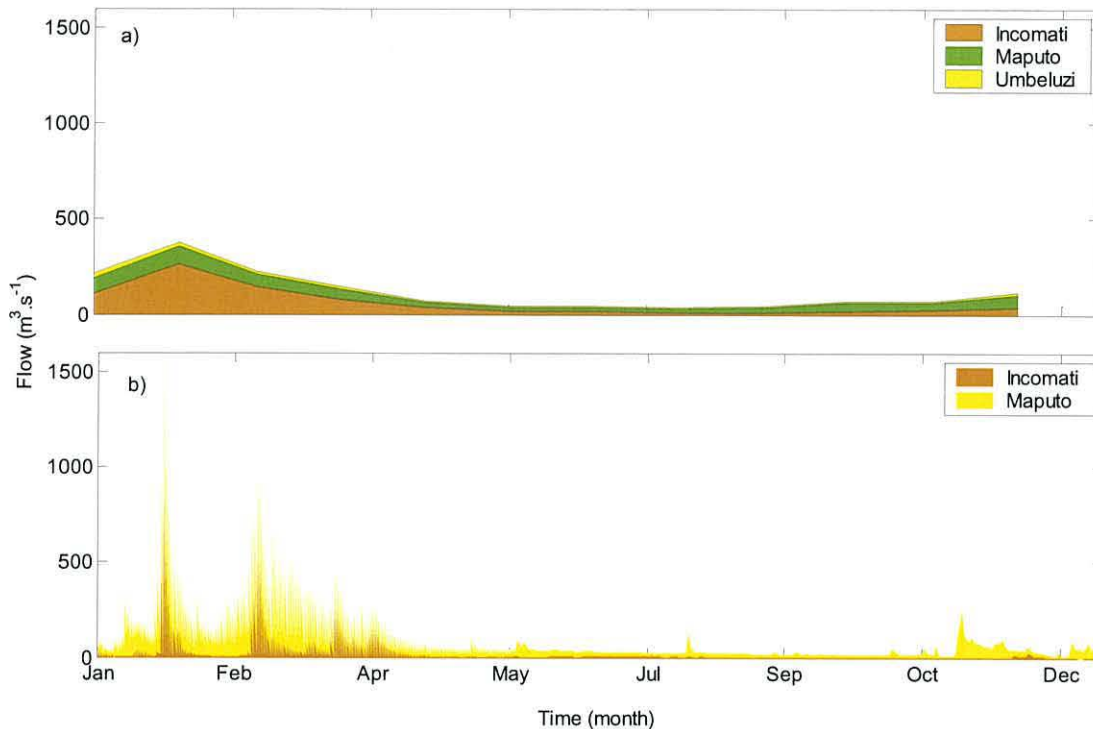
Figure 2:4 – Seasonal river discharge in Maputo Bay. The contributions of the Incomati, Maputo and Umbeluzi basins are stacked with the upper line representing the bay-wide cumulative discharge: a) observed historical monthly averages; b) discharge from January 2003 to May 2004 (observed Incomati discharge in orange and modelled Maputo discharge in yellow).

The Incomati flow during the period in which this study took place is shown in the bottom panel of Figure 2:4.

Considering the wettest months, from October to April, the last 26 years the Incomati registered a mean flow of 79 $m^3.s^{-1}$. During the same months, in 2003-2004 the mean for the Incomati flow was 39 $m^3.s^{-1}$.

During the same hydrological year, the average dry season flow was 6 $m^3.s^{-1}$ and the maximum observed peak discharge was 1076 $m^3.s^{-1}$. It is important to note that the first freshwater discharge in the wet season led to a rise of the flow from 3 to 1076 $m^3.s^{-1}$ in only 4 days with the episode lasting only 3 days. This illustrates the pulse-like character of the inflow of freshwater which reaches the bay in large quantities for very brief periods.

Table 2:1 – **Data availability for each of the catchments that drain into Maputo Bay.**

	Available Period	Frequency
Incomati	1979 - 2005	Daily
	1953 - 2005	Monthly
Maputo	1964 - 1983	Daily
	1995 - 2003	Daily
Umbeluzi	1989 - 2003	Daily

The only available data for Maputo River for the period of relevance were synthesised by the University of Natal from historical records. This is presented in Figure 2:4 bottom. In comparison with the Incomati, the Maputo River is depicted to have lower peak flow (521 against 1076 $m^3.s^{-1}$) and to be smoother throughout the wet season with less marked pulse discharges.

2.3   Regional oceanographic context

2.3.1 Mozambique Channel

Maputo Bay connects at its mouth with the Delagoa Bight situated on western margin of the Mozambique Channel (Figure 2:1).

The classical view of the currents around the Mozambique Channel was that the South Equatorial Current (SEC) at 15°S would branch when reaching Madagascar. This would produce a North Madagascar Current (NMC) of ~ 30 Sv which would flow south through the channel to form the Mozambique Current (MC) (Swallow et al., 1988). The south branch of the SEC (~20 Sv) would flow around Cape St Marie, at the southern tip of Madagascar, and head southwest to form the Agulhas Current (AC). According to Quartly and Srokosz (2004), the perception of a permanent Mozambique Current has changed and the low variability scenario has been replaced by a more time and spatially variable configuration, in the form of a train of anticyclonic eddies (Figure 2:5).
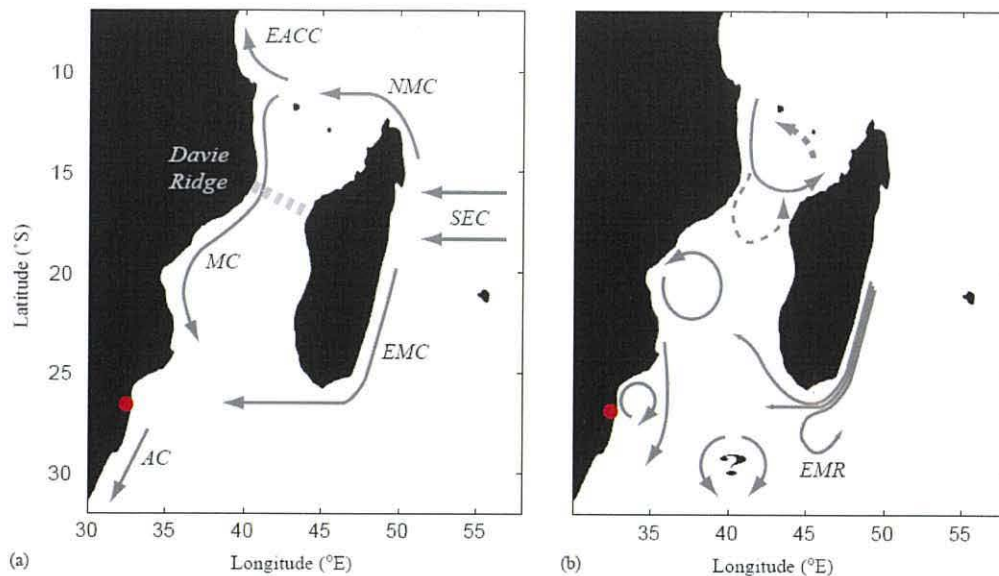
Figure 2:5 - Circulation around Madagascar, adapted from Quartly and Srokosz (2004). Maputo Bay is signalled in red. a) Classical perception of long-term mean flow derived from wind forcing and mean water properties.(b) Present day perception of the Variability in features: SEC—South Equatorial Current, NMC—North Madagascar Current, EACC—East African Coastal Current, EMC—East Madagascar Current, MC—Mozambique Current, AC—Agulhas Current, EMR East Madagascar Retroflection.

It is of special relevance that Lutjeharms and Jorge da Silva (1988) report a permanent cyclonic eddy just outside Maputo Bay in the Delagoa Bight. This feature was observed consistently around 33.5° E from 1957 to 1980 and again identified in 1987 by Grundlingh *et. al.* (1991), which measured its maximum sea level depression of 100 cm, decreasing rapidly to 12 cm from October to December 1987. The Delagoa Bight eddy was again observed between 1998 and 2003, by Quartly and Srokosz (2004) which argue that its position and intensity is controlled on its eastern boundary by the passage of large anticyclonic eddies on southwest migration from their origin at Cape St. Marie. Lutjeharms and Jorge da Silva (1988) calculate currents of ~ 15 cm.s^{-1} flowing southeast of the eddy core and a returning north current between the eddy and the coast. Despite the profuse evidence of this feature, the literature shows insipient dynamical arguments for its existence and stability.

2.3.2 Tidal forcing

Maputo Bay is subjected to a strong semidiurnal tide with marked spring to neaps ratio (Canhanga and Dias, 2005; Hoguane *et. al.*, 1999). Currents inside the bay range

from 0.15 m.s^{-1} in neap tide to 1 m.s^{-1} in spring tide (Saide, 1995) and tidal analysis of the historical surface elevation done by Canhanga and Dias (2005) show a minimum range of 0.2 m and a maximum of 3.8 m. with a tide form factor of $F = 0.25$ where:

Equation 2:1
$$F = \frac{O_1 + K_1}{M_2 + S_2},$$

and O_1, K_1, M_2, and S_2 are the constituent amplitudes in metres (Pugh, 1987). This value of the form factor indicates a strong semidiurnal character of the tide. Both Hoguane *et. al.* (1999), using observations, and Canhanga and Dias (2005), using numerical modelling results, find that the tide propagates along the axis normal to the mouth of the bay, with no significant lag between the west and east margins.

2.3.3 Offshore salinity and temperature

Salinity and temperature offshore Maputo Bay is described in Sete *et. al.* (2002) using a compilation of the available cruise data between 1977 and 1980 summarised in **Table 2:2**.

Temperature is shown to have a clear annual cycle warming from winter to summer and vice-versa. On the other hand, salinity has a very small degree of variation and the season mean values cannot be considered statistically different or otherwise since there was no mention of the number of degrees of freedom in the dataset. The seasonal variation in the depth of the mixed layer shows a shallower pycnocline during the spring and summer months but as in the salinity data, the statistic validity of this trend is unknown.

Table 2:2 – **Temperature, salinity and Mixed layer depth adapted from Sete *et. al.* (2002)**

	Period	Value
Surface Temperature (°C)	Jan-Feb-Mar	26-29
	Apr-May-Jun	24-25
	Jul-Aug-Sep	22-25
	Oct-Nov-Dec	25-27
Surface Salinity (PSU)	Jan-Feb-Mar	34.4-35.2
	Apr-May-Jun	35.0-35.5
	Jul-Aug-Sep	35.2-35.5
	Oct-Nov-Dec	35.3-35.5
Mixed Layer Depth (m)	Jan-Feb-Mar	30-80
	Apr-May-Jun	50-100
	Jul-Aug-Sep	30-120
	Oct-Nov-Dec	20-80

2.4 Atmospheric input

Previous studies describe the bay's climate as part tropical part subtropical, influenced by the SE trade winds and northerly monsoons, but also occasionally by strong and cold SW winds or cyclones from the NE (de Boer et al., 2000). The seasonal incidence and variation of these regimes were not detailed in the literature available.

The winter (April to September) is usually cool and dry, while the summer (October to March) is warm and rainy. The mean daily air temperature varies from 17 to 27 °C (Hoguane, 1996) and the mean annual rainfall is 884 mm (de Boer et al., 2000).

2.4.1 Wind

The wind dataset was acquired from Mavalene International Airport weather station. These data spans from 01/03/2003 to 01/04/2004 with an hourly sampling frequency and 22.5 ° precision in the wind direction. The average wind speed for this period was ~ 4 m.s^{-1} and the wind speed never goes above 15 m.s^{-1}.

The rose plot of the wind in Figure 2:6 shows the number of data points falling within 22.5° wide bins. The main direction of wind is northward, but cross-shore (W-E) and along-bay (SSW-NNE) winds are also relevant. With regard to the spectral distribution of the signal, the left panel of Figure 2:6 shows that much of the energy lies in the subtidal frequencies and the most significant peak is at 1 cpd. No seasonal trend emerges from the analysis of the filtered wind data (Figure 2:6, c)
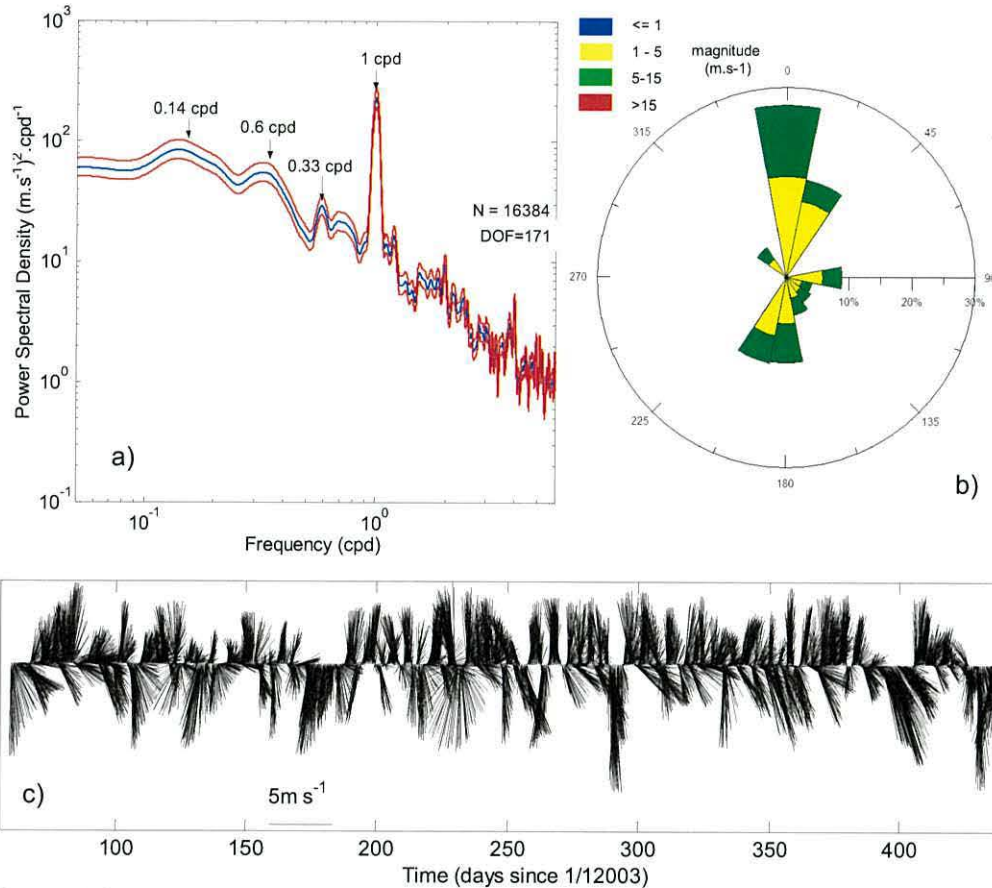
Figure 2:6 – Local wind from Mavalene International Airport (Maputo): a) power spectral density of wind magnitude (red line indicates 95% confidence interval; b) wind direction and magnitude rose plot in ° from North; c) diurnal wind vector.

2.4.2 Air temperature, radiant heat flux and atmospheric pressure

Figure 2:7 top panel shows the air temperature measured in Mavalene International Airport, Maputo. Between 01/03/2003 and 01/04/2004, the mean temperature reached a plateau of ~ 25 °C, decreasing to its lower values in July where a 10.5 °C minimum was recorded. The maximum recorded temperature for the whole period was 41.3 °C.

The middle panel of Figure 2:7 shows the radiant heat budget for the offshore cell of the NCEP model centred on 33.75 E , 25.71 S, (Kalnay *et. al.*, 1996). This budget is composed of the net long and shortwave radiation flux across the atmosphere-ocean interface. The sensible and latent heat components of the overall heat budget were omitted due to their dependence on water temperature and heat storage capacity. When compared to the radiant heat cycle, the recorded air temperature lags 8 days approximately.
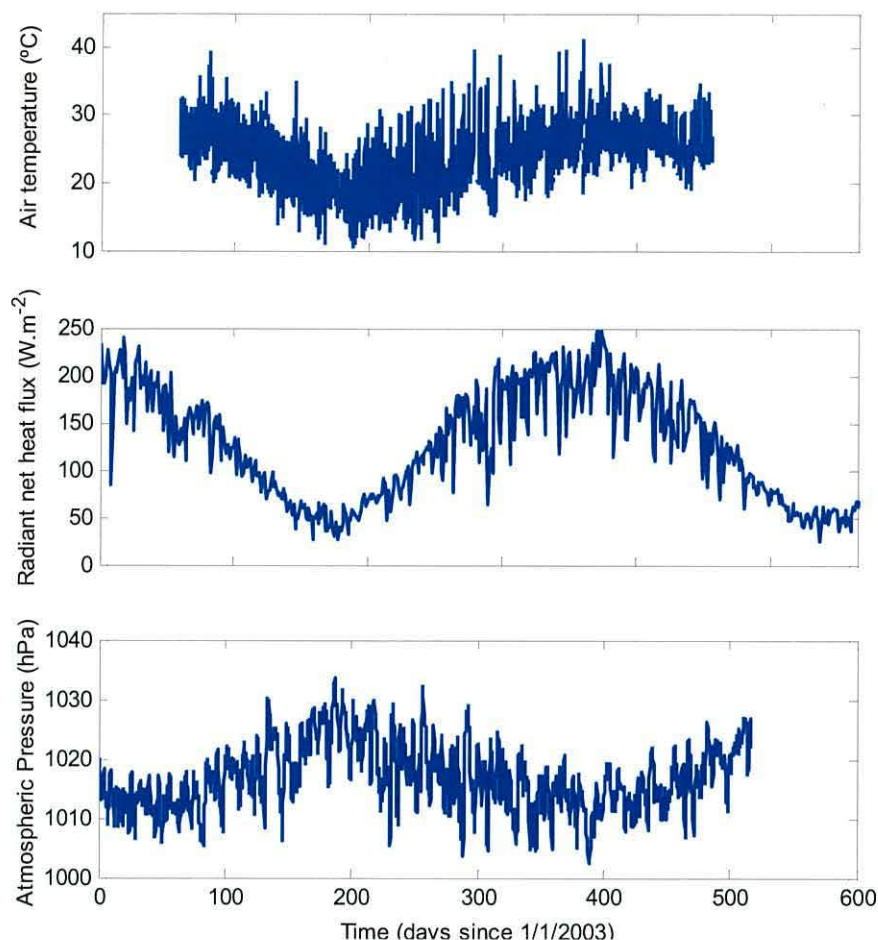
Figure 2:7 – Temperature, radiant heat budget and atmospheric pressure (daily means): upper panel: air temperature measured at the Mavalene International Airport; middle panel: radiant heat budget – longwave + shortwave net flux across the atmosphere-ocean boundary NCEP reanalysis data; lower panel: regional atmospheric pressure from NCEP reanalysis data.

The regional atmospheric pressure is plotted on the lower panel of Figure 2:7 . This data is a result of the averaging of the NCEP reanalysis data for the range between 32.5 – 35 E, 25 – 27.5 S. The atmospheric pressure mirrors closely the heat input, reaching its lowest point during the summer months and its highest during winter.

During the wet season, the atmospheric pressure and freshwater flow were correlated between -0.20 to -0.38 for a 95% confidence interval. For the full record, wind speed and atmospheric pressure showed a low correlation of -0.01 to 0.08 for a 95% confidence interval.

3 Observational programme

3.1 Planning

The aim of the observational programme was to investigate the flow regime of the bay and its exchange with the shelf over a full hydrological year. The objectives were to define the tidal contributions to the bay's flow regime, the density driven circulation, and how these two terms interacted on the seasonal, fortnightly and semidiurnal timescales. This required a good handle on: i) the tidal and residual currents; ii) the evolution of the density field; iii) the sea surface elevation.

The operations were scheduled to start in March 2003 and to carry on for fifteen months until May 2004. The planning and implementation of the programme was made in cooperation with the Universidade Eduardo Mondlane (UEM) and the Mozambican Fisheries Institute (IIP). All instrumentation was provided by UEM with the exception of one Aanderaa RCM9 unit which was kindly supplied by the Mozambican Hydrographic Institute (INAHINA).

In view of the anticipated limited number of instruments available, five mooring stations were planned to run for the full observational period each carrying two RCM9 current meters, one placed near the bottom and the other as close to the surface as possible. Initially it was planned to service the moorings every two weeks in order to minimise bio-fouling effects. In fact, the once the effective number of operating current meters was known only two moorings were scheduled to be deployed as depicted in Figure 3:1. Each of the RCM9 units measured current magnitude, current direction, temperature, pressure and conductivity.
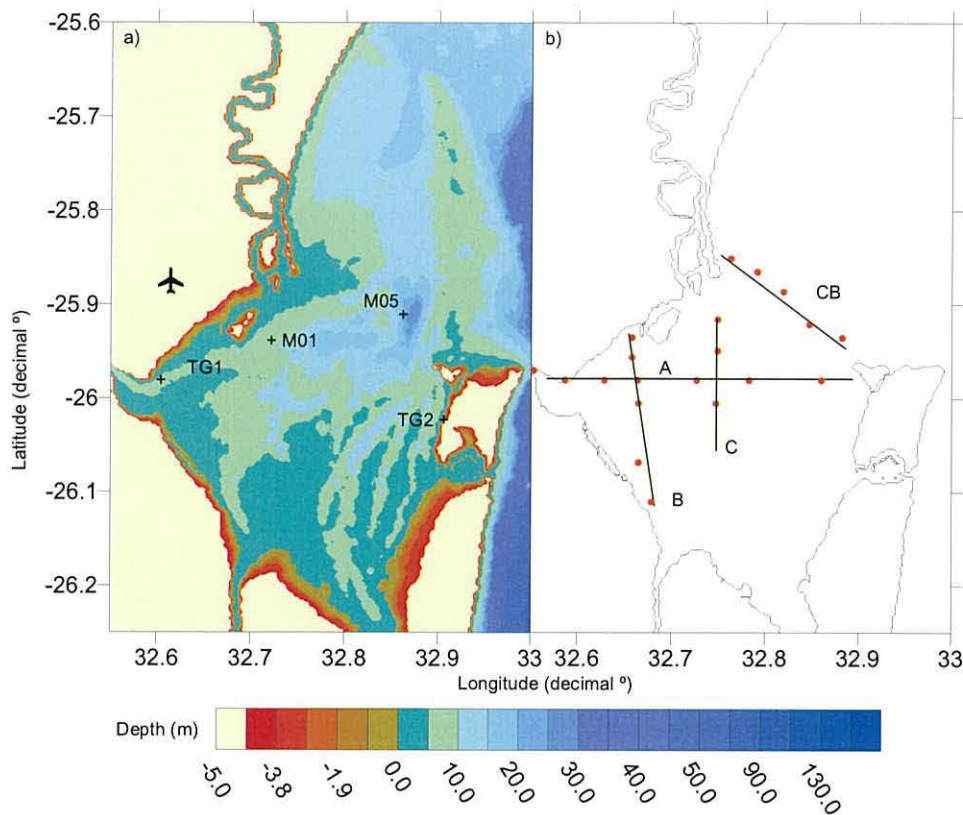
Figure 3:1 – Bathymetry and observational layout: a) Maputo Bay's Bathymetry and long term sampling site, where TG indicates tide gauge, M indicates RCM9 mooring and the airport sign points the weather station at Mavalene International Airport; b) CTD sampling grid sections with red dots indicating the profiling stations.

Two Hydrotide Recording Gauges (HTRG) were scheduled to be deployed during the same period at locations TG1 and TG2. From these deployments information was expected regarding: i) the tidal characteristics of the bay; ii) the subtidal bay surface elevation cycle; and iii) the subtidal slope between each TG1 and TG2.

Four CTD (Current Temperature and Density) sampling sections with a total of 20 stations covering most of the bay, were scheduled for sampling once every three weeks in order to provide horizontal coverage of the density field and improve on the vertical resolution of the RCM9 mooring stations during both neap and spring tides. The sampled sections are plotted in Figure 3:1 b).

In order to define the forcing mechanisms, the acquisition of the following data was planned for the deployment period: i) meteorological data from Inhaca Island and the Mavalene International Airport; ii) and river flow for the Incomati, Umbeluzi and Maputo rivers.

3.2   Implementation

The CTD campaigns were accomplished with minor complications. The mooring operations and tide gauge deployments proved more difficult with substantial bureaucratic delays in the acquisition of the current meters and tide gauges, which resulted in a deferred start to the mooring programme. Mooring vandalism led to instrument and data loss and limited availability of technical personnel hampered the continued operation of all four long-term instrument sites. The planned and implemented sampling programmes are schematised in Table 3:1 and Table 3:2 (pages 24 and 25). Station locations are presented in Annex 1 and instrument specifications in Annex 2.

3.2.1   CTD sampling

In order to maintain consistency in relation to the tidal cycle, the same route through the sampling stations was used in each survey, with the run starting one hour before high water to perform the cross-bay sections A and CB during slack water. Due to personnel shortage and boat availability, the 3-week target of bay wide sampling was reduced to a monthly survey effort when possible.

The casts were performed with a SBE19 plus Seabird CTD (Conductivity Temperature Depth) profiler, hand lowered from a 7 m long powerboat. The campaigns started just after the instrument was returned from servicing and calibration by the manufacturers. Re-calibration in Maputo was impossible due to the unavailability of a salinometer.

3.2.2   Tide gauges

Two HydroTide Recording Gauges (HTRG) were deployed at Clube Naval pier and in front of the Inhaca Biology Station, TG1 and TG2, respectively in Figure 3:1 a.

The tide gauges were pre-calibrated by the manufacturer so that only an adjustment in the working density was needed to transform the pre-calibration for freshwater to the

conditions expected in Maputo Bay.

The HTRG is a vented pressure gauge, which measures pressure relative to atmospheric pressure using a hose connection to the atmosphere. For this reason, the instrument housing is usually deployed in dry land or on a fixed platform. Whilst the TG1 deployment was made on a permanent structure, for the TG2 site a tower made of scaffolding tubes and concrete base was planned to hold the HRTG recording unit. Due to the unavailability of materials, an executive decision was made to install the TG2 unit on a mooring pole approximately 1.5 m above high-water springs. Logistic constraints led to the delay of the tower deployment, and although the mooring pole held the recording unit dry for the first 139 days of sampling, it eventually collapsed and the pressure sensor was damaged.

The tower was finally deployed in March 2004 but the TG2 position was not equipped with an HTRG since it was easier to operate the only working unit from TG1.

3.2.3 Moorings

The moorings in Figure 3:3 were designed with subsurface buoys to minimise vandalism and accidental trawling. Even so, in the first deployment at M01 the mooring was vandalized shortly after the deployment with the loss of one current meter and floatation gear causing a hiatus of 3 months in the overall mooring programme. Subsequent vandalism at the same mooring resulted in the early suspension of the operations at M01.

The Data Storing Unit clocks were synchronised with an UTC standard prior to deployment and after recovery the difference from that standard was logged. CTD casts were performed prior to and after deployment and at each servicing when the fouling was removed from the instrument and the conductivity sensor carefully cleaned. Again, due to limited personnel availability, servicing of the moorings were also cut down to monthly visits when possible.

The overall quality of data varied according to the parameter measured. Current speed, direction, temperature and pressure were of generally good quality despite some timing discrepancies in the August 2003 deployment. As for conductivity, the records were of limited value. The settlement of biota rendered the conductivity signal useless after approximately 5 to 8 days in the water at M01 and 15 to 20 days at M05. This bio-fouling reduces the cross-sectional area of the conductivity ring mounted on the RCM9 leading to the underestimation of conductivity. Furthermore, most of the data from calibration casts were misplaced during the archiving process. In this way, the attempts to calibrate the data were made resorting to the regular bay-wide CTD campaigns closer to the deployment dates and sites.

Attempts were made to salvage as much as possible from the conductivity data. The M01 signal was beyond repair. Regarding the M05 mooring, the available CTD casts were used to correct the less damaged records. Figure 3:2 shows the full M05 salinity signal after applying the UNESCO (1981) algorithm top sensor conductivity and temperature. Alongside, the figure shows CTD casts and the final salvaged dataset. The first deployment, in red, was corrected using the slope between CTD casts to interpolate linearly the observed error. The second deployment, in green, had to be substantially truncated. Although a fall in salinity as observed in the second deployment was to be expected at a neap tide after significant freshwater flow, there was no CTD calibration casts during this period in order to confirm the trend. Hence, the second deployment was considered invalid since the beginning of the salinity fall. Similar corrections were applied to the bottom current meter. There were no significant errors during the third deployment and the sensor seemed to respond well between neap and spring tide conditions.
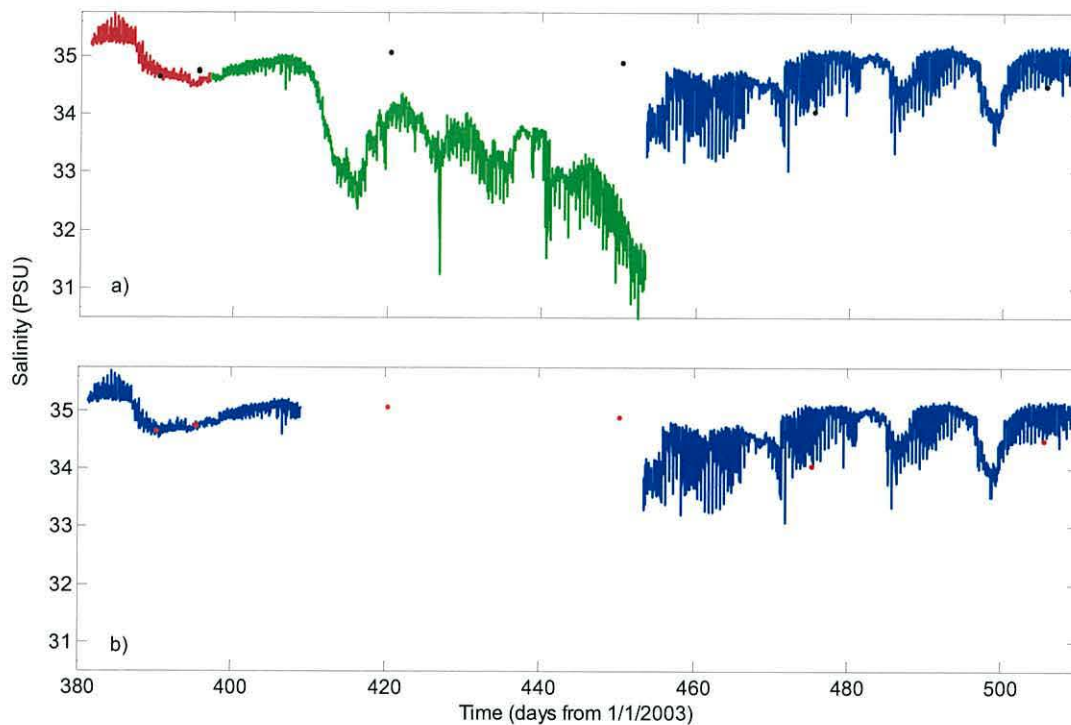
Figure 3:2 – Correction of the salinity signal at M05 top RCM9 unit: a) raw signal with colours separating each deployment and the black dots marking the available CTD results during the deployment period; b) corrected signal with CTD results marked in red.

Errors in the timing of the August 2003 deployment at M05 were corrected by matching the pressure signal to the pressure record at TG2 and linearly interpolating the gaps in the data.

3.2.4 Auxiliary data

Several problems were encountered when pursuing the acquisition of the meteorological and hydrological data: i) the Inhaca Island weather station was out of commission during the period of observational work; ii)the only remaining met station at Mavelene airport failed to provide consistent atmospheric pressure data; iii) and despite many attempts it was impossible to acquire Maputo and Umbeluzi river flow data for the period of interest. NCEP model reanalysis data was used to substitute the atmospheric pressure absent from the Mavalene dataset.

M01   M05

MSL: 10.9 m   MSL: 20.3 m

Subsurface floater

RCM9: 7 m   RCM9: 14 m

Subsurface floater

RCM9: 1.5 m   RCM9: 2.5 m

Engine block
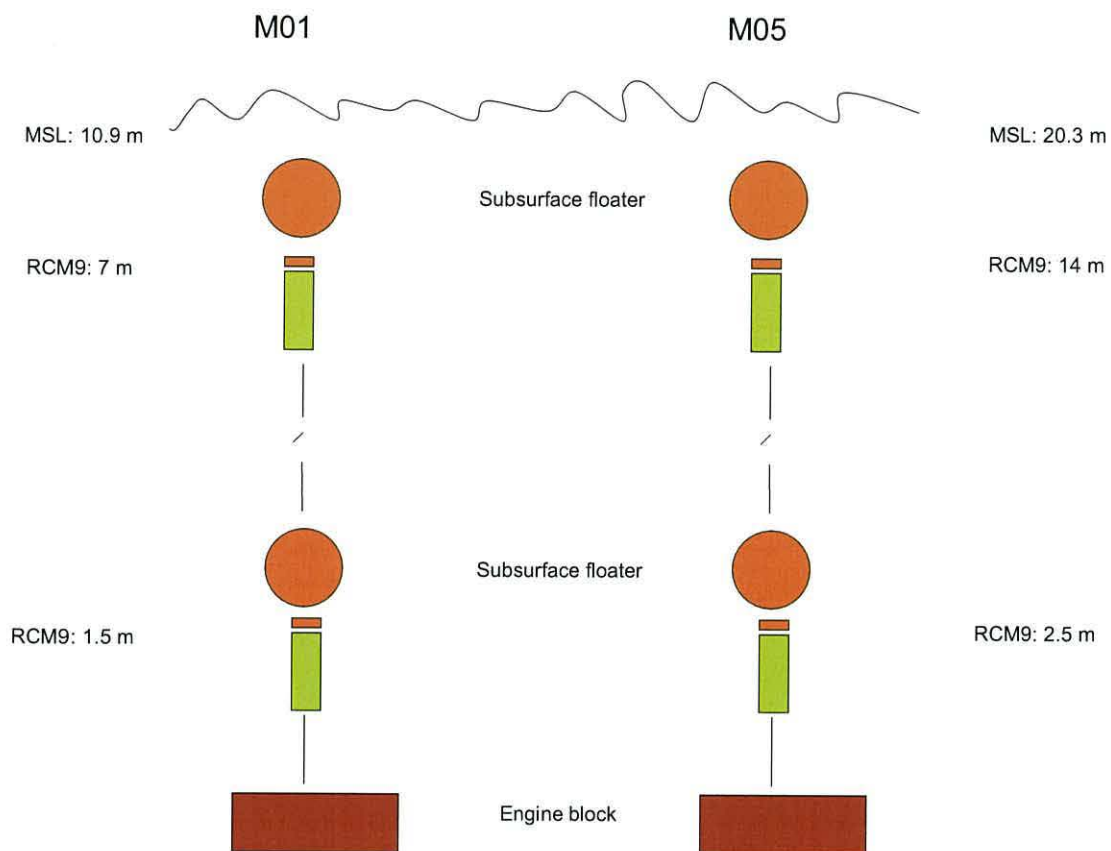
Figure 3:3 – Schematic representation of mooring layout at M01 and M05 with instrument positions in meters above seabed.

Table 3:1 – Planned observational programme

		Mar-03	Apr-03	May-03	Jun-03	Jul-03	Aug-03	Sep-03	Oct-03	Nov-03	Dec-03	Jan-04	Feb-04	Mar-04	Apr-04	May-04
CTD monthly	A B C D															
CTD tidal	CB															
M01 top	Vel C* T P															
M01 bottom	Vel C* T P															
M05 top	VEl C* T P															
M05 bottom	Vel C* T P															
Tide gauges	CN IB															
Incomati flow Maputo flow Airport met Inhaca met																

Planned measurements

C* Conductivity
T Temperature
P Pressure

A-F Monthly Sections
CB Bay-Shelf interface

CN - Clube Naval (Maputo harbour)
IN - Inhaca Island Biology station

Table 3:2 – Implemented observational programme

Legend:
- Analysed data (green)
- Corrupted data (red)
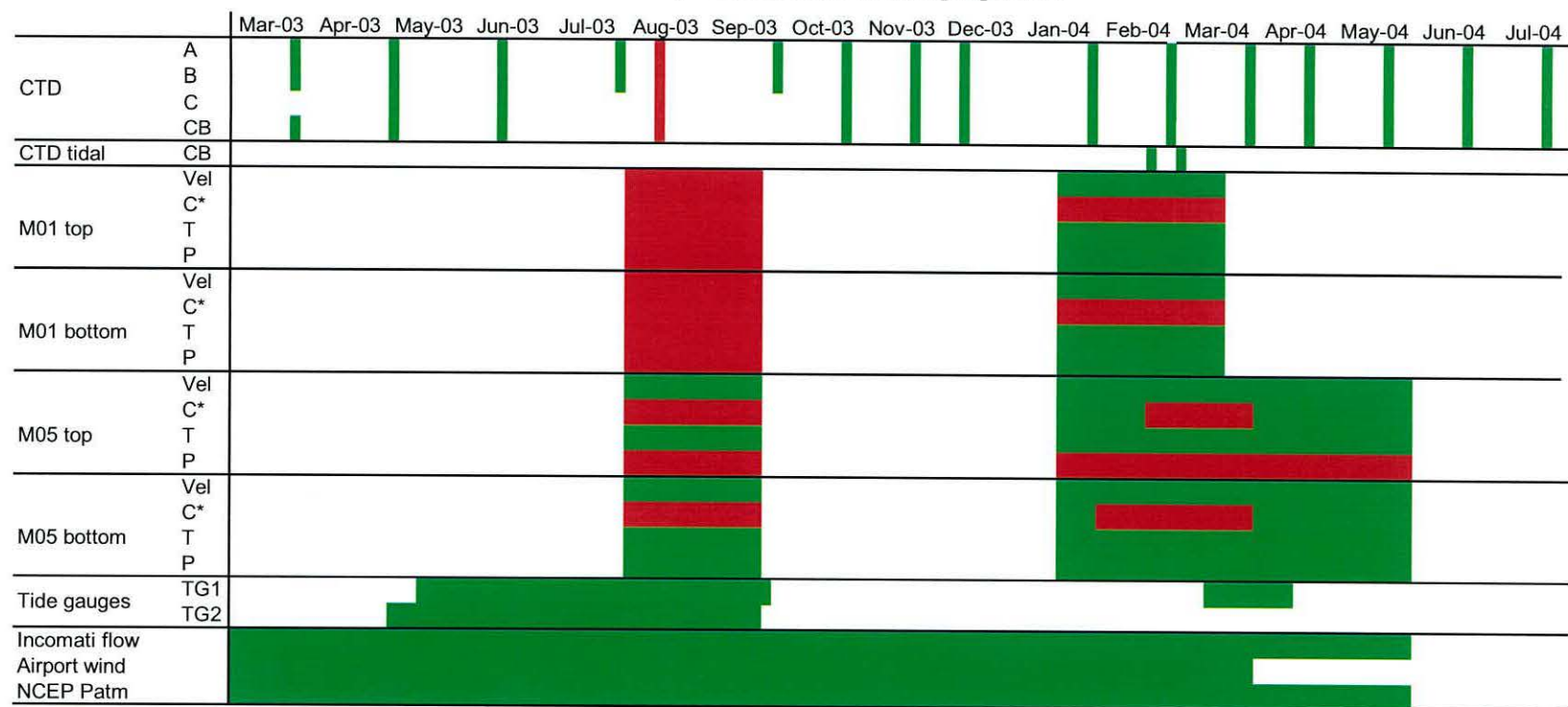
C* Conductivity
T Temperature
P Pressure

A-C Monthly Sections
CB Bay-Shelf interface

TG1- Clube Naval (Maputo harbour)
TG2 - Inhaca Island Biology station

4 Numerical Modelling

4.1 The need for modelling

The observational work undertaken in Maputo Bay in the course of this dissertation project produced considerably less data than expected. To overcome these limitations, modelling was used to provide a fuller picture of the bay's behaviour. In particular, the numerical model extended spatial and temporal coverage of the system's properties, to regions and times where no observations were available.

Numerical 3-dimensional modelling was carried out in four steps:

i) calibration of a realistically forced winter run against observations;

ii) diagnostic of the bay's dynamical properties using an idealised freshwater flow regime with realistic tidal forcing;

iii) realistically forced hindcast run for the full period of observations;

iv) calculation of flushing times using a set of runs forced with idealised values for freshwater and tide.

The setup of the original configuration of the model and subsequent runs were carried out at the Council for Science and Industrial Research (CSIR) in Stellenbosch, Republic of South Africa with the author taking part in the calibration process. The final experimental runs detailed in Chapter 8 were specified, set up and run solely by the author. All modelling data presented in this dissertation were extracted and analysed by the author.

4.2 Technical data and calibration of Delft3D-Flow

The numerical modelling used to explore the physical regime of Maputo Bay was conducted with the Delft3D-Flow hydrodynamic modelling platform. The Delft3D-

Flow is a three-dimensional hydrodynamic and transport simulation program that calculates non-steady flow and transport phenomena resulting from tidal and meteorological forcing (Lesser et al. 2004; WL|Delft Hydraulics, 1999; Nicholson et al. 1997; Bos et al., 1996).

The Delft3D-Flow platform was setup with a 96x135 cells curvilinear irregular grid with a mean resolution of ~500 m, representing the bathymetry of Maputo Bay, with 5 equally spaced sigma layers in the vertical. The modelling domain was dimensioned in order to provide for enough adjustment space between the boundaries and the focus area in Maputo Bay. Tidal forcing was calculated at the boundary using a synthesis of measured tidal harmonics in the bay with the convenient adjustments for phase lag and depth difference. A k-epsilon turbulence closure model was used. In Annex 3, the modelling grid is shown together with the modelling specifications common to all the runs.

In the first step of the numerical modelling effort the model was calibrated comparing a winter season month run against field data. Harmonic analyses were performed on the velocity model output and compared with the observed values to assert the model's representation of tidal forcing and response. In Table 4:1, the differences between observed and modelled harmonics are presented for the first (CR1) and the final (CR2) calibration runs.

Table 4:1 – Observed-modelled tidal harmonics at M05 for the first and the final calibration runs

		Calibration Run 1				Calibration Run 2			
	Name	dMaj (cm.s-1)	dMin (cm.s-1)	dInc (°)	dPhase (h)	dMaj (cm.s-1)	dMin (cm.s-1)	dInc (°)	dPhase (h)
Top	M2	-25.6	-6.2	14	1.4	-3.7	0.0	11	0.5
	S2	-5.6	-2.2	13	1.1	-2.6	-0.3	10	0.2
	MSf	2.6	-0.4	41	-39.5	1.2	1.7	-4	28.4
	MS4	0.6	0.5	4	0.5	0.7	-1.2	2	-0.2
Bottom	M2	-14.0	-1.5	8	1.0	4.3	0.1	6	0.3
	S2	-0.3	0.1	7	0.8	2.8	0.3	5	0.0
	MSf	3.7	-0.3	-12	81.3	0.5	-1.4	-4	32.3
	MS4	-0.4	-2.0	17	0.6	2.4	-0.3	19	-0.1

The first Delft3D-Flow results, CR1, showed discrepancies in the tidal currents

(Figure 4:1). The field measurements exhibit the expected asymmetry between flood and ebb due to energy dissipation and transfer to high harmonics inside the bay as reported in Pingree and Griffiths (1979) and Speer and Aubrey (1985). CR1 does not show this asymmetry which suggests that frictional effects are not properly represented.

Further indication that frictional dissipation is underestimated in the uncalibrated model comes from calculating the energy budget for the M_2 and S_2 tidal waves using Equation 4:1 (Table 4:2).

Equation 4:1
$$W_t = \frac{1}{2}\rho g \hat{U}^2 \sqrt{g\zeta} \cos(\varphi_\zeta - \varphi_u)$$

where, ρ is the density of the propagation medium, ζ is the amplitude of the elevation, $\hat{U}$ the depth averaged tidal velocity amplitude and $\varphi_\zeta - \varphi_u$ the difference in phase between the elevation and velocity waves (Howarth and Pugh, 1983). The phase difference, velocity and tidal amplitudes were assumed approximately homogenous along the cross-section perpendicular to the direction of propagation of the tidal wave. Multiplying Equation 4:1 by the length of this cross-section yields the amount of work done by the tides landward of the transect. Using the data acquired at M05, the amount of work performed by the tides in Maputo Bay was 364 MW for M_2 and 177 MW for S_2.

Table 4:2 – Tidal energy dissipated inside the bay

	Observed (MW)	CR1 (MW)	CR2 (MW)
M2	364	219	331
S2	177	63	129

The discrepancies in dissipated tidal energy were corrected altering the bottom roughness parameter from an initial Nikuradse (1932) length of $k_s=3\times10^{-2}$ to 10^{-1} m. The roughness parameter $k_s=30\times Z_0$ and is translated into the Chezy friction coefficient, C, within the model by the following expression:

Equation 4:2
$$C = 18\log_{10}\left(\frac{12H}{k_s}\right),$$

where H is water depth (WL|Delft Hydraulics, 1999). With this correction, the shape of the tidal height and tidal current records were improved (Figure 4:1) and so was the harmonic comparison. Marginal improvement was achieved by allowing the cells at the comparison stations to have the same depth of the field stations.
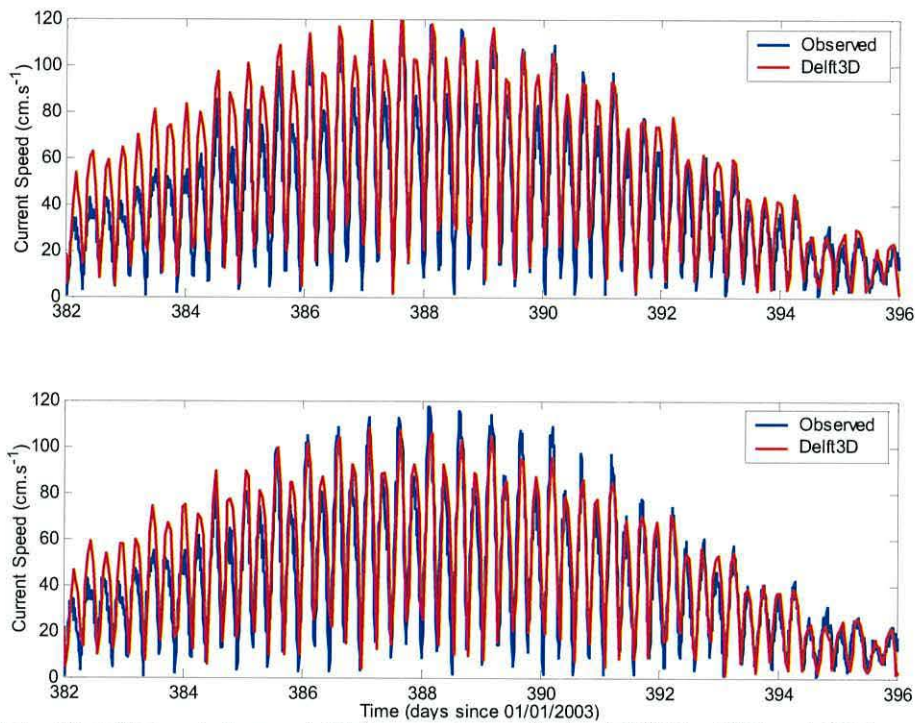
Figure 4:1 – Modelled and observed tidal current magnitude at M05 for CR1 and CR2.

4.3   Model runs

With the model calibrated to tidal forcing, the second step in the modelling effort was to diagnose the Delft3D-Flow representation of the main dynamic features of the bay. Several runs were designed to test the model's robustness in relation to tides, freshwater input and wind variations. With these tests, the ability of the model to reproduce water column structure, residual currents and Ekman transport was confirmed against similar modelling exercises and systems. Only two of the eleven diagnostic runs undertaken are use in this dissertation: i) the D11 – *dry steady* – is a dry summer run where no freshwater enters the bay and no wind action is considered for 30 days; ii) D12 – *wet steady* – is a wet summer run were freshwater enters the

bay at a constant rate of 1000 m^3.s^{-1} (on a 3:2 Incomati to Maputo flow relation) for the first 15 days followed by 15 days with no flow. Similarly to D11, no wind action is considered for the full run. The run specifications for the full experiment are detailed in Annex 3.

To evaluate the Delft3D-Flow performance, residual velocities were compared with the observations during the dry season in D11. In D12, the representation of the density driven circulation was evaluated on the model's ability to reproduce density gradients, frontal structures and coastal currents expected under high runoff conditions, with comparisons made against published work for other large estuaries and ROFI systems.

Additionally, D12 is used to explore the bay's dynamical response by extracting the horizontal residual circulation in the presence of a density gradient at neap and spring tides.

In the third step of the numerical modelling effort, a reference run was set up in order to attempt to reproduce the system dynamics during the sampling period. In addition to the tides, the model was forced with hydrological and meteorological parameters for the period of interest. These series came from observational sources when available and were supplemented with model outputs when to supplement gaps in the observations (*e.g.* Maputo River flow). This run came to be known as the *basecase* run.

The last set of runs designed to calculate the flushing time in Maputo Bay are detailed in Chapter 8 together with the analysis of their results.

4.4   Limitations of the model

It is important to state that accuracy of a hydrodynamic model is greatly dependent of the quality of the bathymetry. The available bathymetry of Maputo Bay results from a

compilation of surveys dating from the nineteen sixties to the nineteen eighties so that there may be significant departure from the present day bathymetry.

At its final version, the Delft3D-Flow model of Maputo bay was considered calibrated to the first degree by representing satisfactory tidal motion and dissipation.

Throughout this dissertation, the numerical model's ability to simulate the bay will be assessed in its ability to reproduce dynamics identified in the observations such as residual circulation and evolution of the water column density structure.

5 Sea surface elevation and velocity

In spite of the numerous complications acquiring the long-term moored data, a valuable dataset of sea surface elevation and velocity was sampled continuously. This chapter analyses tidal and subtidal frequencies of sea surface elevation and velocity in search of answers to the following questions:

- Does the present data confirm the previous studies on the nature of the tidal regime in Maputo Bay?

- What role do the tides and atmospheric processes play in setting up surface slopes and driving residual currents?

- How large is the amount of tidal energy dissipated in Maputo bay and how does it vary with the neap to springs cycle?

- Now that the Delft3D-Flow simulation is tidally calibrated, how accurately can it represent the subtidal dynamics in the bay in both dry and wet conditions?

To provide answers for the questions above, this chapter uses the observed sea surface elevation and velocity, supplemented by 3d modelling and theory to yield a picture of the bay's response to tidal, event-scale and subtidal forcing.

As it was detailed in Chapter 3, the several long-term measurements taken do not always overlap in time. Elevation at TG1 and TG2 was obtained almost simultaneously for ~4.5 months during the dry season. As for the currents, only M05 yielded data at both dry and wet season conditions. At M01, the data refer approximately to the first 2 months of the wet season.

5.1 Tidal characteristics of Maputo Bay

The tides in Maputo Bay were analysed in previous works by Saide (1995), Hoguane

et. al. (1999) and Canhanga and Dias (2005). As part of the sampling effort detailed in Chapter 3, tidal elevation was measured at Clube Naval (TG1) and Inhaca Island biology station (TG2) for 129 and 139 days respectively. These deployments were carried out during the dry season. Additionally, there was a late deployment at TG1 between 11/03/2004 and 12/04/2004 that took place during the wet season. A section of these deployments is presented in Figure 5:1, where it is immediately apparent the large spring to neaps change in tidal range. For the full record, the minimum tidal range was 0.56 m and the maximum 3.11 m.
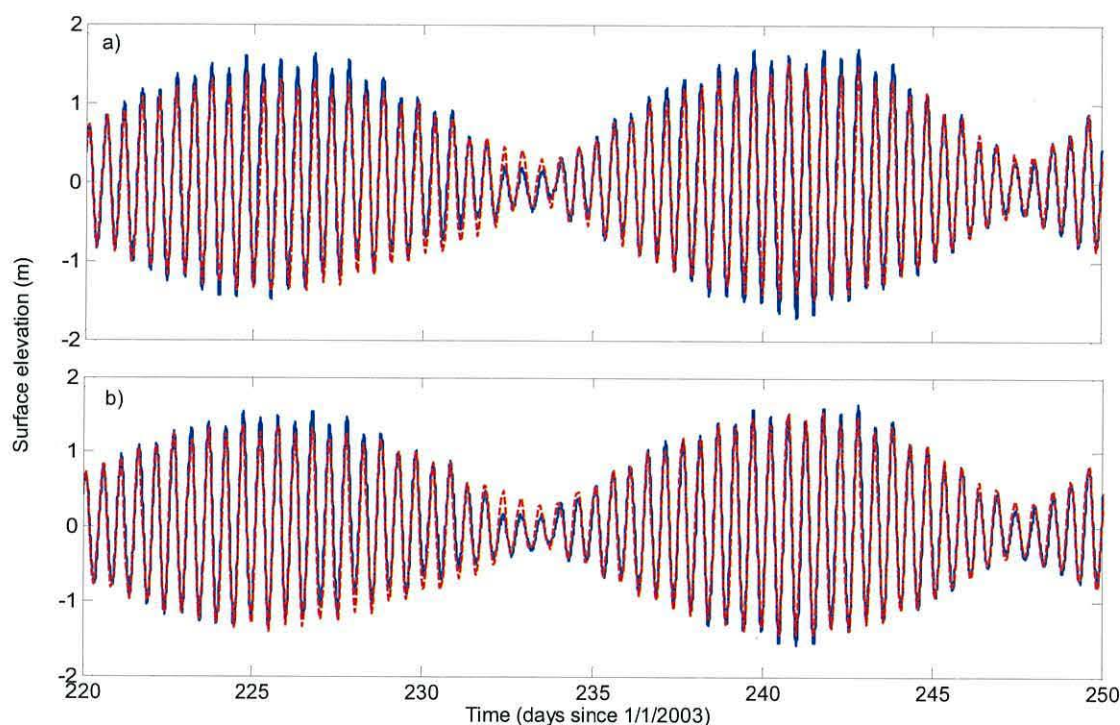
Figure 5:1 – Surface elevation, observed in blue and Delft3D-Flow results in red at a) TG1, b) TG2.
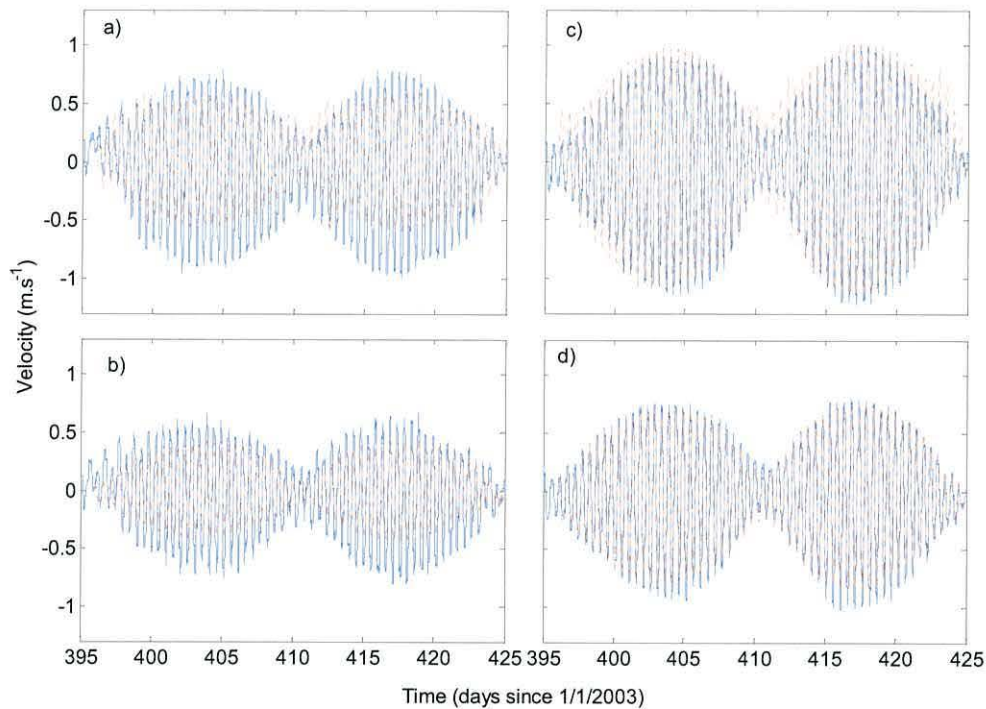
Figure 5:2 – Velocity along the major axis of the tidal ellipse, observed in blue and Delft3D-Flow results in red at a) M01 top, b) M01 bottom, c) M05 top and d) M05 bottom.

Current meters were deployed for considerably longer periods than has been reported in any of the previously published work. The moorings at M01 and M05, each with two current meters, were deployed for a maximum 182 days of continuous deployment. Again, the spring to neaps difference in tidal velocity amplitude is pronounced as shown in the section shown in Figure 5:2. The maximum current amplitude was of 1.3 m.s^{-1} during a spring tidal range of 2.98 m. The minimum current amplitude was as small as 0.09 m.s^{-1}, during neap tides when tidal range amounted to only 0.8 m.

Both observations and the Delft3D-Flow model show a marked asymmetry in the tidal currents with a stronger flood than ebb increasing with tidal range. Nevertheless, the classical shape of the semi-diurnal cycle with short and strong flooding followed by long and weak ebbing (Pingree and Griffiths, 1979) was absent, implying a net transport inshore at both moorings, which increased with tidal range.

In Figure 5:3 (page 36), the tidal ellipses at M01 and M05 are plotted in the form of a single period excursion for M_2, S_2, MS_f, and MS_4 tidal constituents.

5.1.1 Tidal harmonic analysis

The harmonic analysis of velocity and surface elevation was performed using the t-tide software package (Pawlowicz $et.$ $al.$, 2002).

Table 5:1 and Table 5:2 (pages 37 and 38) show the analysis of the pressure and velocity recordings at TG1 and TG2. The common characteristics at both stations are the strongly semidiurnal character of the tide and the relatively small value of M_2 in relation to the rest of the semidiurnal constituents, resulting in the observed high spring to neaps ratio. With regard to sea surface elevation, the tide lags in Clube Naval (TG1) relatively to Inhaca Island (TG2) by 8 and 12 minutes, for M_2 and S_2 respectively. This small lag was also reported in Hoguane $et.$ $al.$ (1999) and in Canhanga and Dias (2005).

Significantly larger time lag is observed in tidal velocity with M05 lagging in relation to M01 by 1 hour and 24 minutes for M_2 and S_2, respectively. This is clearly a data handling error since the tide is rising first inside the bay than at the mouth. An unrecoverable error was identified in M01's timestamp. However, this error is of no relevance to the arguments put forward as the tidal signal at M01 is never compared with other measurements and in the case of subtidal comparisons the lag can be ignored.
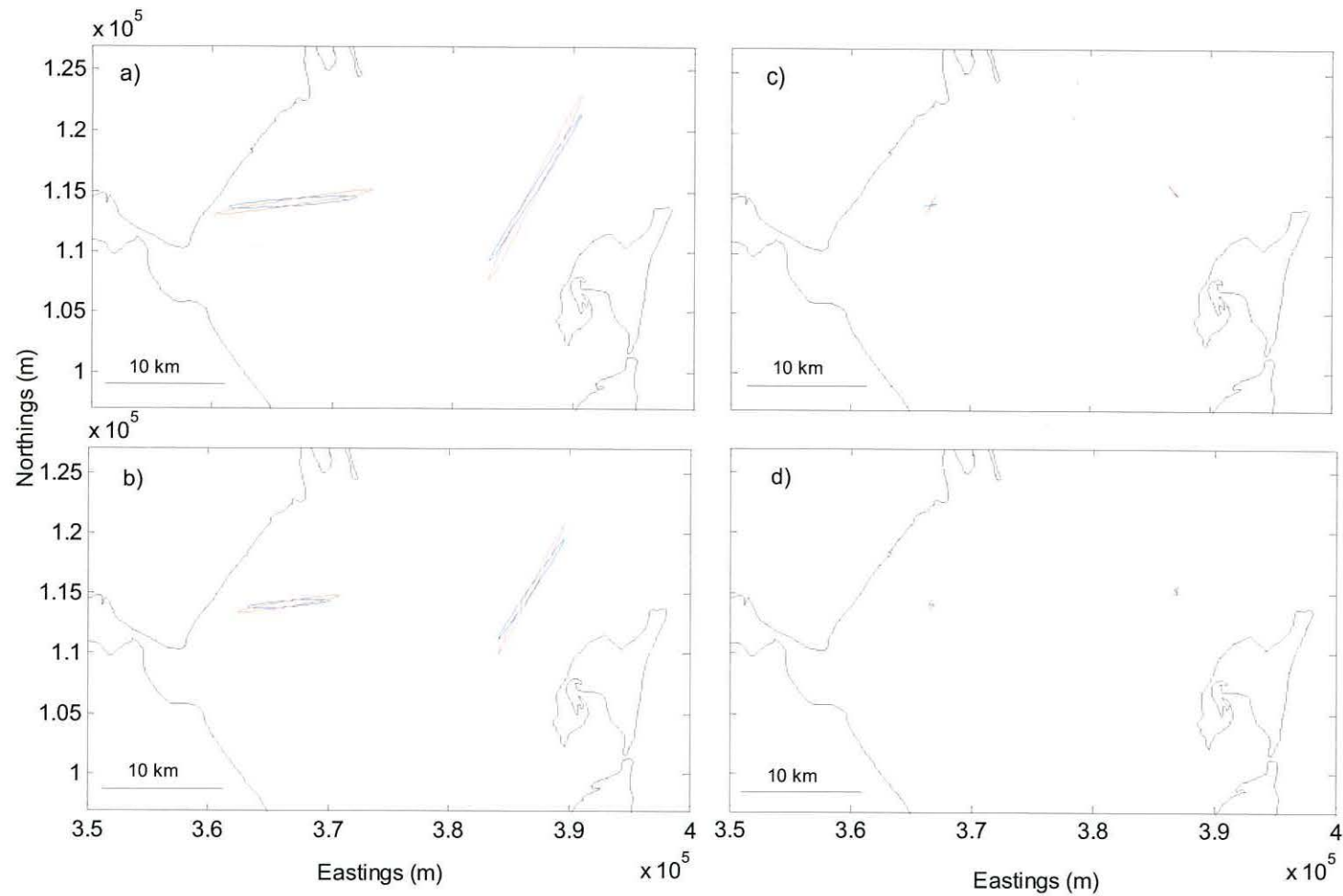
Figure 5:3 – Harmonic components of the tidal excursion (blue bottom and red top): a) M$_2$, b) S$_2$, c) MS$_f$ and d) MS$_4$.

Table 5:1 – Tidal harmonic constituents for sea surface elevation: Amp – constituent amplitude; φ – phase lag.

	TG1				TG2			
	Observations		Delf3D-Flow		Observations		Delf3D-Flow	
	Amp. (m)	φ (°)	Amp. (m)	φ (°)	Amp. (m)	φ (°)	Amp. (m)	φ (°)
MSF	-	-	-	-	-	-	-	-
Q1	0.01	309	0.01	221	0.01	310	0.01	214
O1	0.02	357	0.02	314	0.02	352	0.02	309
K1	0.05	172	0.04	240	0.04	182	0.04	236
MU2	-	-	0.10	223	-	-	0.10	210
N2	0.14	102	0.12	93	0.14	101	0.12	81
M2	0.91	121	0.87	153	0.86	117	0.88	142
S2	0.47	168	0.47	206	0.44	162	0.48	195
M3	0.01	238	0.01	292	0.01	228	0.01	276
SK3	0.01	340	-	-	0.01	321	-	-
M4	0.01	158	0.02	228	0.01	192	0.02	240
MS4	0.01	253	0.01	329	0.01	255	0.02	326
S4	-	-	0.01	320	-	-	0.01	337
2MN6	0.01	37	-	-	0.00	6	-	-
M6	0.01	59	0.01	149	0.01	33	0.01	125
2MS6	0.02	96	0.02	179	0.01	66	0.01	163
2SM6	0.01	146	0.01	247	0.01	111	0.01	228
M8	-	-	0.03	118	-	-	0.02	62

Table 5:2 – Tidal harmonic constituents for velocity: U_M – velocity along major axis; U_m – velocity along minor axis; Inc – major inclination from N; φ – phase lag.

	M01 Observations				M01 Delf3D-Flow				M05 Observations				M05 Delf3D-Flow			
	U_M(m/s)	U_m(m/s)	Inc (°)	φ (°)**	U_M(m/s)	U_m(m/s)	Inc (°)	φ (°)	U_M(m/s)	U_m(m/s)	Inc (°)	φ (°)	U_M(m/s)	U_m(m/s)	Inc (°)	φ (°)
MSF	0.07*	-	-	-	0.00	0.00	148	243	0.04	0.00	123	221	0.03	0.00	142	223
O1	-	-	-	-	0.00	0.00	21	62	0.01	0.00	52	100	0.01	0.00	60	68
K1	0.03	0.01	12	329	0.01	0.00	33	358	-	-	-	-	0.02	0.00	64	344
MU2	-	-	-	-	0.04	0.00	29	336	-	-	-	-	0.07	0.00	60	320
N2	-	-	-	-	0.05	0.00	28	204	0.07	0.00	62	221	0.10	0.00	61	195
M2	0.47	0.02	9	210	0.38	0.00	28	266	0.60	0.02	63	239	0.69	0.02	60	258
S2	0.30	0.02	9	273	0.22	0.00	28	316	0.42	0.01	63	285	0.41	0.01	61	307
M4	-	-	-	-	0.00	0.00	175	140	0.03	0.01	81	340	0.03	0.01	101	10
MS4	0.03	0.01	102	335	0.01	0.00	45	147	0.05	0.02	82	41	0.03	-0.01	96	86
2MS6	-	-	-	-	0.01	0.00	16	319	0.02	-0.01	76	302	0.03	0.00	70	332
2SM6	-	-	-	-	0.00	0.00	20	8	0.02	0.00	74	351	0.01	0.00	69	27
M8	-	-	-	-	0.03	0.00	28	227	-	-	-	-	0.03	0.00	65	214

*)small signal/noise ratio

**) timestamp error

The tide gauges show only small elevation amplitude attributed to shallow water constituents such as MS_f, M_4 and M_6. Inversely, both current meters show significant response at these frequencies. The values found for MS_f velocity constituent reach ~ 0.04 – 0.07 m.s^{-1} and coincide with the ones reported in Canhanga and Dias (2005).

There is little to be commented on the simulation of the major tidal constituents by the Delft3D-flow model, since these were the main forcing at the boundary. Inversely, the shallow water constituents were absent from the forcing, implying that their simulated results show how accurate the quadratic relations between tide and bathymetry are modelled. As in the observations, the model shows little response in the elevation shallow water harmonics but a significant one in the velocity results for the same frequencies.

5.1.2 Tidal energy input

The fortnightly modulation of tidal forcing has an effect in the amount of energy dissipated inside the bay, contributing to the tidal mixing of the water column.

Table 4:2 (page 28) shows the net energy flux into the bay calculated according to Howarth and Pugh (1983) using Equation 4:1 for values at M05.

An alternative method was applied using the results from the Deltft3D-Flow run D11, where no freshwater flow was allowed to enter the bay, to assess the spatial variation of tidal mixing. The rate of tidal dissipation was calculated according to:

Equation 5:1
$$\varepsilon = C_D \rho \frac{U^3}{h},$$

where C_D is the bottom drag coefficient (2.5x10^{-3}), ρ average seawater density (1025 km^{-3}), U average tidal current's magnitude over 1 tidal cycle, and h water depth (Simpson and Hunter, 1974). During spring tides ε is ~ 0.1 Wm^{-3} over a large proportion of the Bay while to the northwest of Inhaca Island there is an area of intensive stirring with values exceeding 1.0 Wm^{-3}. The results of the model indicated

2 to 3 orders of magnitude difference between spring and neap tides in the effective

tidal mixing energy input (Figure 5:4), which is consistent with the observed change

in current amplitudes noted above, implying a considerable fortnightly change in the

balance between stratifying and stirring terms. As stated in Section 4.2, the final

calibration of the hydrodynamic model was consistent with the energy flux observed

in the field.
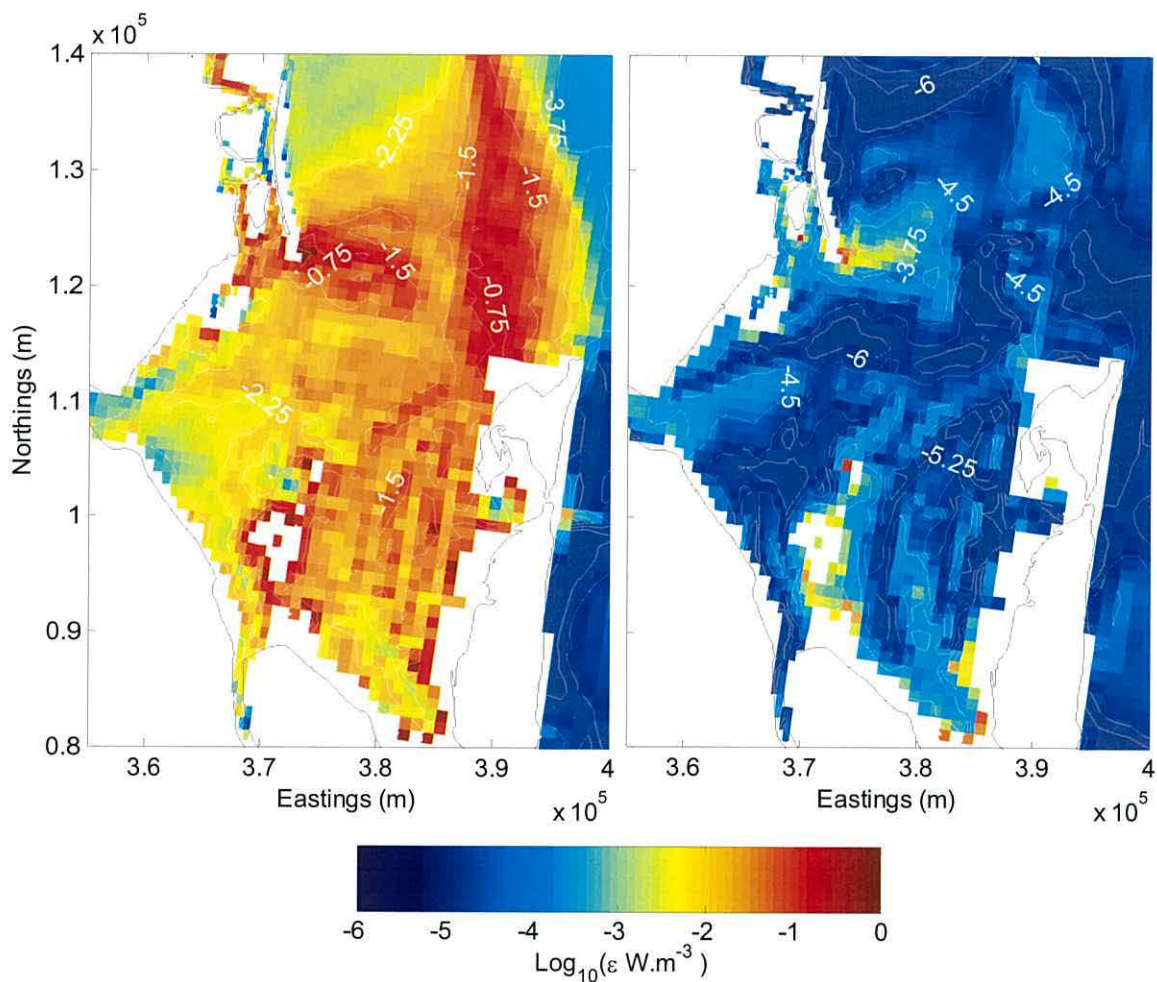
Figure 5:4 - Tidal stirring energy in spring (left) and neap tides (right).

5.2 Subtidal sea surface elevation and velocities

The pressure and velocity signals were filtered in the time domain with a 72 h

window low-pass tidal filter (Pugh, 1984).

5.2.1 Subtidal surface elevation

Atmospheric pressure from NCEP reanalysis was used to compensate for the regional

sea surface response to atmospheric pressure variation know as the inverse barometer effect (Gill, 1982). When atmospheric pressure variation is included, the hydrostatic pressure variation, becomes:

Equation 5:2 $$\rho g \eta = \rho g \eta' - P_{atm},$$

where η is the measured sea surface elevation and η' is the sea level variation adjusted to take into account atmospheric pressure. They relate to each other in the following way:

Equation 5:3
$$\eta = \eta' + \eta_{atm}$$
$$\eta_{atm} = -\frac{P'_{atm}}{g\rho_{sea}},$$

where and η_{atm} is the inverse barometer effect. Sea level adjustment to regional atmospheric pressure change occurs at timescales shorter than 24h. This adjustment phase lag is filtered out when the 72h filter is applied, in this way the inverse barometer effect can be subtracted from the filtered series.
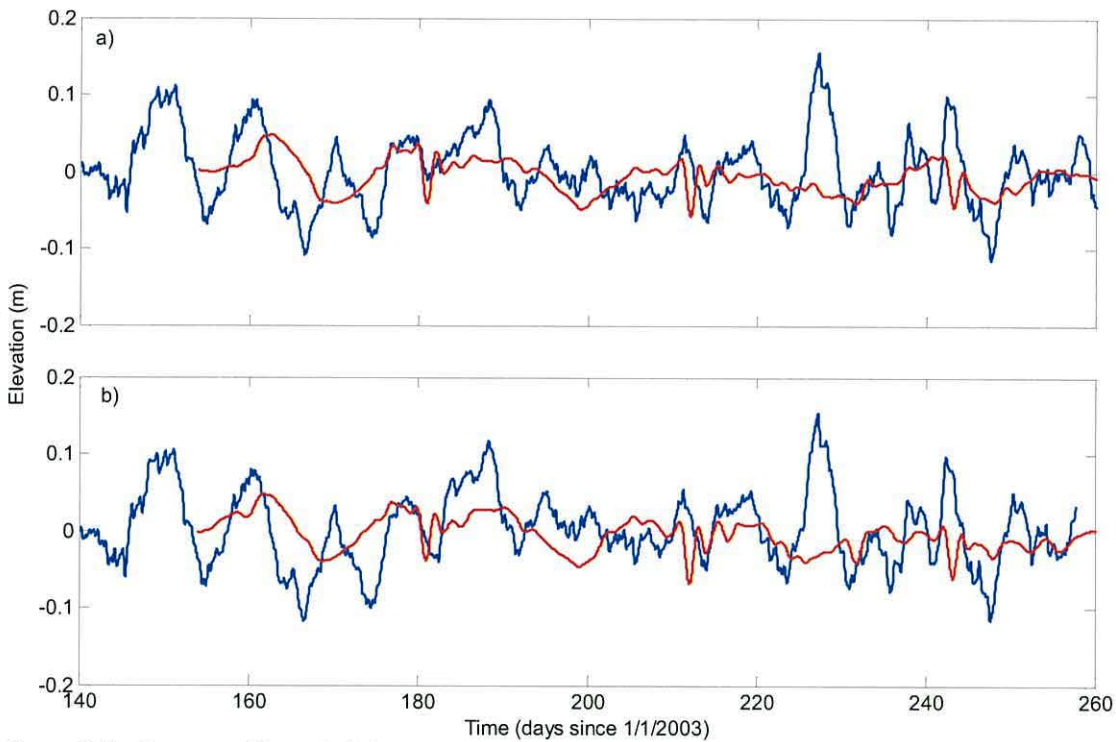
Figure 5:5 – Low pass filtered η' (blue: observations; red: Delft3D-Flow): a) TG1, b)TG2.

In Figure 5:5, the subtidal reduced elevation is plotted together with the respective Delft3D-Flow results. The dynamic range of the signal is ~0.3 m for the full

observational record. Some amount of periodicity is present in the signal with cycles of ~10 day period and ~0.05 – 0.2 m. However, the cycles differ in shape and the period is not consistent.

In Figure 5:6, the subtidal PSD of the two stations are presented. Overall, the tide gauges show a wide band response about the 9 – 10 day period. Neither wind nor atmospheric pressure shows a response at that band.

Furthermore, the subtidal elevation did not show any response at the fortnightly period. This was an expected result given that the bay connects to the shelf though a wide mouth.

In the Delft3D-Flow simulation, η' shows a considerably shorter dynamic range of ~0.1 m and there was no marked periodicity present in the simulations. The discrepancies between modelled and observed subtidal sea surface elevation seem to indicate that the ~10 day oscillation period present in the observations is due to forcing that was absent in the model setup such as remotely imposed gradients by coastal or oceanic features.
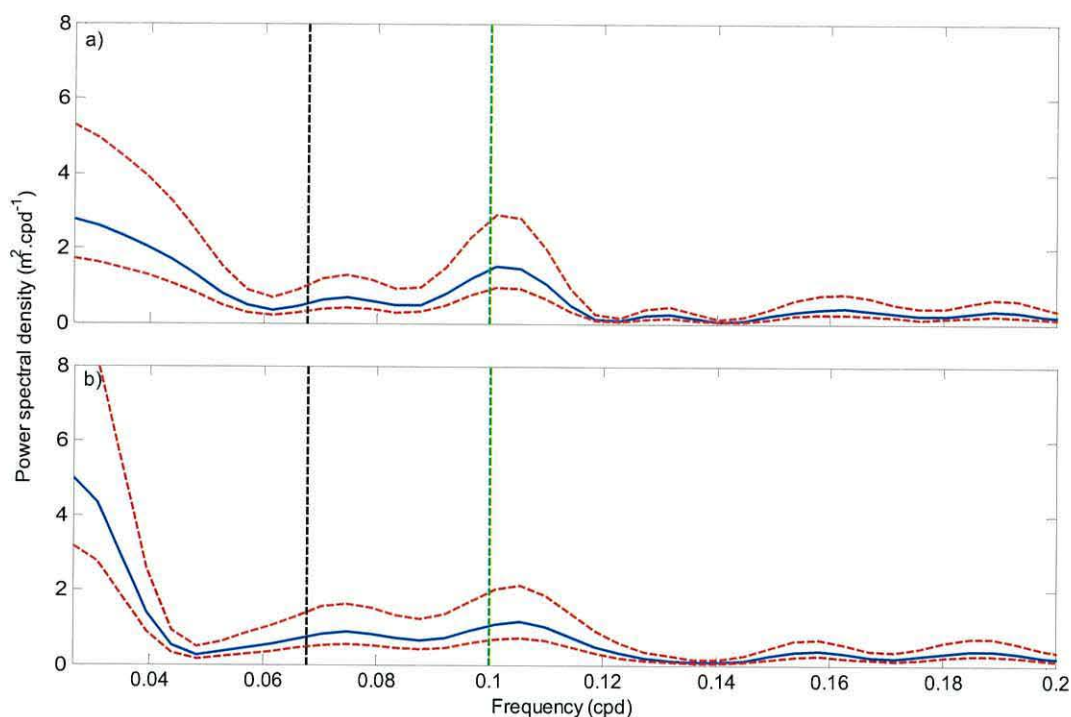
Figure 5:6 – Power spectral density of sea surface elevation in blue, 95% confidence interval in red and vertical black dotted line marking the MS$_f$ frequency at: a) TG1, b) TG2. Spectra from 138 day long series, subsampled in 3 windows with a 50% overlap (DOF = 20).

5.2.2 Sea surface slope

There was no absolute height referencing of the pressure sensors deployed.

Nevertheless, it is possible to analyse the relative time variation of the sensors in

relation to each other.
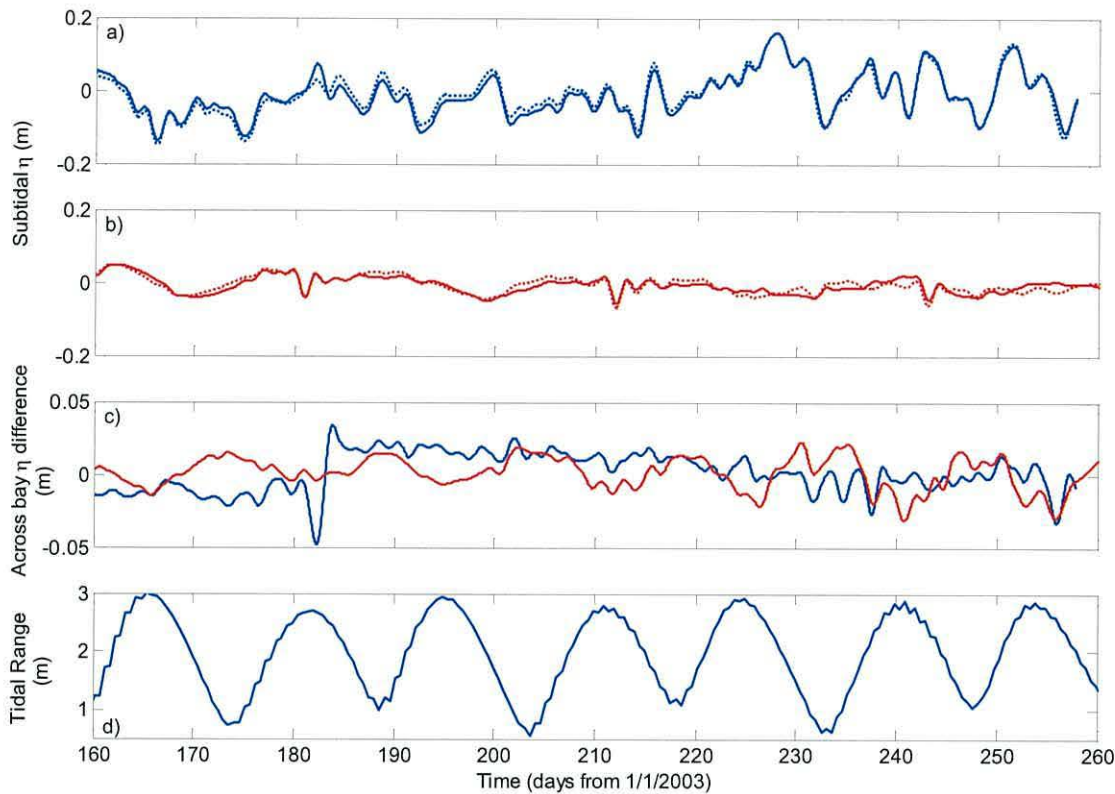
Figure 5:7 – Mean sea surface elevation (MSSE) (blue: observations; red: Delft3D-Flow simulation): a) observed mean surface elevation at TG1 and TG2 (dotted) ; b) Delft3D-Flow *basecase* mean surface elevation at TG1 and TG2 (dotted); c) difference in MSSE = TG2-TG1; d) tidal range.

There was no significant subtidal variation of surface elevation between TG1 and TG2 (Figure 5:7, c). The exception to this is a singularity at day 182 when it is thought that the sensor at TG1 was accidentally offset.

With regard to slope, the Delft3D-Flow simulation, unlike the observations, shows a weak but clear fortnightly oscillation. This relative movement is in phase with tidal range and the inner station TG1 is shown to rise in relation to the outer station at TG2, hitting a weak tidal choking effect (Kjerfve and Magill,1989; Hill, 1994). The artificial production of such a phenomenon can reflect some degree of over dosing of the bottom friction, exaggerating the neap to spring cycle of flood dominance, which in turn will drive a neap to spring rise in the level of the bay. However, this effect is of the order of 10^{-3} m and therefore negligible.

Table 5:3 –Correlation matrix between forcing and residual current magnitude during the wet season.

	M01						M05					
	Top	Bottom	Tidal Range	Freshwater	Wind	Patm	Top	Bottom	Tidal Range	Freshwater	Wind	Patm
Top	1.00						1.00					
Bottom	0.67	1.00					0.77	1.00				
Tidal Range	0.57	0.22	1.00				0.86	0.72	1.00			
Freshwater	-0.28	0.09	-0.15	1.00			-0.01	0.08	-0.16	1.00		
Wind	-0.24	-0.06	-0.12	-0.11	1.00		-0.05	0.04	-0.05	-0.09	1.00	
Patm	0.13	-0.20	0.05	-0.64	0.13	1.00	-0.18	-0.17	-0.13	-0.57	0.03	1.00

Table 5:4 – Correlation matrix between forcing and residual current magnitude during the dry season.

	M05			
	Bottom	Tidal Range	Wind	Patm
Bottom	1.00			
Tidal Range	0.86	1.00		
Wind	-0.02	-0.08	1.00	
Patm	0.05	-0.18	-0.15	1.00
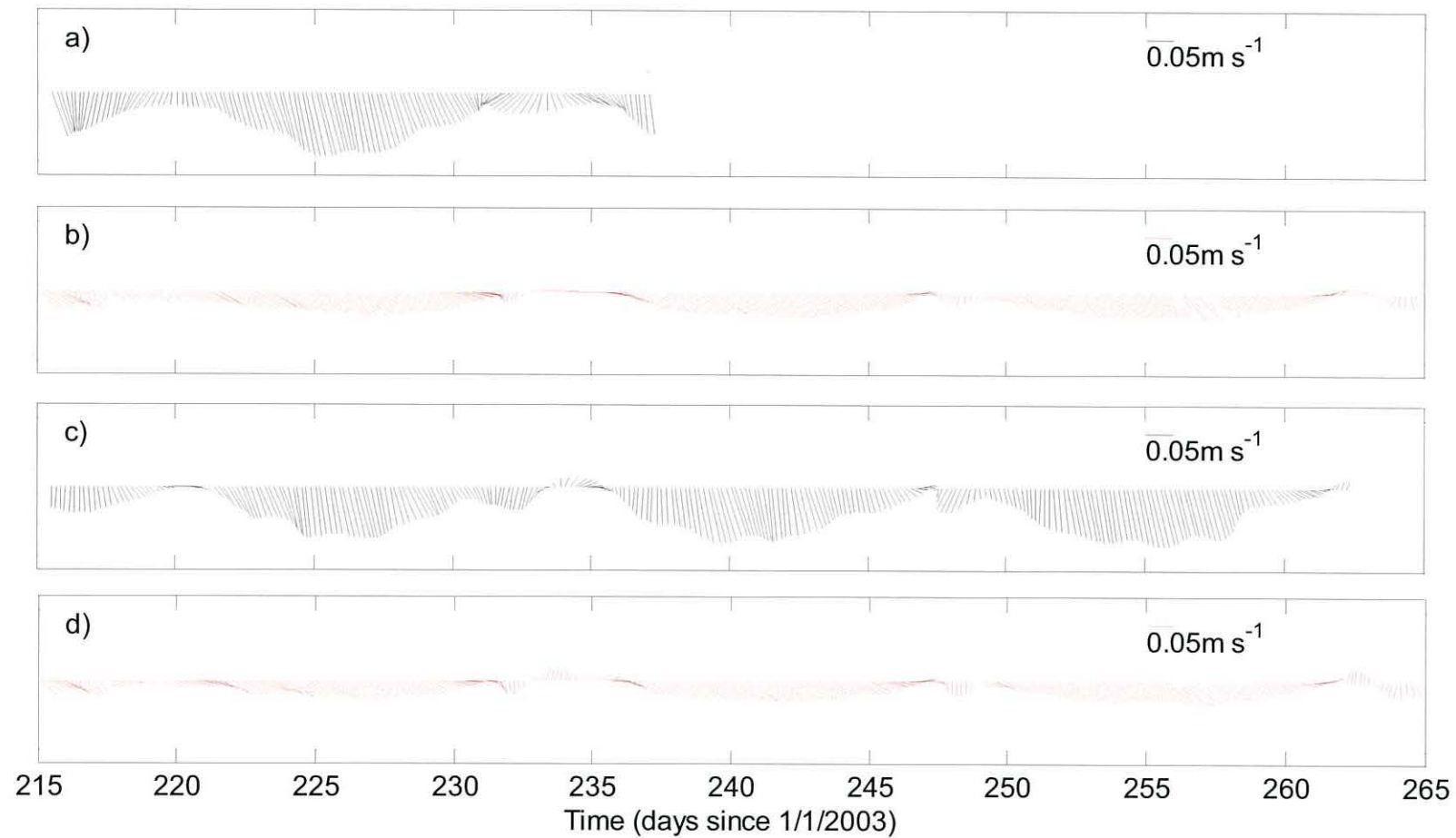
Figure 5:8 – Residual current at M05 during the dry season (black: observations; red: Delft3D-Flow simulation): a) and b) top; c) and d) bottom.
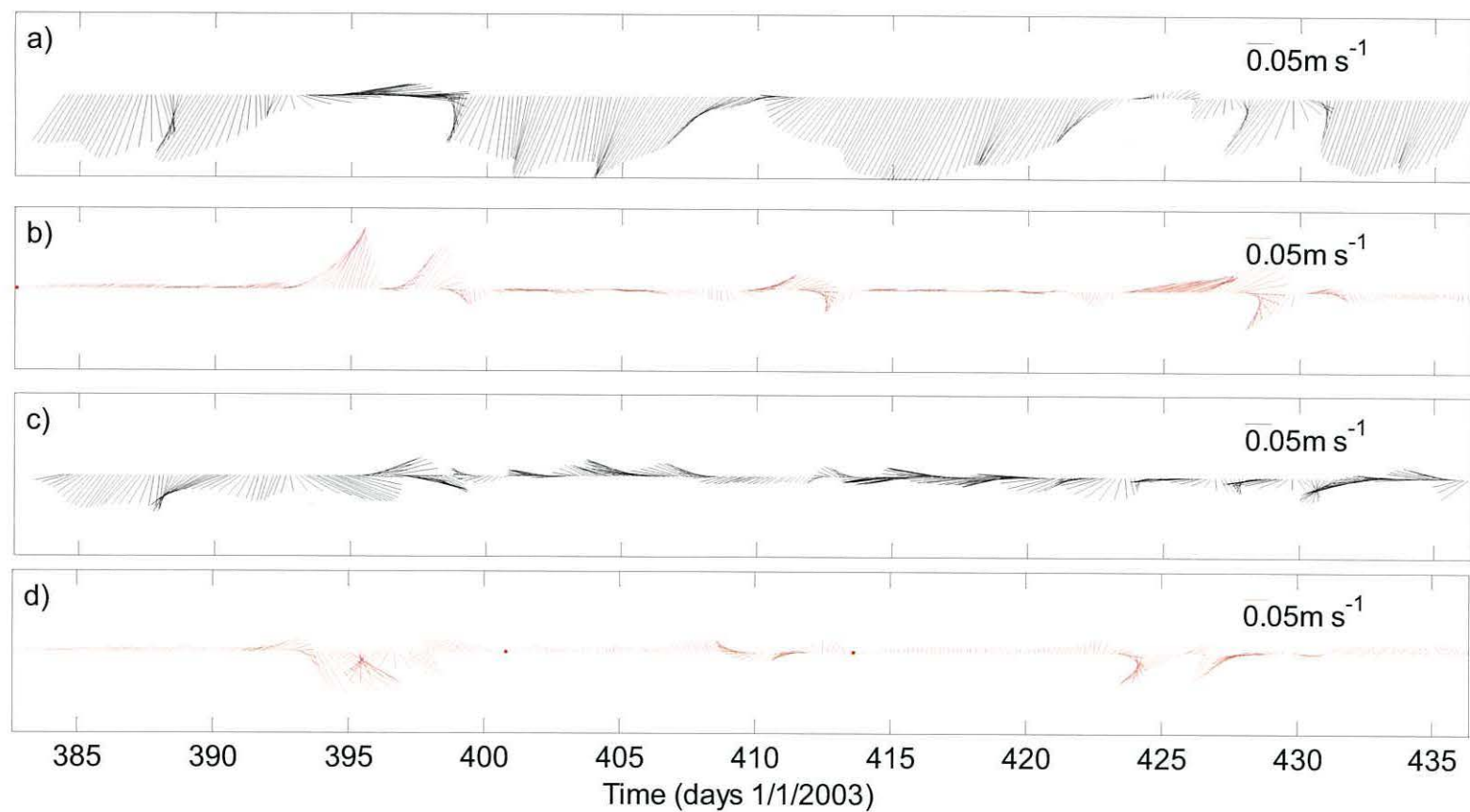
Figure 5:9 – Residual current at M01 during the wet season (black: observations; red: Delft3D-Flow simulation): a) and b) top; c) and d) bottom.
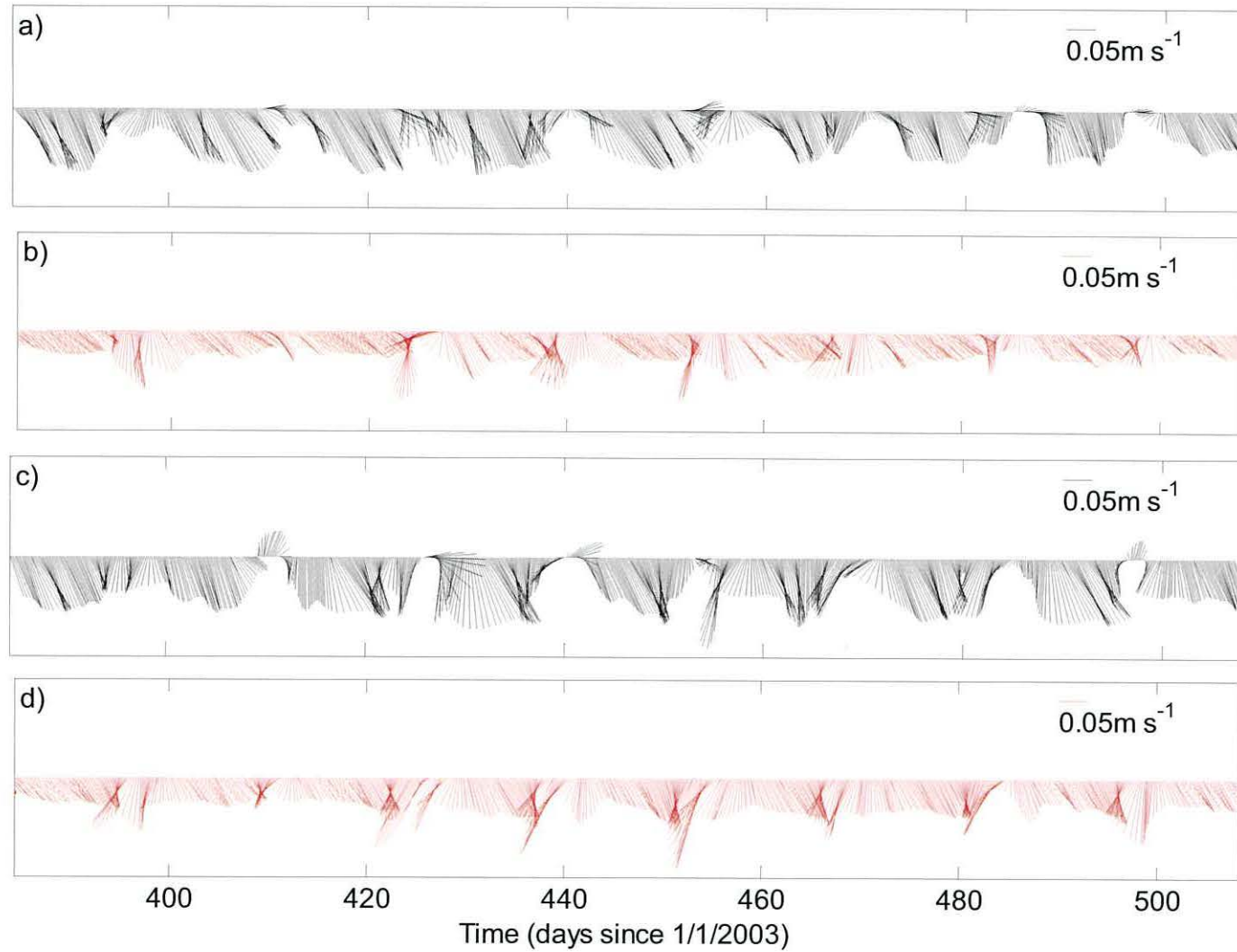
Figure 5:10 – Residual current at M05 during the wet season (black: observations; red: Delft3D-Flow simulation): a) and b) top; c) and d) bottom.

5.2.3 Residual velocity

The residual velocities are plotted from Figure 5:8 to Figure 5:10 (pages 46 - 48). In order to identify the influence of the candidate residual circulation controls, the correlation matrix R_{xy} between the major expected forcing factors and the velocity magnitude is presented in Table 5:3 and Table 5:4 (page 45). The correlation matrix is defined according to Bendat and Piersol (1986) for each pair of time series x and y as,

Equation 5:4
$$R_{xy} = \frac{C_{xy}(0)}{\sqrt{C_{xx}(0)C_{yy}(0)}},$$

where $C(0)$ is the zeroth lag covariance between the series in subscript.

There is a strong correlation between the velocity magnitude and tidal range at both moorings. This is most obvious during the dry winter season at M05 (Table 5:4) when the interference of density driven currents is absent from the residual, with velocity magnitude and tidal range reaching a $R \approx 0.86$ for 1119 DOF. In relation to the horizontal differences, M05 is more dependent on tidal range, whilst M01 also exhibits a response to the influence of freshwater runoff and wind.

Figure 5:11 a) and b) shows the regression model between tidal range and M05 current magnitude during the winter season plotted alongside the recorded data. The red line in the figure depicts the behaviour predicted by a model obtained by least square fitting the measured subtidal current amplitude against tidal range. For most of the record, the subtidal current magnitude increases with the tidal range. Exceptions to this occur for short bursts during the neap tides when the current, predominantly inshore and towards the eastern bank, reverses and flows offshore (e.g. data points indicated by the arrows in Figure 5:11). This behaviour is repeated during the wet season with increased magnitude in the neap tide bursts.
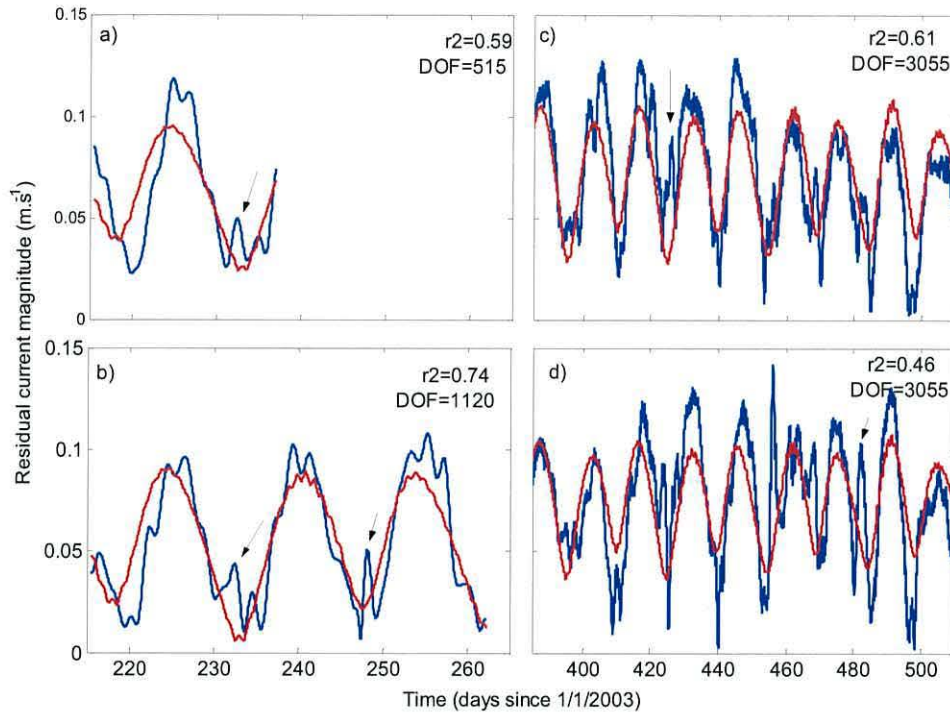
Figure 5:11 – Observed residual current magnitude at M05 (blue) and linear regression model results (red:): a) dry season top; b) dry season bottom; c) wet season top; d) wet season bottom.

The M01 mooring was deployed at the Maputo harbour navigational channel, so that residual currents there are expected to follow the channel. Figure 5:12 plots the along-channel velocity at M01 together with tidal range and freshwater flow. Apart from the background response to tidal range that accounts for up to 57% of the variance (Table 5:3), the rest of the variance is mainly contained on two different events around days 395 and 425. These seem to be generated by the freshwater flow events at day 390 and 422, resulting in a residual current response at the next neap tide. To determine the vertical character of these residual currents, in Figure 5:12 c) the relation between top and bottom velocity is plotted according to:

Equation 5:5
$$B = \frac{\left| \overline{V}_{top} - \overline{V}_{bottom} \right|}{\left| \hat{\overline{V}} \right|},$$

where V is the along channel velocity, the overbar indicates subtidal and the hat depth averaged. This relation gives an estimation vertical velocity profile departure from a strictly barotropic one. It is then possible to say that the episodic increase in along channel velocity is barotropic around day 395, whilst a clear baroclinic signal is found

around day 425.
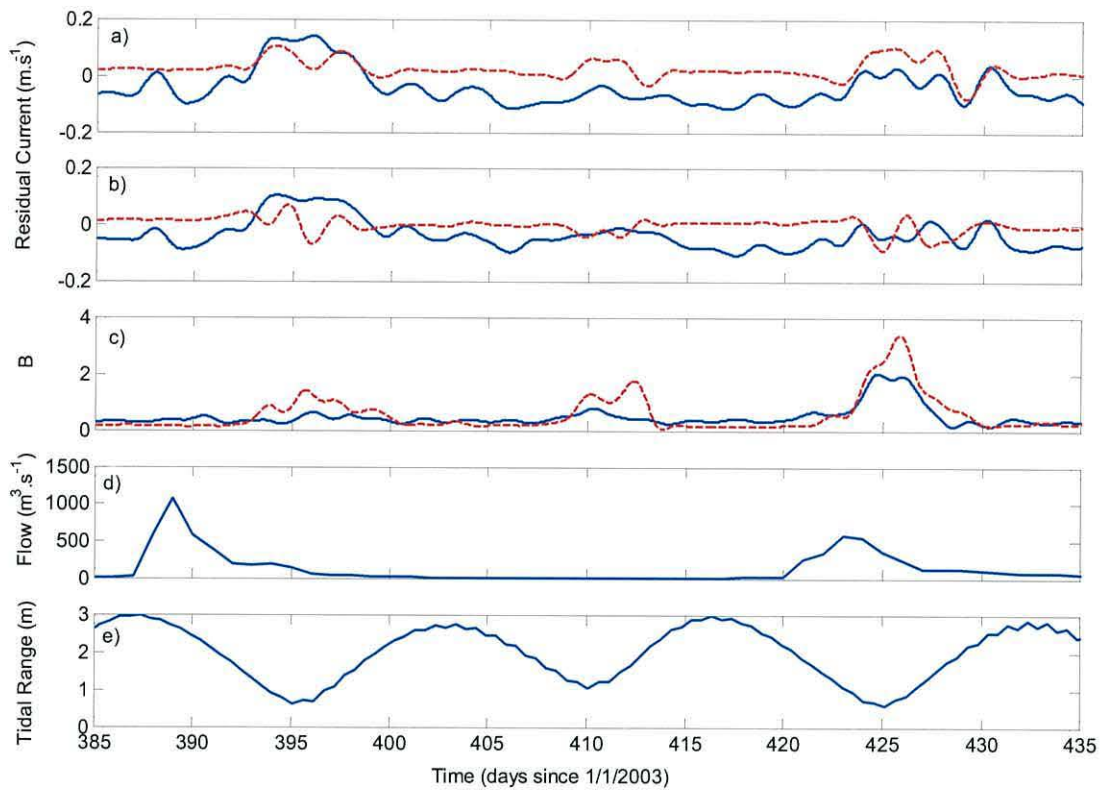
Figure 5:12 – Along-channel residual current at M01 during the wet season (blue: observations; red: Delft3D-Flow simulation): a) M01 along-channel residual current top; b) M01 along-channel residual current bottom; c) result of Equation 5:5; d) Incomati freshwater flow; e) tidal range.

5.2.4 Delft3D-Flow representation of residual currents

Overall, during the dry season, the Delft3D-Flow model simulates satisfactory residual flow, showing the relation between residual current and tidal range as observed (Figure 5:13, a and b) and going to the detail of representing the neap tide burst at M05 (Figure 5:8). However, during the wet season, the fortnightly signal is overwhelmed by the magnitude of the neap tide bursts (Figure 5:13, c and d) so that background tidal rectification is greatly underestimated.
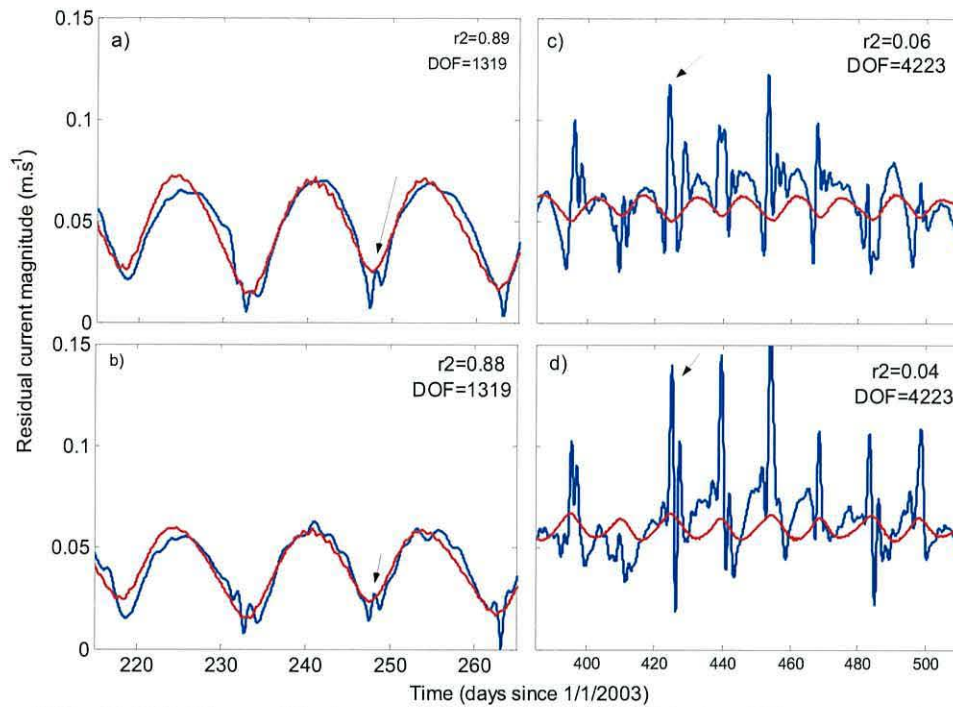
Figure 5:13 – Delf3D-Flow residual current magnitude at M05 (blue) and linear regression model results (red:): a) dry season top; b) dry season bottom; c) wet season top; d) wet season bottom.

For freshwater input events at M01 (Figure 5:12), the Delft3D-Flow simulation showed opposite top to bottom flow direction in both freshwater input episodes and predicted some degree of baroclinicity during the neap tide around day 410. This behaviour contradicts the observation results.

The Delft3D-Flow simulations were used to analyse the spatial distribution of residual current. Figure 5:15 (page 54), shows the cross-mouth velocity derived from the full velocity model outputs for each of the CB section field sampling stations under neap and spring tide conditions. Independent of the tidal and freshwater regime, the water enters the bay through the deep southeast channel and exits through the shallows at the northwest, creating two separated flow cells.

During the dry season, these two cells occupy the full depth of the bay and their location does not change from neap to spring tides. Instead, the response to rise in tidal forcing at spring tides is reflected in the intensification in exchange across the mouth, with residual currents increasing strongly at the shallow end and weakly in the deep channel.

During the wet season, there are clear differences, between neap and spring tides, in the distribution of flow across the mouth of the bay. At springs, the pattern is similar to dry season conditions. In neaps, however, there is estuarine type circulation with the outward cell expanding to the top and centre of the mouth and the inward cell increasing in intensity and occupying the bottom of the deep channel. Unlike dry season conditions, exchange increases when tidal range decreases.
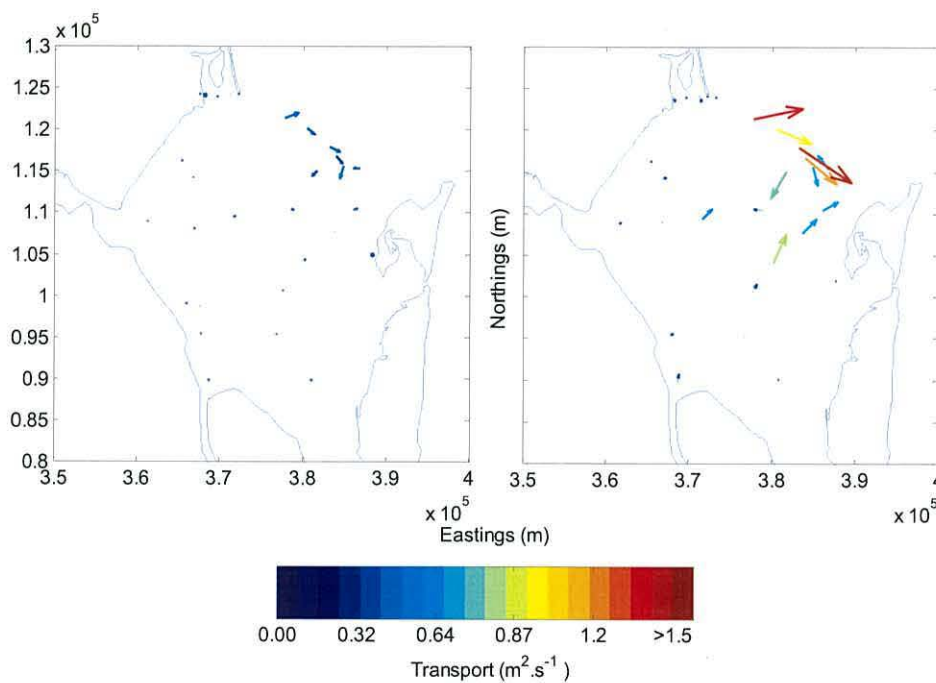
Figure 5:14 – Residual transport in Maputo Bay, Delft3-Flow results during the dry season: a) neap tide day 203; b) spring tide day 194.

Regarding the horizontal distribution, Figure 5:14 shows the depth averaged transport per meter normal to the flow under dry winter conditions. The model shows that circulation is more vigorous at the mouth of the bay, with a cyclonic character.

Figure 5:16 and Figure 5:17 show the residual flow at neap and spring tides under wet conditions. During neap tides (Figure 5:16), a strong estuarine type circulation
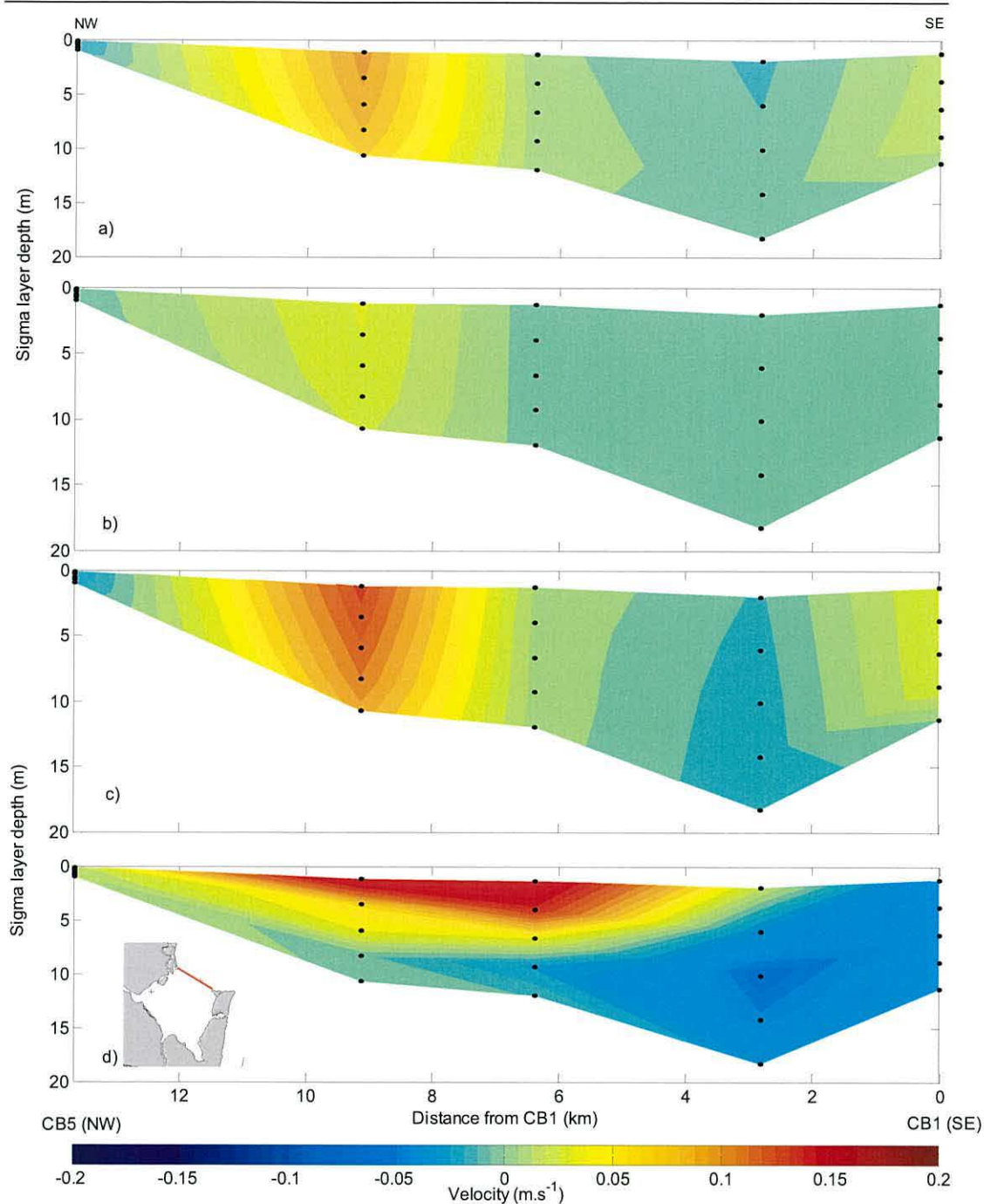
Figure 5:15 – **Cross-sectional residual velocity at the mouth of Maputo Bay (positive offshore), Delft3-Flow results: a) dry season spring tide day at 194; b) dry season neap tide at day 203; c) wet season spring tide at day 417; d) wet season neap tide at day 427.**
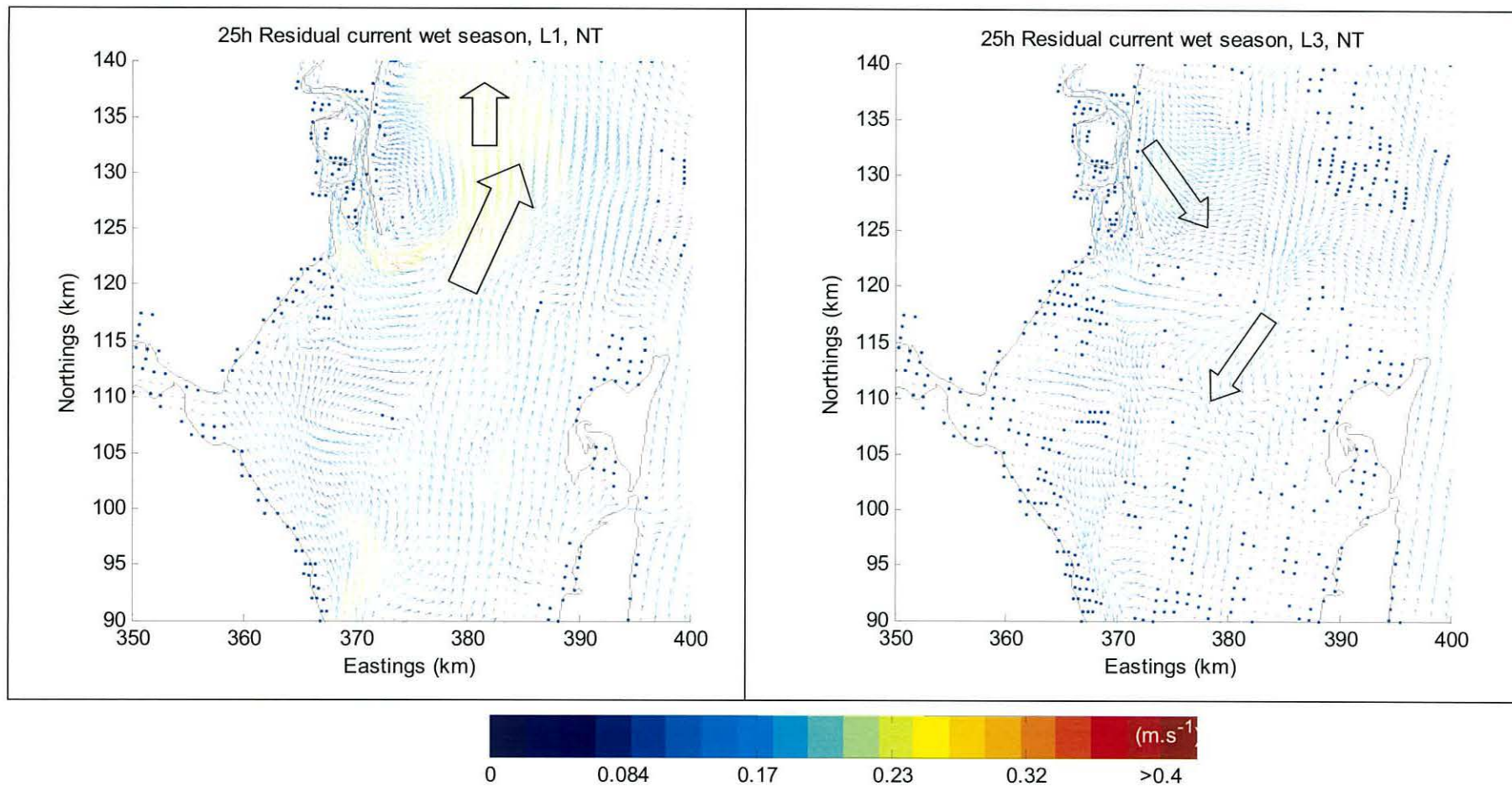
Figure 5:16 – Delft 3D results of residual velocity during neap tide under a wet season regime (L1 – top layer; L3 – 0.5 depth).
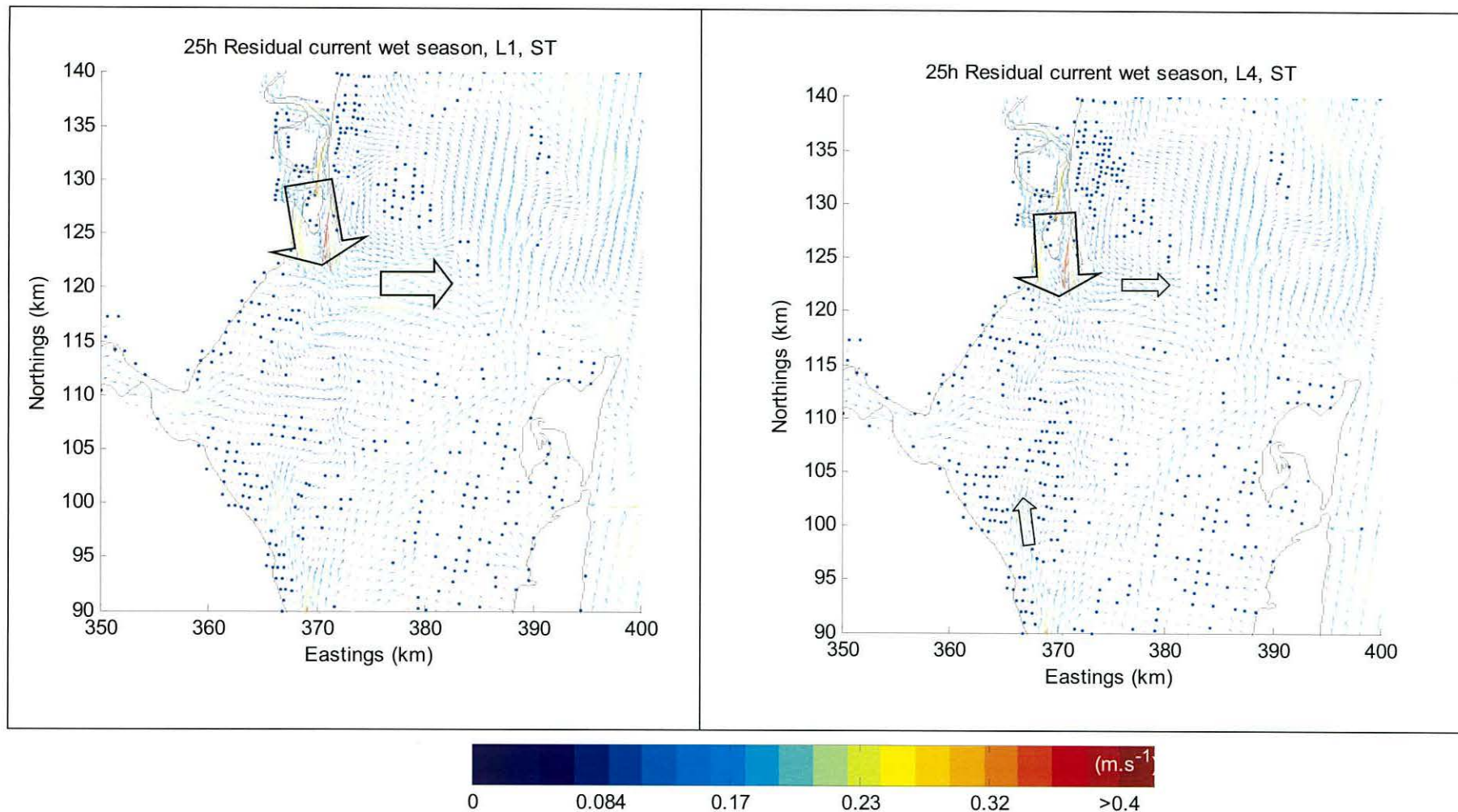
Figure 5:17 – Delft 3D results of residual velocity during spring tide under a wet season regime (L1 – top layer; L4 – 0.7 depth).

develops in response to the horizontal density gradients due to the absence of tidal vertical mixing. This circulation promotes the transfer of estuarine water out of the bay and shelf water into the bay simultaneously which was reflected in an increase in transport across the mouth of the bay as shown in Figure 5:15. During this period the plume expanded turning left, forming a density coastal current. During spring tides (Figure 5:17), the water column is vertically mixed, the gravitational current is arrested and most of the freshwater is retained in the bay as the plume retracts and the coastal current stops.

5.3   Summary of main results

The most remarkable aspects of the sea surface elevation and currents of Maputo Bay is the large neaps springs variation in tidal forcing as noted in previous observational studies for surface elevation (Hoguane *et. al.*1999) and velocity (Saide, 1995). The tide here is strongly semidiurnal and the relatively small value of the M_2 tidal constituent in relation to the rest of the semidiurnal constituents results in the observed high spring to neaps ratio of $\sim 0.5 - 3$ m in height range and $\sim 0.1 - 1.3$ m.s^{-1} in velocity amplitude. The energy dissipated through bottom roughness follows this rise in velocity from $\sim 10^{-4}$ Wm^{-3} in neap tides to $\sim 10^{-1}$ Wm^{-3} during springs.

The short tidal lag between the mouth and the inner bay shows that the tide is close to a standing wave. There is, however, a small progressive character in the tidal wave shown by the energy flux calculated for Maputo Bay. The departure from a strictly standing wave sets the energy dissipate landward of the mouth at 364 MW for M_2 and 177 MW for S_2. The neap to springs cycle of tidal velocity leads to a $\sim 2 - 3$ orders of magnitude difference in energy dissipated ($\sim 10^{-4} - 10^{-1}$ Wm^{-3}). This dissipation through bottom friction should lead to the occurrence of overtides and fortnightly tidal components (Speer and Aubrey, 1985; Liu and O'Donnell, 1997). However, the only significant occurrence of such shallow water constituents was found in the observed

velocity, with MS_f ~0.04 – 0.07 m.s^{-1}, MS_4 ~ 0.05 m.s^{-1} and M4 ~ 0.03 m.s^{-1}. No significant values for the shallow water constituents were found in the observed sea surface elevation.

With regard to subtidal seas surface adjustments, a ~ 9 – 10 day oscillation period was found in the observations with amplitude ~ 0.05 – 0.2 m. The differences in shape, the broadly defined spectral peak and the inability of the model to represent this feature indicates its origins on remotely imposed gradients by coastal or oceanic features.

A linear regression between tidal range and subtidal velocity has satisfactory fitness under dry and wet season conditions, at the mouth of the bay, with the exception of a short interval around neap tides. The amplitude of the residual velocity, ~ 0.05 m.s^{-1}, is consistent with the MS_f amplitude calculated. The absence of this frequency in sea surface elevation shows that the residual currents do not originate from a fortnightly remotely imposed slope. On the contrary, such residuals must be produced locally by the interaction between tidal current and rapidly varying bathymetry. Such effect is referred in Robinson (1983) as tidal rectification. This rectification is in phase with the spring – neaps cycle and the absence of mean sea level change at this frequency implies that the bay's net volume flux due to tidal rectification is zero.

At the inner bay mooring, M01, such an agreement between subtidal velocity and tidal range was absent under wet conditions. However, significant residual currents occur at neap tides following episodes of strong freshwater inflow. The inner bay reacts to these events in a barotropic fashion early in the wet season and baroclinically late in the wet season.

The Delft3D-Flow model simulates accurately residual flow during the dry season, showing the same relation between residual current and tidal range, as in observations, and detailing the representation of the neap tide burst at M05. During the wet season the model overestimates estuarine circulation at neap tides thus

masking the effects of tidal rectification.

During the wet season, the fortnightly signal is overwhelmed by the magnitude of the neap tide bursts (Figure 5:13, c and d) so that background tidal rectification is greatly underestimated.

In terms of the spatial distribution of the residual current, The Delft3D-Flow simulations predicts significantly weaker residuals in the inner bay than at the mouth. Here circulation is depicted as cyclonic, with the NW shallow section exporting water and the SE deep channel importing. During the dry season and in wet season spring tides, these outflowing and inflowing cells occupy the full depth of the water column. However, at neap tides during the wet season the interface between the circulation cells slopes from its vertical position as the estuarine water rises and spreads at the surface while the ocean water does the opposite. In terms of the residual exchange, during the dry season this parameter increases with tidal range whilst in the wet season the opposite occurs.

6 Seasonal Cycle

The seasonal variation of the density, salinity and temperature in Maputo Bay establishes the background on which the shorter timescale dynamical changes take place. Whilst a horizontal density gradient will allow gravitational flow to take part in the circulation, transport under a homogenous density field will have to rely on tidal shear and rectification alone. The existence of a state in which the water column is initially vertically mixed but a significant horizontal gradient is maintained may allow the system to release this accumulated potential in either a transient manner, helped by tidal straining, or in a more permanent one during periods of low background turbulence. Characterising the salinity and temperature seasonal variation will allow to: i) attribute the origin of the density field; ii) use the salinity as a passive tracer to calculate the flushing time (in Chapter 8). Consequently, the present chapter aims to answer the following questions:

- How do temperature and salinity change during the year?

- When and for how long does Maputo Bay stratify?

- Is the stratification controlled by salinity, by temperature or by a combination of both?

Historically there are no records of physical parameters in Maputo Bay that span over one full season. In the course of this project, periodic bay-wide CTD campaigns were carried out surveying the Bay during both wet and dry seasons. The results from these campaigns and the data from the deployed RCM9 current meters are used to answer the questions posed above. In addition, results from the *basecase* simulation are compared with the observational data.

In this dissertation, potential energy anomaly (Φ) is used to gauge the stability of the vertical stratification measured from CTD casts. Φ is defined as the amount of work

required to bring about complete vertical mixing (Simpson *et al.*, 1978) and can be written as:

Equation 6:1 $\Phi = \dfrac{1}{h}\displaystyle\int_{-h}^{0}(\hat{\rho}-\rho)gz\,dz, \quad with \quad \hat{\rho}=\dfrac{1}{h}\displaystyle\int_{-h}^{0}\rho\,dz$,

where ρ is seawater density, h is depth and g acceleration do to gravity.

6.1 Bay average salinity and temperature

Bay averaged values for salinity and temperature were computed using the CTD sampling campaign data. The full tour around the sampling field takes approximately 5 hours. In order to correct for the non-synoptical character of the sampling, velocities at the stations from the Delft3D hydrodynamic model were used to move the sampling stations to their position at high tide. At each sampling date, salinity and temperature at these new positions were interpolated into a 500x500 array, masking out any of the points either above water or not covered by the interpolation method (Figure 6:1). The individual elements of the array were scaled by performing a weighted average as a function of the depth in each cell in relation with the sum of all the depths:

Equation 6:2
$$C_{bay} = \sum_{i=1}^{N} C_i \cdot p_i$$
$$p_i = \frac{H_i}{\displaystyle\sum_{i=1}^{N} H_i} \quad ;$$

Where C is the value of temperature or salinity, i represents the cell index from 1 to $N=500^2$ and H the depth. The results are presented in Figure 6:2 a) and b).
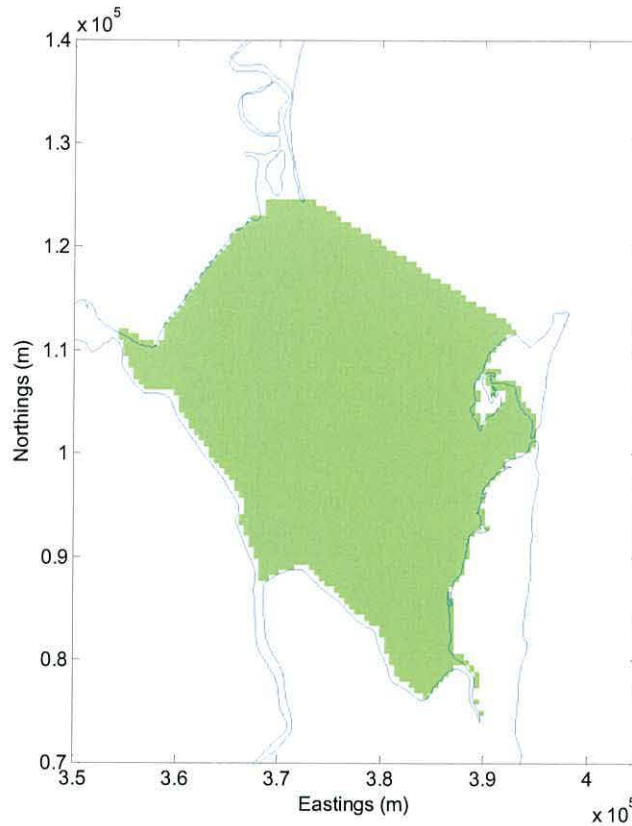
Figure 6:1- Area used for the calculation of bay averaged properties (in green).

The bay averaged temperature was use to calculate the bay's total heat storage (Figure 6:3 c). It is interesting to note that the net heat flux calculated from the temperatures leads ~50 days that of the radiative heat input that should peak near the austral summer solstice at day 354. The heat storage leads by the same amount in relation to the summer equinox, in day 445, reaching a maximum around day 397.

Using the time variation of the bay's heat content, the contribution to rate of change in Φ by surface heating, shown in Figure 6:3 a), can be estimated according to Simpson and Bowers (1981):

Equation 6:3
$$\left(\frac{\partial \Phi}{\partial t}\right)_{heating} = \frac{\alpha g \frac{\partial Q}{\partial t}}{2c_p},$$

where the expansion coefficient $\alpha = 2 \times 10^{-4}$ °C^{-1} and specific heat $c_p = 4 \times 10^3$ J.kg^{-1}°C^{-1}.

The values vary between -7×10^{-6} and 5×10^{-6} W.m^{-3}. When the first freshwater pulse occurs, between days 390 and 393, the heat flux is negligible and hence its contribution to Φ is very close to 0.
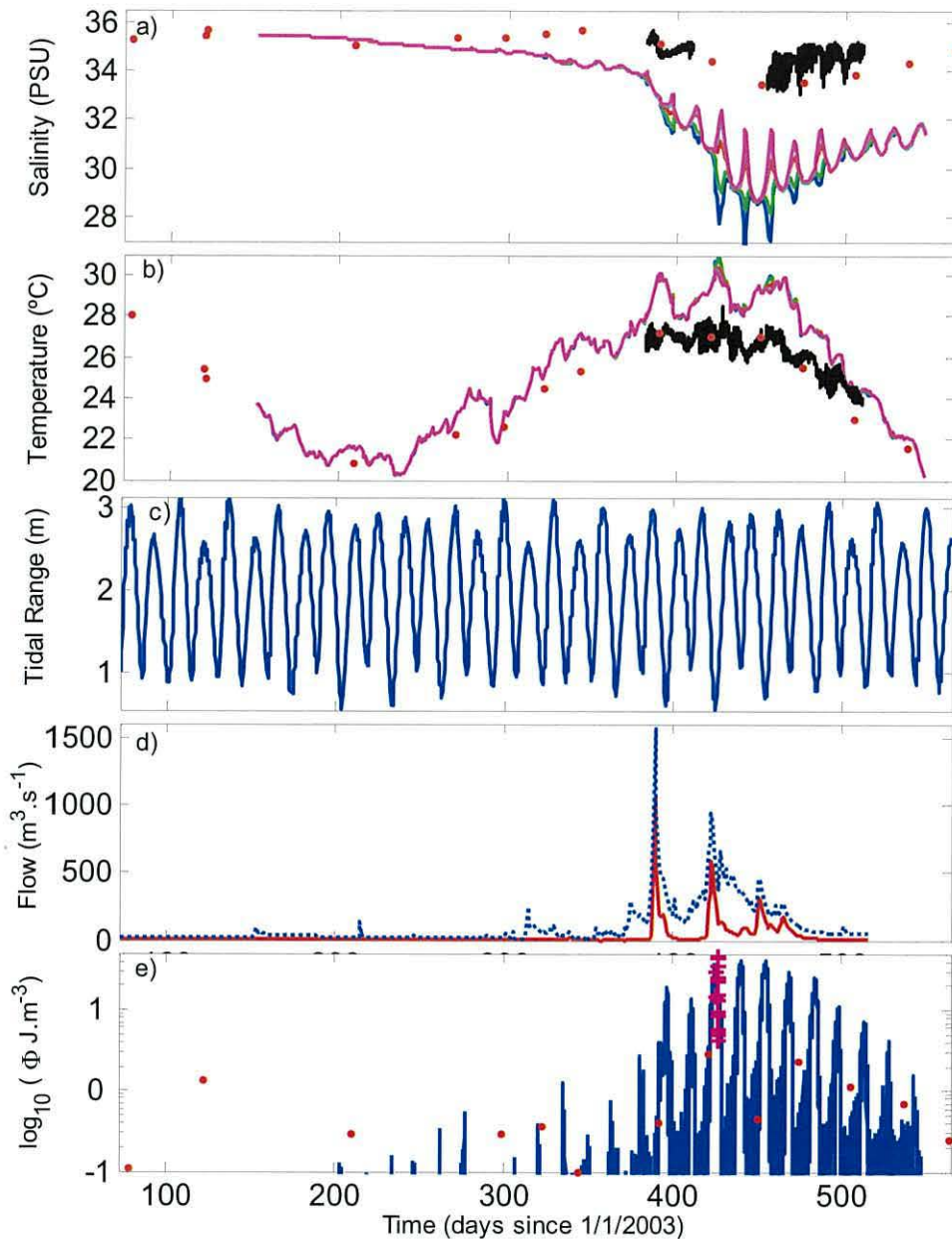
Figure 6:2 - Seasonal evolution of forcing agents and consequent change in salinity and potential energy anomaly in section A compared with Delft3D-Flow *basecase* run: a) bay averaged salinity (coloured lines - Delft3D; dots – CTD observations; black line – M05); b) bay averaged temperature (coloured lines - Delft3D; dots – CTD observations; black line – M05); c) synthetic tidal range from analysis of TG1 data; d) Incomati River flow from Magude river gauge (red line) and input flow for the Delft3D (blue dotted line); e) section mean potential energy anomaly at section A (full line - Delft3D; dots – observations) and section CB (+: spring tides green; neap tides magenta).
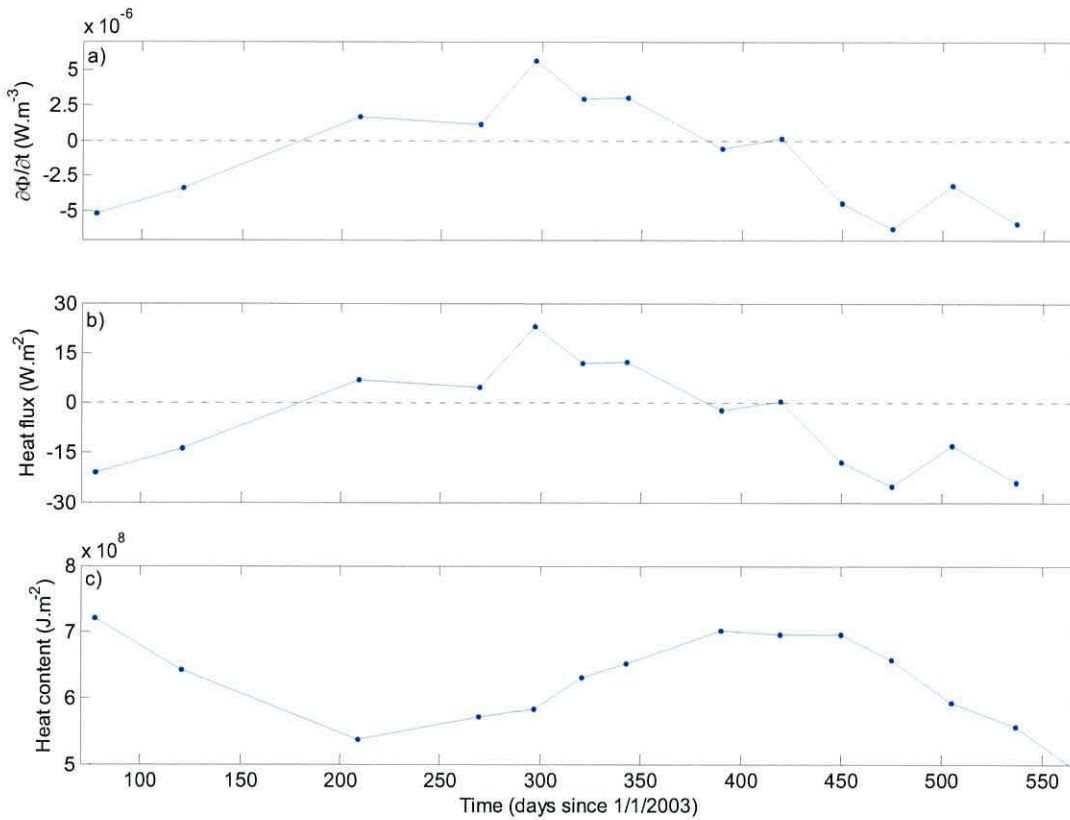
Figure 6:3 – Bay averaged heat seasonal cycle: a) potential energy anomaly rate of change due to surface heating; b) heat flux; c) heat content.

Panel a) of Figure 6:2, shows the available salinity records for the sampled period. During the dry austral winter, the average salinity in the bay stays at values similar to those of the Mozambican Channel. This however changes when the radiative heat flux reaches its peak around day 354. At that time the bay average salinity values increase somewhat, reaching a maximum of 35.6 PSU recorded approximately one month before the first freshwater pulse. This value is 0.4 PSU above the historical maximum salinity recorded on the adjacent shelf (Sete *et. al.*, 2002).

From the first pulse of freshwater at day 390 to day 450 the bay average salinity decreases steadily reaching a minimum of 33.5 PSU at day 450. This represents ~2 PSU difference from the shelf and a correspondent freshwater fraction of 0.056. To reach this minimum requires an approximate mean flow of ~ 70 m^3s^{-1} which is in the same order of magnitude as the measured flow for the Incomati for the same period, ~100 m^3s^{-1}. The contribution to Φ by freshwater uniformly distributed at the surface is 3×10^{-4} $W.m^{-3}$, according to Equation 6:4.

Equation 6:4
$$\left(\frac{\partial\Phi}{\partial t}\right)_{fw} = \frac{g}{2}\dot{P}\Delta\rho\,,$$

where $\dot{P}$ is the river flow distributed as rainfall with units m.s^{-1} and $\Delta\rho = 25$ kg.m^{-3} the difference in density of fresh and salt water (Simpson *et. al.*, 1990).

After this maximum bay-shelf salinity difference at day 450, the bay average salinity increases from then onwards, in spite of one last freshwater pulse.

6.2 Boundary conditions

As it was noted in the averaged salinity signal, there is an early summer salinity surplus in the bay in relation to the shelf. The following analysis of the interaction between the salinity rise and temperature has to rely mainly on the temperature sensors mounted on the two RCM9's at M05 due to the lack of precision in the salinity sensors.

In Figure 6:4 (page 66), the top to bottom difference in temperature, $\Delta T = T_{top} - T_{bottom}$, is plotted together with salinity and elevation. The three combinations of phase-to-high water and signal of ΔT found are represented.

In early summer (Figure 6:4, first column), the bay is a negative estuarine system where the salinity maximum occurs at low water. At that time, the peak in $|\Delta T|$ occurs at low water and the bottom water is warmer, hence more saline.

After the first freshwater pulse event, the bay becomes a positive estuarine system, where the salinity maximum occurs at high water. At this time (Figure 6:4, second column) the bottom water was colder.

Later in the wet season (Figure 6:4, third column), the bay has changed state again. It has evolved from an unbalanced environment, where freshwater was injected abruptly, into more stable conditions where the stored freshwater is now being slowly flushed. Now, whilst keeping the positive estuarine nature, ΔT is negative and $|\Delta T|$

maximum occurs at low water.

It is postulated that the build up of warmer, more saline water inside the bay is related to intensive evaporation in the shallow and intertidal areas away from the freshwater sources. These freshwater sinks are flooded at high water, exchanging their water properties with the rest of the bay. This relation was found in similar conditions by Hoguane *et. al.*(1999) and Lencart e Silva (2001), in Saco the Inhaca and Ria Formosa, respectively. This water is denser than the ambient water and warmer, thus justifying the heat signature found with higher temperature at the bottom. However, the signal found in Maputo Bay is very weak and near the limit of detection of the instruments. This together with the absence of data for the southeast region of the bay, the more likely region for presence of hyper-saline conditions, renders unclear the origin of the temperature anomaly. Furthermore, the excess in salinity inside the bay was never connected to a significant bay-shelf density gradient (see Section 6.3).
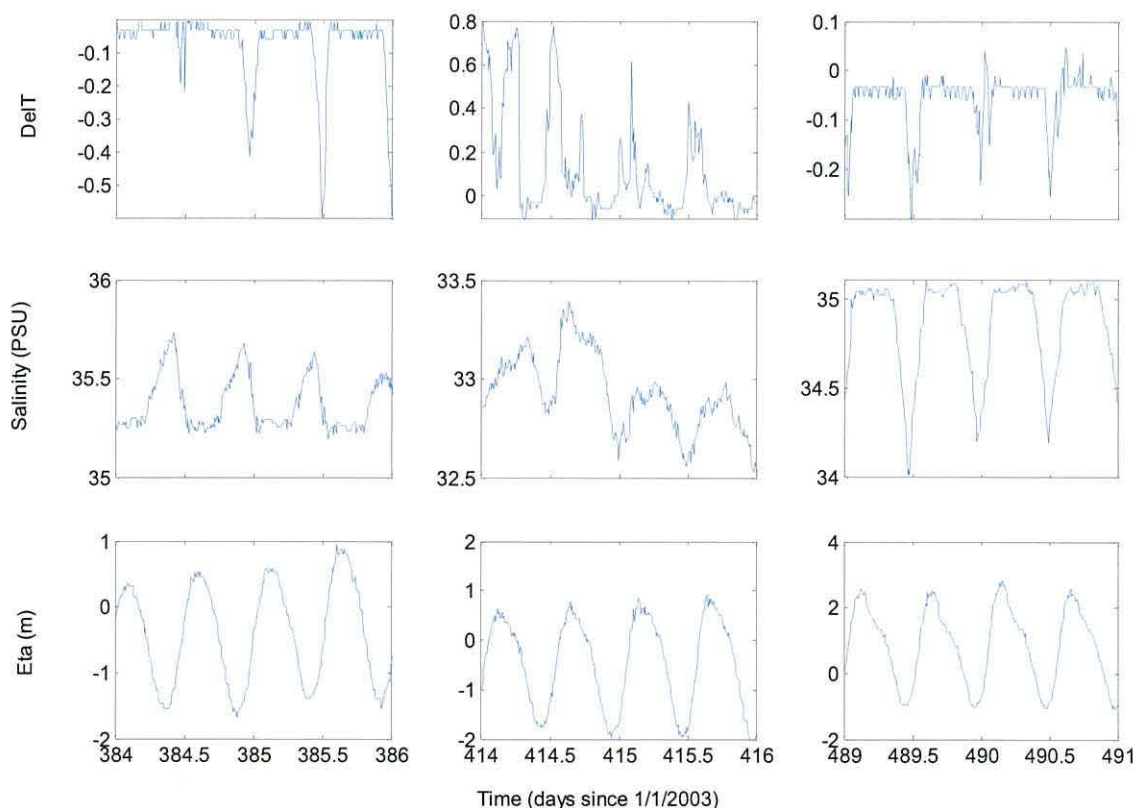
Figure 6:4 – Evolution of ΔT in three typical periods at M05. ΔT in the 1st row, salinity in the second row and sea surface elevation in the 3rd.

6.3   Water column density structure

In order to assess the bay's change in density structure during the 15-month sample period, the CTD sampling done in section *A* is analysed. In addition to spanning the bay's full breadth, this line was sampled on all the CTD campaigns, making it the most representative for this analysis.

The CTD campaigns were carried out under spring tide conditions. In periods of slow change in the freshwater input, *i.e.* during the dry season, the monthly sampling can be considered a significant value for that period. Nevertheless, due to the spring-neaps cycle, the mixing is not constant and therefore the Φ calculated should be considered as the monthly minimum. During the wet season, this value should be viewed as an instant measurement of the water column structure in the bay.

Panel e) of Figure 6:2 shows the calculated Φ for section *A*. The values show that the bay is almost completely mixed during the dry season. With input of freshwater between day ~400 and day ~525, the average stratification increases to a peak of 80 $J.m^{-3}$ observed during a survey at neap tide on day 426.
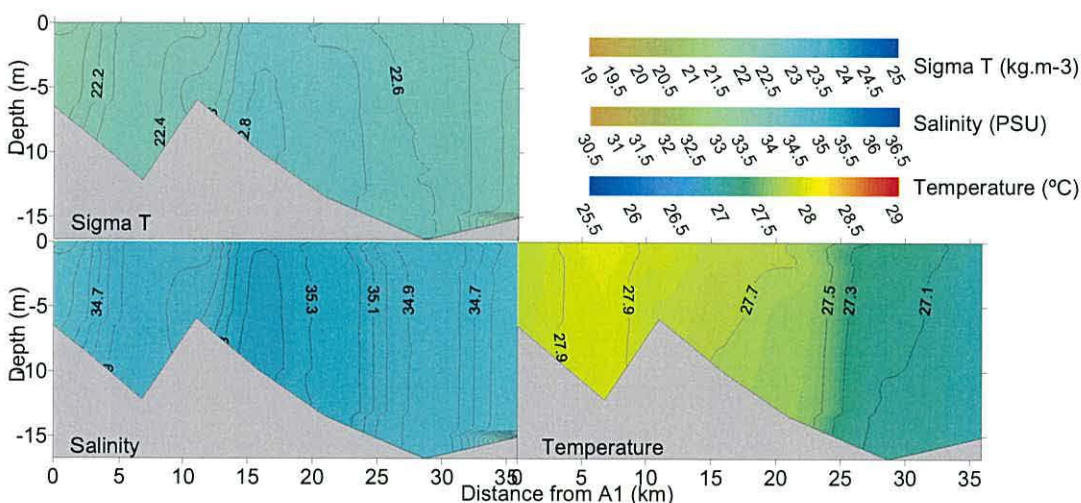
Figure 6:5 – CTD survey of section A during spring tide in dry conditions at 26/01/2004, 390 days since 1/1/2003.

As it was shown in Section 6.1 the surface distributed buoyancy due to heating is very low, contributing to Φ at a maximum rate of $5 \times 10^{-5} \, W.m^{-3}$.

There is, however, a possible secondary effect of heating altering the density structure in the bay. Due to its shallow bathymetry, Maputo Bay has less heat storage capacity than the adjacent shelf. Also due to this difference in depth, stirring will more rapidly mix the heat accelerating the early peak in storage, as observed. Hence, it could be expected that the bay-shelf temperature gradient arisen from this would drive a horizontal density gradient much like freshwater does in an estuary. At around day 380 there was as much as 0.9 °C difference in ~ 15 km between the inner bay and the mouth, amounting to a density gradient of 2×10^{-5} kg.m^{-4}, if only temperature is considered. However if the salinity excess is taken into account, with the bay registering 35.75 and the shelf 35.25 PSU, the gradient becomes positive inshore and diminishes to ~ 3×10^{-6} kg.m^{-4}.

To substantiate the fact that temperature does not play a significant role in setting a density gradient, Figure 6:5 depicts a fully mixed water column on all the three parameter and no significant horizontal gradients. This section was taken at day 390 during springs and the last day of the dry summer when heat storage was near its peak, with the bay starting to cool.

From this evidence, it is possible to infer that if there is some stratification due to deferential heating in the shallow part of the bay, this phenomenon is transient and does not hold in with an increase in tidal stirring.

6.4   Delft3D-Flow results

The numerical model represented well the trend in the temperature cycle and the low heat flux periods but during the summer, the model overestimated the temperature by as much as 3 °C.

In comparison to the measured data, the simulated bay starts to freshen too early in the season. This early start may be attributed to modelled flow for the Maputo River.

As it can be seen in panel d) of Figure 6:2 (page 63), the freshwater flow series (blue line) used as input in the *basecase* run starts to discharge water in the bay well before the first recorded pulse of freshwater in the Incomati (red line).

With a head start of approximately 1.5 PSU deficit at the first freshwater pulse recorded, the simulation has a steeper decrease in salinity when compared to the recorded in the CTD campaigns.

Hyper-saline conditions were not mirrored by the *basecase* simulation using Delft3D, where evaporation was not included in the salt mass continuity equation, being used only to account for latent heat loss. This can explain some of the early decrease in bay averaged salinity, the opposite of the recorded trend.

The *basecase* run represented well the seasonal change in stratification and was reasonably accurate in representing Φ at neap tides. There is however, a noticeable over-estimation of mixing by the model during spring tides, resulting in significantly lower Φ values than recorded.

6.5   Summary of main results

The seasonal temperature cycle in Maputo Bay shows a peak in heat flux ~50 days before the summer solstice and the equal heat storage lead in relation to the summer equinox. The bay averaged temperature spans from 28 °C on 28/03/2003 to 20 °C on 28/07/2004.

Towards the end of the wet season the salinity in Maputo Bay was observed to fall as low as 2 PSU bellow the salinity of the adjacent ocean. The bay averaged salinity ranges from 35.7 PSU in day 343 to 33.5 in day 450. During early summer episodes of hyper-saline conditions up to 0.5 PSU above the adjacent ocean salinity were observed.

Stratification in Maputo Bay follows the salinity cycle reaching a maximum of 80

J.m^{-3} of Φ at neap tides during the wet season, when the freshwater fraction of the bay is near its maximum. Observations show that both surface distributed heat and bay-shelf differential heating were weak contributors to stratification during the dry season. Heat is also a negligible contributor to Φ during the wet season since maximum heat storage was attained 7 days after the first freshwater inflow.

The Delft3D-Flow *basecase* run shows a satisfactory representation of the seasonal temperature and stratification cycles but overestimates the bay's salinity deficit.

7 Buoyancy and Tides

The problem of the buoyancy-stirring competition in the presence of a spreading buoyant plume differs from the classical heat-stirring problem since the source of buoyancy is being distributed as a function of its gradient whereas in the case of uniform surface heating, the source is fixed (Simpson *et al.* 1990).

Linden and Simpson (1988) show that vertical mixing inhibits the development of density currents and, when mixing is switched on and off for equal times, the exchange through a cross-gradient section increases with the period of the mixing cycles. Additionally, In large estuaries and ROFIs, research (e.g. Fujiwara *et al.*,1997) has shown that the fate of the density field is controlled not only by buoyancy and tidal forcing but by the system's morphology as well .

It was shown in Chapter 6 that the bay experienced the strongest stratification during the period between 400 and 525 approximately mainly due to freshwater input. It was also shown the important fortnightly change in tidal forcing of Maputo Bay. Consequently, this chapter aims to answer the following questions:

– What are the differences in stratification between neap and spring tides?

– How do the different buoyancy and stirring terms interact to generate the semidiurnal stratification cycle observed?

To answer them, the semidiurnal CTD campaigns at the mouth of the bay (CB sections, Figure 3:1 page 6) are analysed together with the current at M05, in search for patterns in the density field. These two semidiurnal cycles of CTD profiling were taken at days 417 and 421 well into the wet season and when full heat storage was achieved (Chapter 6). Next, a schematic model is built to gauge the relative importance of the several buoyancy and stirring terms.

7.1   Bay-shelf interface

In Figure 7:1, the properties of the water across the CB section are plotted in T-S diagrams. The figure shows that during spring tide the oceanic water, cooler and saltier, intrudes further into the Delagoa Bight reaching the bay. This is felt in stations CB1 and CB2 whilst the northwest stations CB3, CB4 and CB5 record a warm and fresher signature characteristic of the inward bay.
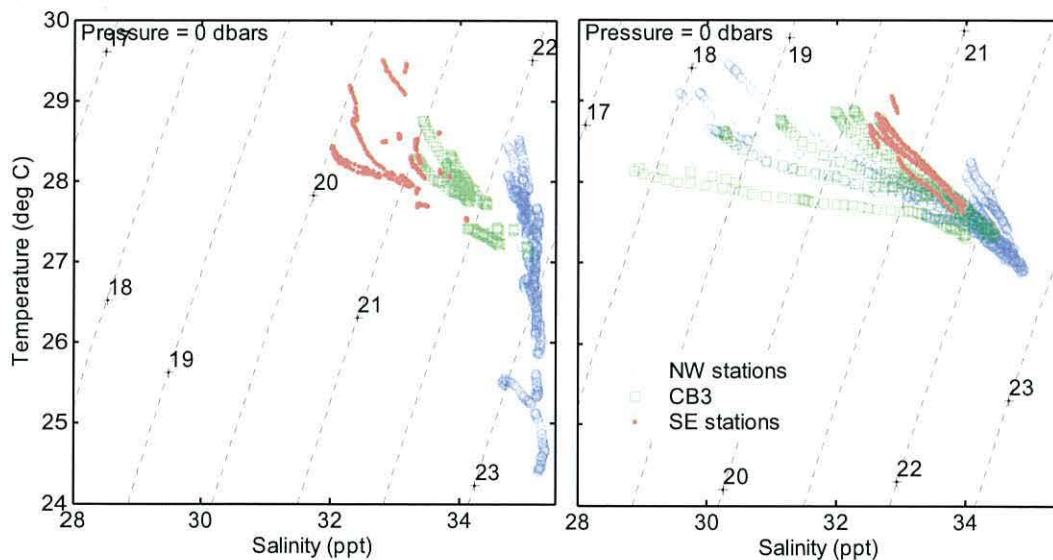
Figure 7:1 – Temperature, salinity plots depicting the water properties in 3 different regions of the mouth of Maputo Bay (CB1 and CB2 in blue; CB3 in green; CB4 and CB5 in pink). Left panel: spring tide tidal cycle campaign. Right panel: neap tide tidal cycle campaign.

In relation to the vertical distribution of properties, southeast stations CB1 and CB2 show that, when it occurs, stratification is mainly thermally driven whilst the northwest stations and CB3 show combination of haline and thermal stratification.

7.1.1   The semidiurnal campaigns

In Figure 7:2 and Figure 7:3 (pages 75 and 76), the observed stratification is represented through Φ. This is plotted alongside salinity and temperature from CTD casts and velocity measured at M05 (near CB2).

Under neap tide conditions, the water column was found to be stratified throughout the section during the 6 hours of sampling. Within this period, the currents were 2 to 3 times weaker than under spring tide conditions and Φ was greater by an order of

magnitude reaching 78 J.m^{-3} (Figure 7:2). The neaps campaign was shortened due to technical problems so that only half of the tidal cycle was sampled, but all evidence points to a persistence of strong stratification throughout the tidal cycle. With regard to the temperature and salinity characteristics of the water, the neap tide campaign shows warmer and fresher water, with its strong stratification mainly due to differences in salinity (Figure 7:1).

The spring tide survey begins near high water with some significant stratification, ~15 J.m^{-3} encountered in the deep part of the transect (CB2, Figure 7:3). When tidal velocity reaches its maximum, the structure has been eroded to give a completely vertically-mixed water column as shown by the near to zero values of potential energy anomaly. Near low water slack, stratification develops throughout the section enduring longer in the deepest part of the transect (~10 J.m^{-3}). During the following flood, stratification is again eroded throughout the section, reappearing only in the deepest part near high water.

Three main features should be noted, that:

i)   the transient stratification observed at the end of the ebb coincides with the maximum top to bottom displacement in the density up-gradient direction;

ii) the asymmetry about low-water in the density cycle where stratification was eroded faster during the flood;

iii) the sudden stratification at high-water due to temperature

This suggests that the observed stratification mainly results from the tidal straining of the horizontal density field during the ebb and to advection of temperature stratified water from the shelf during high water.

Since density was only sampled in the across-bay axis, there is an ambiguity between locally produced and advected stratification. To solve this, the following section uses

a schematic model to test if the observed stratification could be produced locally.
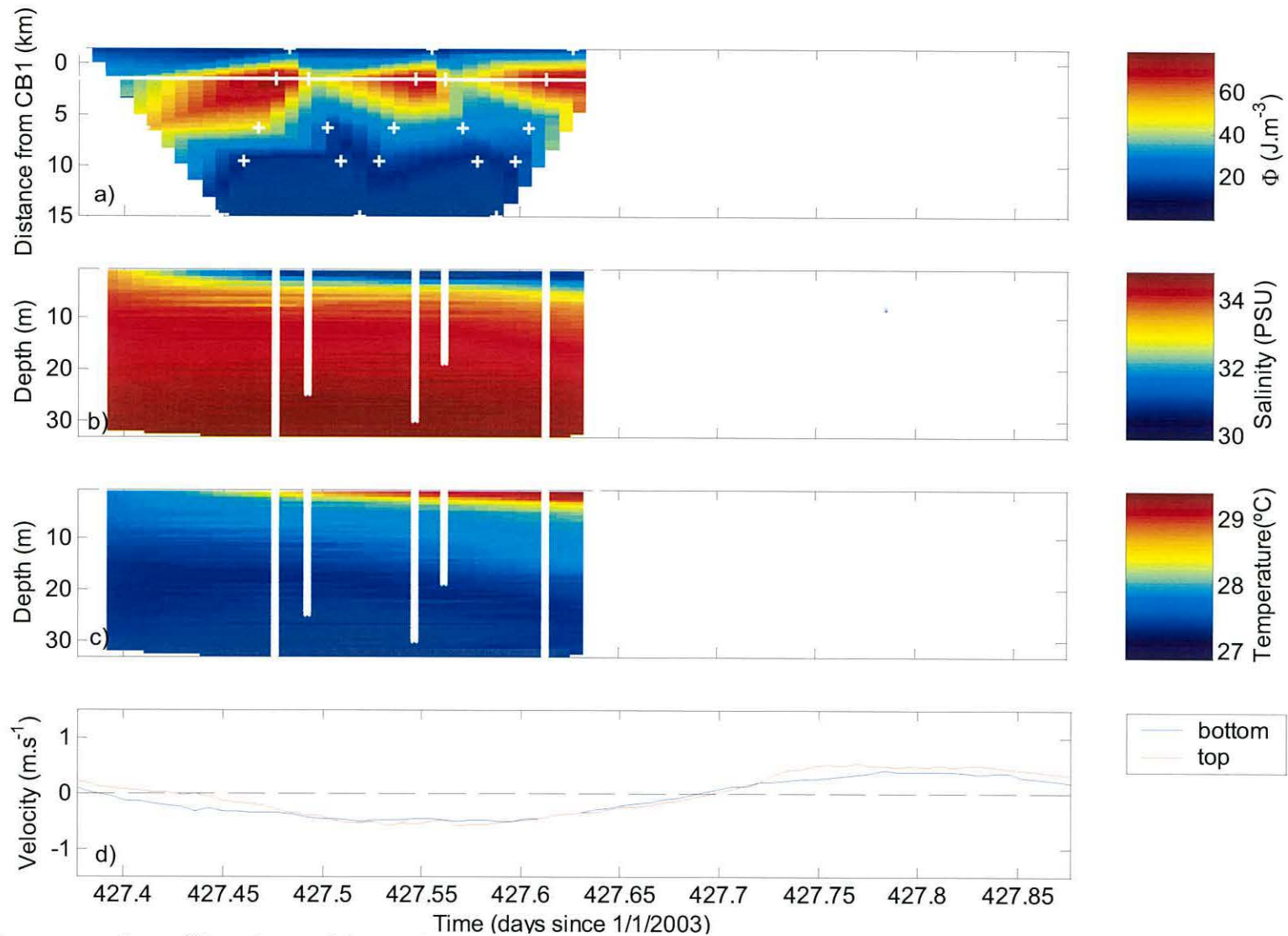
Figure 7:2 – Water column properties at CB section semidiurnal tidal cycle during neap tide: a) potential energy anomaly variation. b) salinity profile at M05(CB2); c) temperature profile at M05(CB2); d) velocity at M05 marked in white across the top panel (red - bottom current meter, blue – top current meter).
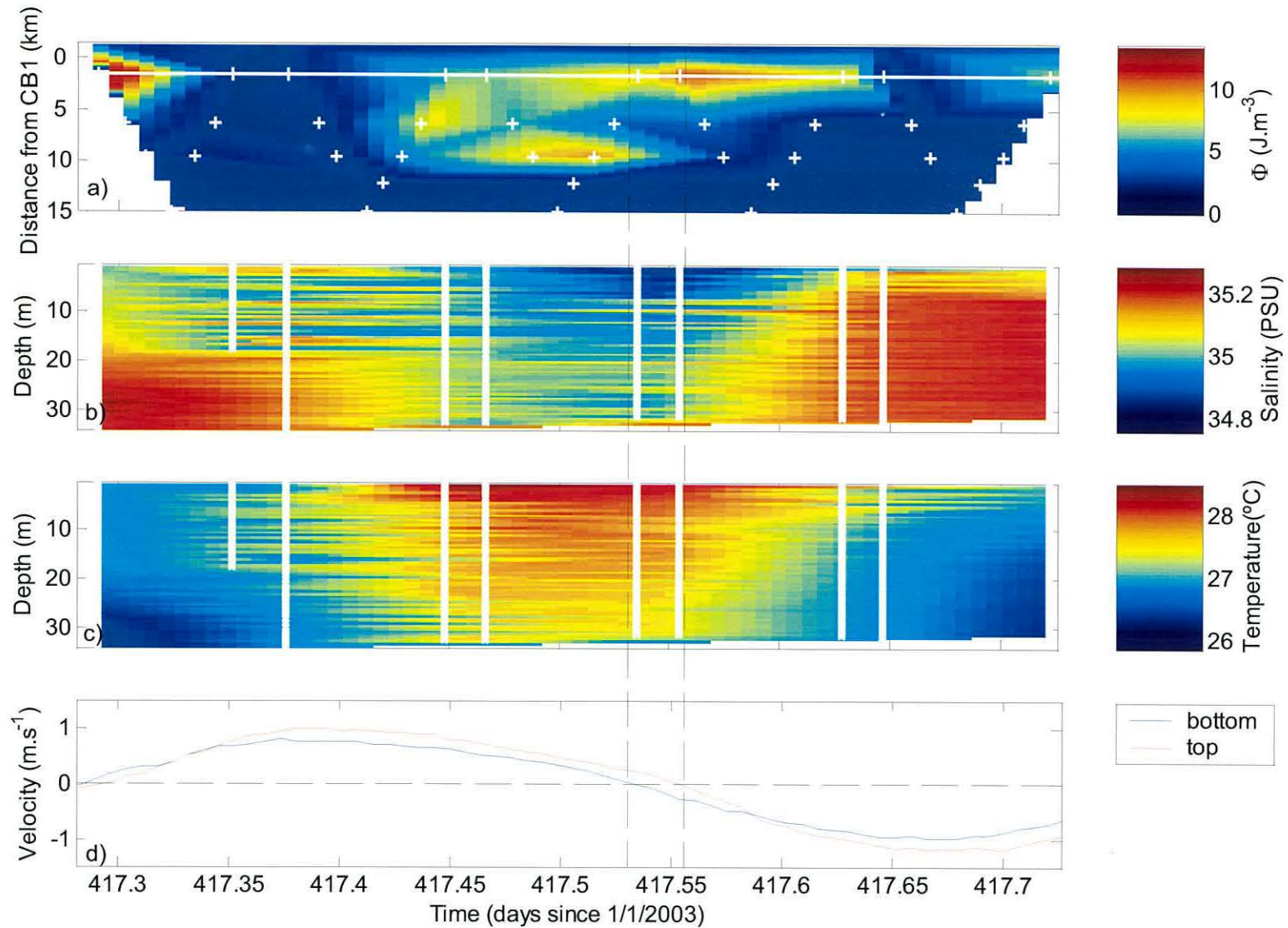
Figure 7:3 – Water column properties at CB section semidiurnal tidal cycle during spring tide: a) potential energy anomaly variation. b) salinity profile at M05(CB2); c) temperature profile at M05(CB2); d) velocity at M05 marked in white across the top panel (red - bottom current meter, blue – top current meter). Vertical lines mark low water slack.

7.1.2 The terms in the buoyancy-stirring equation

The local importance of straining is tested in a schematic model of stratification where all terms in the buoyancy-stirring equation are compared.

Following Simpson *et. al.* (1990), the positive contributions to Φ come from buoyancy input from heating, pycnocline intensification by velocity shear due to estuarine circulation and tidal straining of the density field. The negative contributions come from bottom tidal mixing, surface wind mixing and convective overturning from the action of the tidal velocity profile over the density field in the down-gradient direction. For the present model, the heating term was disregarded since full heat storage capacity of the bay was already attained at the time of the semidiurnal campaigns. These terms are expressed in Equation 7:1.

Equation 7:1
$$\frac{\partial \Phi}{\partial t} = \left(\frac{\partial \Phi}{\partial t}\right)_{STR} + \left(\frac{\partial \Phi}{\partial t}\right)_{E} - \left(\frac{\partial \Phi}{\partial t}\right)_{Mixing}.$$

For the straining term, a velocity profile is obtained from the top current meter at M05 using the Bowden and Fairbairn (1953) parameterisation and extracting from it the depth averaged velocity, $\hat{u}$:

Equation 7:2
$$u(\zeta) = \hat{u}(a - b\zeta^2),$$

with a=1.15; b=0.425 and $\zeta = z/h$.

Considering the horizontal density advection $\frac{\partial \rho}{\partial t} = -u\frac{\partial \rho}{\partial x}$ and assuming a depth independent $\frac{\partial \rho}{\partial x}$,

Equation 7:3
$$\frac{\partial \hat{\rho}}{\partial t} = -\hat{u}\frac{\partial \rho}{\partial x}.$$

Taking the time derivative of Equation 6:1 (page 61) and substituting,

Equation 7:4
$$\frac{\partial \Phi}{\partial t} = \frac{g}{h}\frac{\partial \rho}{\partial x}\int_{-1}^{0}(u - \hat{u})z \ dz.$$

The value for $\dfrac{1}{\rho}\dfrac{\partial \rho}{\partial x} = 1.4 \times 10^{-7}\, m^{-1}$ was found by taking the density gradient along the major axis of the tidal ellipse, calculated using the depth averaged density difference between high water and low water casts divided by the tidal cycle excursion during the same period inferred from the top RCM9 at M05. Substituting Equation 7:2 in Equation 7:4 and integrating,

Equation 7:5
$$\left(\frac{\partial \Phi}{\partial t}\right)_{STR} = 0.031 gh\hat{u}\frac{\partial \rho}{\partial x}.$$

For the estuarine circulation term, velocity can be represented using a steady state flow equation that balances the pressure gradient against frictional forces (Officer, 1976),

Equation 7:6
$$u(\zeta) = \frac{gh^3}{48 N_z \rho}\frac{\partial \rho}{\partial x}(1 - 9\zeta^2 - 8\zeta^3).$$

Substituting in Equation 7:4 and integrating over depth,

Equation 7:7
$$\left(\frac{\partial \Phi}{\partial t}\right)_E = \frac{1}{320}\frac{g^2 h^4}{N_z \rho}\left(\frac{\partial \rho}{\partial x}\right)^2,$$

with $N_z = 3.3 \times 10^{-1}\hat{u}h$, following Bowden (1953).

The mixing terms according to Simpson and Bowers (1984) can be expressed as:

Equation 7:8
$$\left(\frac{\partial \Phi}{\partial t}\right)_{Mixing} = \varepsilon\kappa\rho\frac{|\hat{u}|^3}{h} + \delta\kappa_s \rho_s \frac{|W|^3}{h},$$

where according to Simpson *et. al.* (1991), $\varepsilon=0.0038$ and $\delta=0.039$ are mixing efficiencies by tide and wind respectively. The drag coefficient on the sea-bed $\kappa=0.0025$ and at the surface $\kappa_s = 6.4 \times 10^{-5}$.

The terms in Equation 7:1 were forward integrated from $\Phi = 0$ at t=417.35 when the water column was totally mixed.
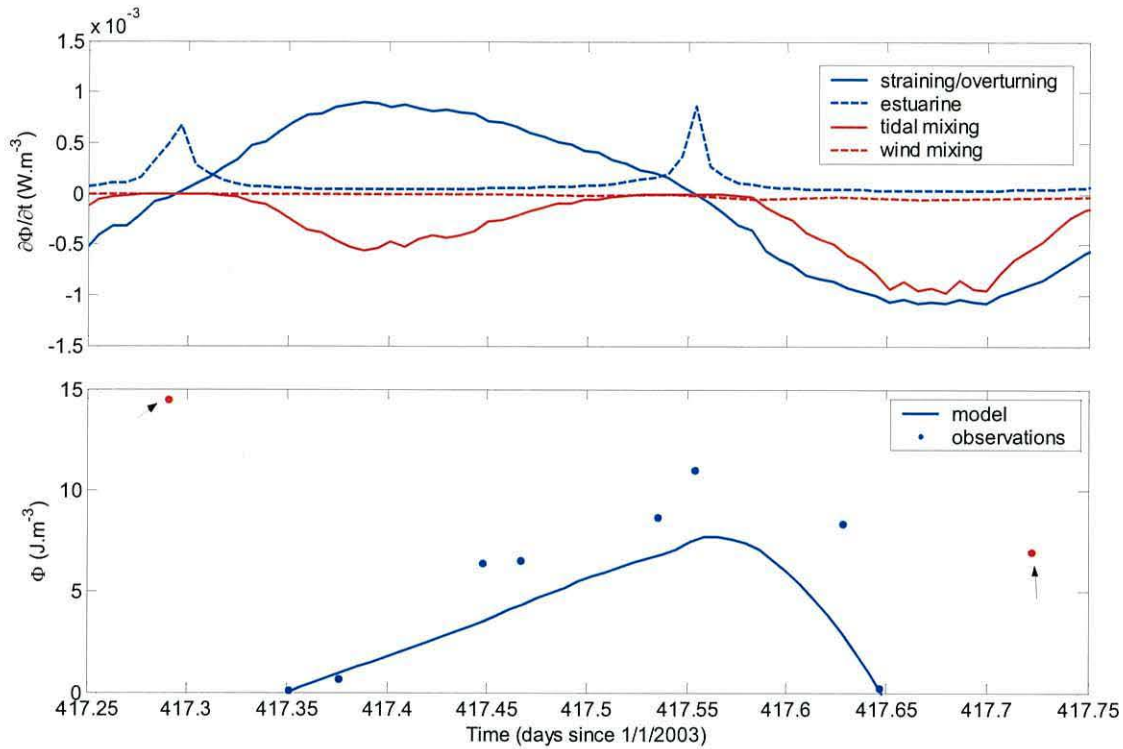
Figure 7:4 – Φ model results: top panel: comparison of each of the terms of Equation 7:1; bottom panel: Φ model and observations compared; points marked in red correspond to shelf water characteristics.

In Figure 7:4 top, the separate contributions to $\dfrac{\partial \phi}{\partial t}$ are plotted showing that the main contribution is given by tidal straining. Φ was calculated by forward integration of Equation 7:1. In the bottom panel, the modelled Φ is plotted together with observations. The simulated results (blue line) describe reasonably well the behaviour of the observed Φ (dots). Taking into consideration that far-field advection is not included in the model, these results show that:

– the observed Φ is explained both in magnitude and in phase by the local cycle of production and erosion of stratification;

– the local Φ cycle is mainly due to the straining term with some contribution of estuarine circulation to the production of stratification and tidal stirring to the erosion of stratification.

The already mentioned stratification asymmetry about low-water is reproduced by the model. This can only be explained by including tidal straining and overturning. This

process creates stratification against tidal stirring during the ebb and erodes stratification with tidal stirring during the flood, thus causing the asymmetry Φ production in Equation 7:1. The eventual ambiguity between Φ locally produced and advected from the inner bay is resolved, given that the latter would be symmetrical about low-water.

The only symmetry about low-water is found in the high-water structures, the same that the model cannot explain locally (Figure 7:4, red dots). Additionally, the timing of these structures coincides with the maximum excursion into the bay. Hence, these can only be occurrences of stratified shelf water advected from the Delagoa Bight.

7.1.3   Delft3D-Flow results

Figure 7:5 and Figure 7:6 (pages 81 and 82) show the water properties and structure for the Delft3D-Flow *basecase* run. In comparison to the observations the model shows higher mixing being able to completely erode the stratification during spring tides (maximum of 2 $J.m^{-3}$) and showing periodic stratification at neap tides with a maximum ~80 $J.m^{-3}$. Despite the considerable velocity shear during springs, the salinity and temperature structures are symmetrical about low water slack, implying that unlike the field results, the mixing and stratification is not due to the interaction between the velocity shear and the horizontal density gradient but to advection. During neap tides, asymmetry about low water is present in the stratification hinting to a degree of strain-induced periodic stratification, SIPS (Simpson *et al.*, 1990), represented by the Delf3D-Flow model. This result cannot be compared with observations given that the flood part of the tidal cycle is absent from the respective field survey.
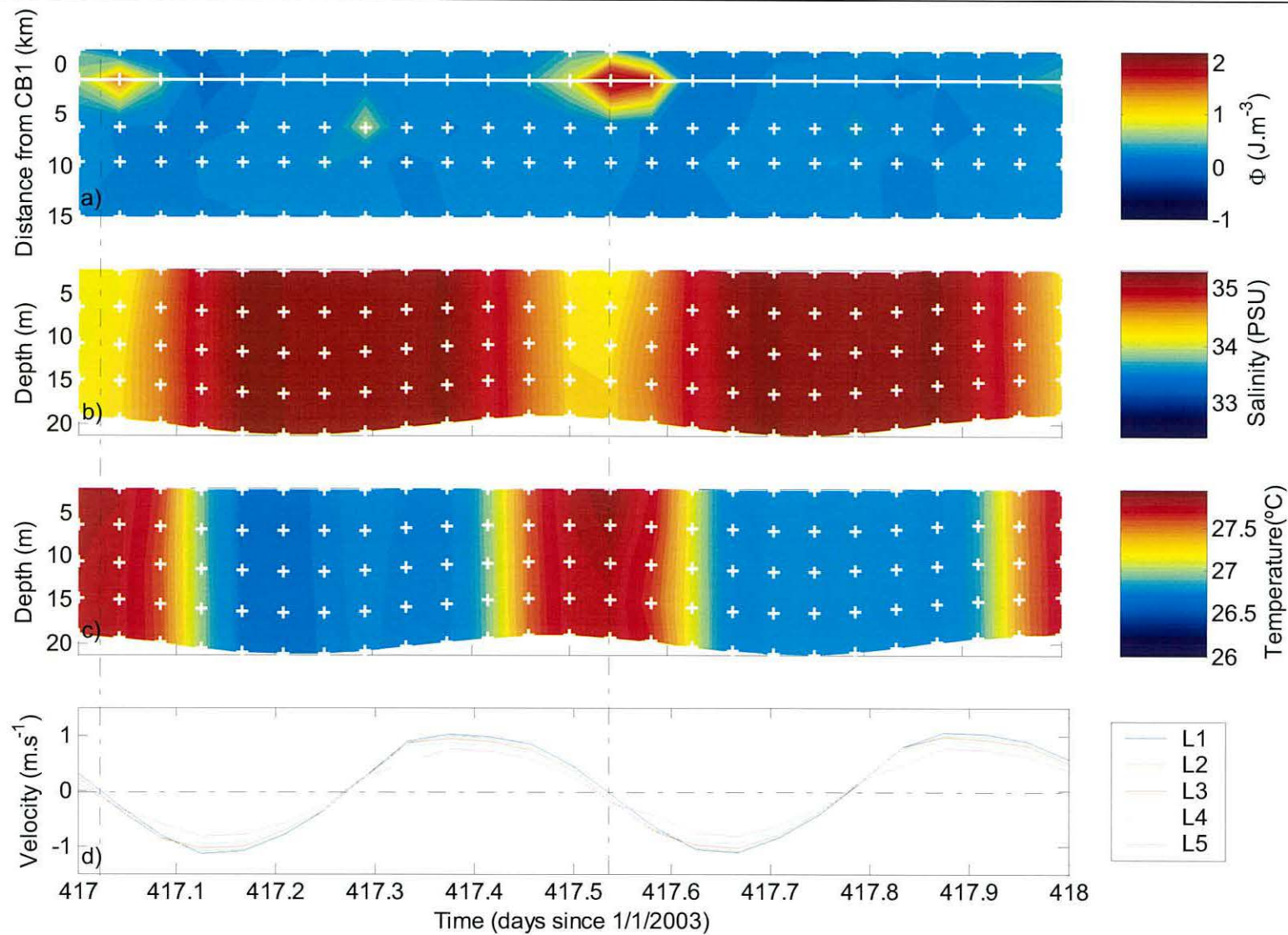
Figure 7:5 – Delft3D-flow *basecase* results for water column properties at CB section semidiurnal tidal cycle during spring tide: a) potential energy anomaly variation. b) salinity profile at M05(CB2); c) temperature profile at M05(CB2); d) velocity at M05 marked in white across the top panel (RCM9 top =L2,L3 and RMC9 bottom = L4,L5). Vertical lines mark low water slack.
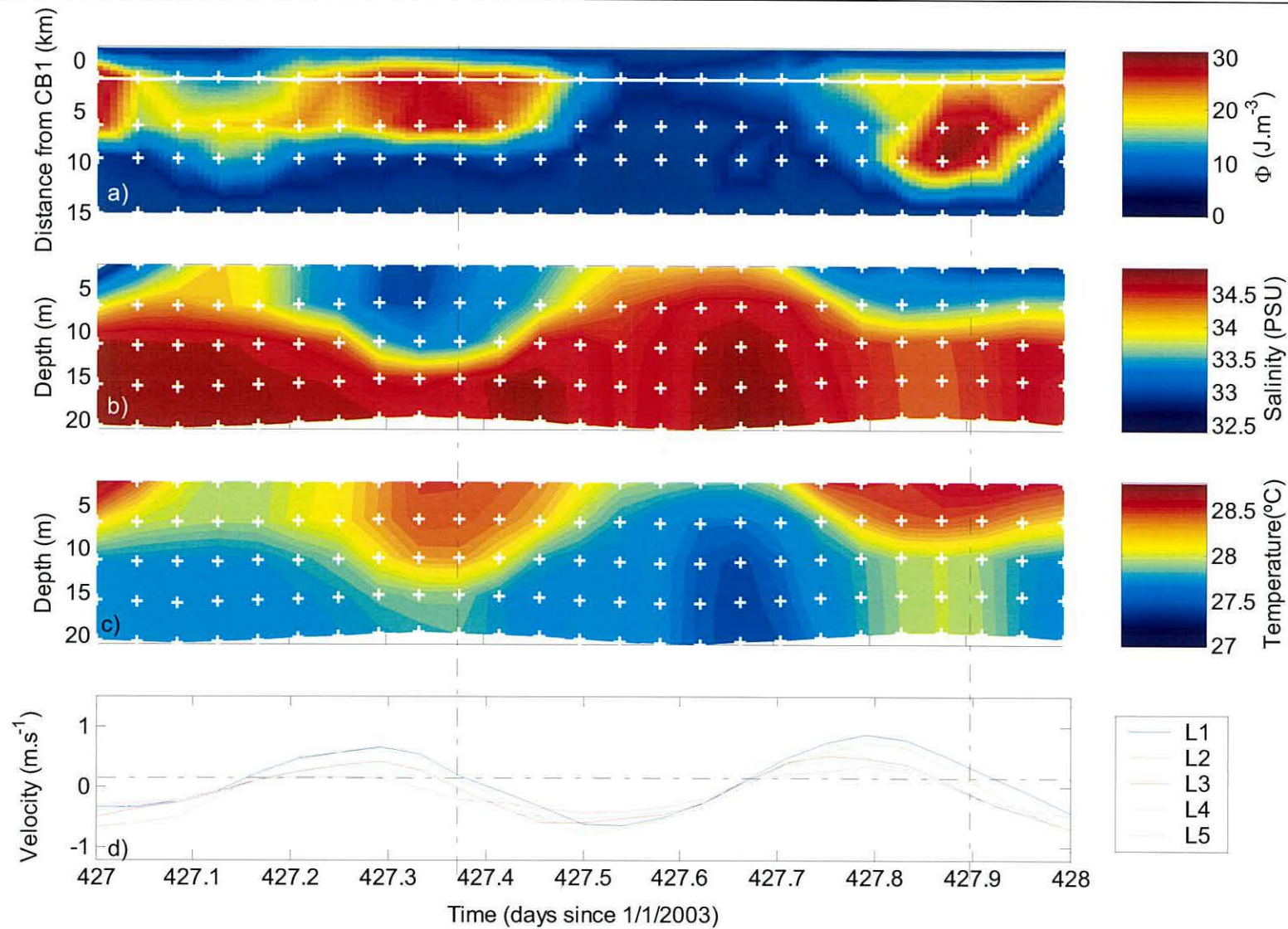
Figure 7:6 – Delft3D-flow *basecase* **results for water column properties at CB section semidiurnal tidal cycle during neap tide: a) potential energy anomaly variation. b) salinity profile at M05(CB2); c) temperature profile at M05(CB2); d) velocity at M05 marked in white across the top panel (RCM9 top =L2,L3 and RMC9 bottom = L4,L5). Vertical lines mark low water slack.**

7.2   Summary of main results

The values of the potential energy anomaly vary greatly from neaps to springs. The 3-fold increase in recorded velocities is reflected in a reduction of ~1 order of magnitude, with Φ varying from ~78 J.m^{-3} during neaps to a maximum of 15 J.m^{-3} during springs.

During spring tides, observations and the schematic model show that: i) the observed Φ is explained both in magnitude and in phase by the local cycle of production and erosion of stratification; ii) the local Φ cycle is mainly due to the straining term; and that the hypothesis of an advective inner bay origin for the stratification can be refuted.

In comparison to the observations the Delft3D-Flow *basecase* run shows higher vertical mixing during spring tides (maximum of Φ 2 J.m^{-3}) and periodic stratification at neap tides with a maximum ~80 J.m^{-3} which is probably due to SIPS.

8 Modelling the flushing time of Maputo Bay

A central question of potential practical importance in Maputo Bay concerns the flushing time, which is a measure of the time required to replace a set fraction of the bay's volume of water. This information is relevant to determine the fate of dissolved substances in the bay and specially vital in case of a sudden contaminant spill. To know how the flushing time varies with different conditions of forcing helps to determine the system's vulnerability at its multiple dynamical states.

From the previous chapters it becomes clear that the main transport forcing is carried out by tide and river runoff. Under near-steady-state salinity conditions, it would be expected transport to be explained by a combination of these forcers. This concept is tested for Maputo Bay in three steps. First, a background value of flushing time is calculated using the observed salinities. The method will yield a wet season mean flushing time value. Next, to understand the implications of varying the two main forcing factors, the Delft3D-Flow platform is used to test the bay's flushing time response to a near-steady-state ensemble of tidal and freshwater conditions. Finally, using a demonstrative box model, tidal shear diffusion is investigated in its relevance to flushing.

The three models presented here address the flushing time in terms of the decay of the bay-mean concentration C of a passive tracer. This decay is assumed to follow first order kinetics so that:

Equation 8:1
$$\frac{\partial C}{\partial t} = -\frac{Q}{V}C,$$

where QC is the total exchange flux across the mouth and V the system's volume. This decay is exponential if Equation 8:1 is integrated with respect to time from the initial concentration C_i:

Equation 8:2 $$C = C_i e^{-\frac{Q}{V}t}.$$

If the time scale $\tau = \dfrac{V}{Q}$ is taken as the flushing time, this represents the time when

$C = e^{-1} C_i$.

8.1 Tidal prism model

In the first approach based on observations, a modified tidal prism model is used to calculate flushing time. To achieve this result, the tidal prism salinity model is first calibrated to the observed salinity using a retention parameter. Flushing time is then derived from the calibrated model.

Dyer (1973) and Officer (1976) refer to a tidal prism model that during the flood part of the tidal cycle the volume, P, of seawater with coastal salinity entering an estuarine system is fully mixed with the bay volume V and the river volume R entering the system. Furthermore, they assume that P and R are fully removed during the ebb.
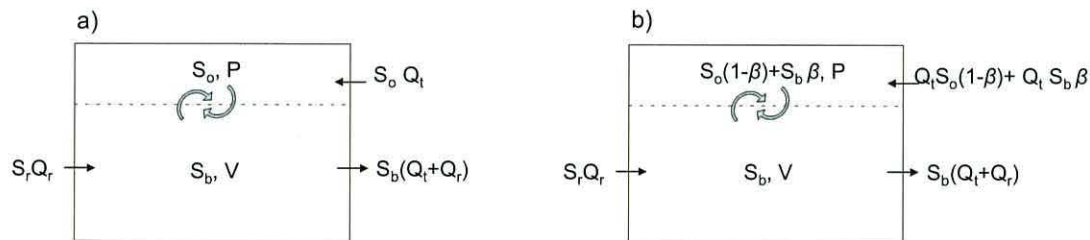
Figure 8:1 – Schematic representation of the Tidal prism model: a) classical configuration; b) with retention coefficient.

Consider a box bay with volume V and salinity S_b connecting to a river with no salinity ($S_r = 0$) and to the open shelf with salinity S_o (Figure 8:1, a). Assume also that:

- the bay adjusts to the change in river flow, Q_r, flow in less than one tidal cycle so that its volume is conserved subtidally ($\partial V / \partial t = 0$);

- the tidal prism volume P enters and exits the bay with no asymmetries, with flow Q_t, every 12.421 hours.

- the water entering the bay is fully mixed within one tidal cycle and that P is

solely composed of shelf water with S_o salinity.

Under these conditions, every tidal cycle the salt flux into the bay is:

Equation 8:3 $\qquad\qquad Salt_{in} = S_o Q_t$

and the salt flux out is:

Equation 8:4 $\qquad\qquad Salt_{out} = S_b(Q_t + Q_r)$,

so that for the classical tidal prism model the salinity rate of change in the bay at each

high water is:

Equation 8:5 $\qquad\qquad \dfrac{\partial S_b}{\partial t} = \dfrac{S_o Q_t - S_b(Q_t + Q_r)}{V + P}$.

In Figure 8:1 b), the same box model is depicted with an added retention parameter β

to account for the return of a fraction of the bay's water from the previous cycle. P

has now salinity equal to $S_o(1 - \beta) + S_b\beta$.

With this modification the salinity rate of change is:

Equation 8:6 $\qquad\qquad \dfrac{\partial S_b}{\partial t} = \dfrac{S_o Q_t(1 - \beta) + S_b Q_t\beta - S_b(Q_t + Q_r)}{V + P}$.

As in Dyer (1973) and Officer (1976), the tidal prism model proposed here views the

system at tidally averaged rates of change.

To calibrate the tidal prism model to the observed salinities, Equation 8:6 was written

in its numerical form and forward integrated with the only free parameter, β, adjusted

to fit the modelled results to the salinity observations (Figure 8:2, a).

The volumes of the tidal prism were calculated using a hypsometric curve obtained

from the available bathymetry. The freshwater flow Q_r was obtained from gauged

data in the Incomati and modelled data in the Maputo River. V was taken as the

volume of the bay at the minimum tidal elevation recorded. The salinity was modelled

from 01/01/2003 to 31/05/2004 and the simulations bracketed β between 0.8 and 0.9

with some agreement.

Ideally, a passive tracer should be used to calibrate the tidal prism model. In the present case, salinity was the only conservative parameter available. However, as it was shown in previous chapters, the dynamical conditions in the bay change when salinity drops, in turn changing the flushing characteristics of the bay. Thus, β can only be tuned to the wet season salinities, hence the model is considered calibrated to the wet season mean dynamical properties.
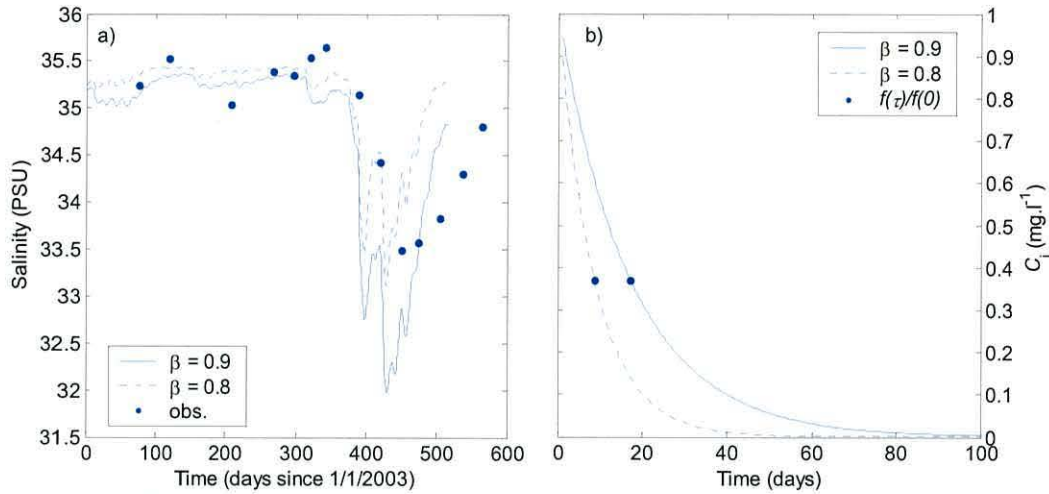
Figure 8:2 – Tidal prism model results of bay-wide depth-averaged salinity. a) Model fitting: observed salinity from tidally corrected CTD casts (blue dots), model results with β=0.8 (dashed) and β=0.9 (full). b) Equation 8:10 applied for β=0.8 (dashed) and β=0.9 (full) the dots represent concentration at flushing time, $C(\tau)=e^{-1}C_i$.

To calculate the flushing time a timescale is derived for the values of β found to bracket the observations. Using the tidal prism model, the bay is filled with a passive tracer with initial concentration C_i=1 mg.l^{-1}.

The passive tracer fluxes, F, then become:

Equation 8:7
$$F_{in} = C_o(1-\beta)Q_t + C_bQ_t\beta + C_rQ_r$$
$$F_{out} = C_b(Q_t + Q_r)$$

so that the rate of change of tracer concentration in the bay is given by

Equation 8:8
$$\frac{\partial C_b}{\partial t} = C_o \frac{Q_t(1-\beta)}{V+P} + C_rQ_r - C_b\left(\frac{Q_t(1-\beta)+Q_r}{V+P}\right).$$

Assuming that $C_r=C_o=0$ in the river and shelf water, the first and second terms of Equation 8:8 vanish and

Equation 8:9

$$\frac{\partial C_b}{\partial t} = -C_b \left(\frac{Q_t(1-\beta)+Q_r}{V+P} \right);$$

$$\frac{\partial C_b}{\partial t} + \alpha \, C_b = 0; \quad \alpha = \left(\frac{Q_t(1-\beta)+Q_r}{V+P} \right).$$

Assuming V, Q_r and Q_t to be constant, the integration of C_b with respect to time yields:

Equation 8:10 $\quad\quad\quad\quad\quad C_b = C_i e^{-\alpha t}.$

At constant flow and boundary conditions, Equation 8:10 describes the tracer in the bay decaying exponentially towards equilibrium concentration at a time constant τ,

Equation 8:11 $\quad\quad\quad\quad \tau = \frac{1}{\alpha} = \frac{V+P}{Q_t(1-\beta)+Q_r},$

where τ is the time that takes for the passive tracer concentration to reach $1/e$ of the initial condition, the measure of flushing time proposed in the beginning of the chapter.

To calculate the wet season mean τ, the mean values for 2003-2004 wet season used were: Q_r=120 m^{3}s^{-1} (Incomati observations plus Maputo modelled data); Q_t=4.24x10^4 m^{3}s^{-1} (the average tidal flow); and V=5.6x10^9 m^3. Substituting in Equation 8:11, $\tau \approx 9$ and 17 days for $\beta = 0.8$ and 0.9 respectively (Figure 8:2, b).

The use of a tidal prism model has the advantage of being the most direct way of obtaining a reference flushing time value based on observations. On the other hand, apart from the obvious morphological simplifications, the tidal prism model treats the bay as a fully mixed system, overlooking the density driven flow and the interaction between the buoyancy input and the stirring produced by the tides. To achieve a more authentic representation of these processes, a full physics 3-dimensional model is needed where the density and flow fields are explicitly modelled.

8.2   Delft3D-Flow model

The use of 3-dimensional modelling with the best available bathymetry should allow

the simulation of the density field including changes due to advection. There are fundamental differences between systems where buoyancy is gained due to point freshwater input and others where this is done uniformly through surface heating. In the classic surface heating case, the buoyancy source is independent of the flow whilst in the ROFI paradigm, the spreading of a buoyant plume – as a result of the density driven flow – advects the source of buoyancy through the system. Adding to this, phenomena such as tidal rectification and tidal straining can only be simulated using a fine grid model. This model has to be capable of representing the interactions between rapidly varying bathymetry and the tidal currents in the case of rectification. In the case of straining, it needs to represent three-dimensionally the interaction between the tidal sheared currents, the density field and the bathymetry. To achieve this, the modelling has to be done at a fine enough scale that allows for the simulation of frontal structures thus created (Chao, 1990; James, 1997).

The basic setup emerging from the final calibrated model in Chapter 4 was used in the idealised simulations for the calculation of flushing time. In these runs, the forcing was modified to populate a 3-dimensional space where flushing varies with tidal range and freshwater input.

Freshwater flow was maintained constant during each run at the following values: 0, 200, 800, 3200 m^3s^{-1}. Tidal forcing was limited to an M_2 wave and the velocity amplitude was kept constant throughout each simulation with scenarios run for 0.05, 0.25, 0.65 and 1.05 $m.s^{-1}$. A passive tracer was distributed uniformly inside the bay and at all depths, covering the area in Figure 6:1 (page 62), with no additional tracer added during the simulation. The concentration of the tracer was measured each 2 hours in the bay. Flushing time was again calculated assuming an exponential decline of the tracer inside the bay. Rearranging Equation 8:10:

Equation 8:12
$$\ln C = -\alpha\ t + \ln C\,|_{t=0};\quad \alpha = \frac{1}{\tau},$$

and plotting the base e log of the concentration against time, the line found should have a slope of $-1/\tau$, where τ is once more the time that takes for the passive tracer concentration to reach $1/e$ of the initial condition.

Flushing time, τ, was calculated by least squares fitting the simulated passive tracer concentration to Equation 8:12. This procedure was applied to a 5-day running window at each time step for the full run and the result used only after a stable value of τ was reached. An example of the method is illustrated in Figure 8:3 for tidal velocity amplitude $U_{M2} = 0.25$ m.s^{-1} and freshwater flow Q_r=3200 m^{3}s^{-1}. In Figure 8:3 a), the window used for the final calibration is marked in green and the remaining values of the series of C is plotted in blue dots. The linear model resulting from the least squares fit is plotted in red. In Figure 8:3 b), the flushing time for each 5-day window is plotted in blue and the final stable value in green. The stability condition was not met for the pairs (U_{M2}, Q_r)={(3,0); (3,3200)}, i.e. for maximum tidal range with both no freshwater flow and maximum freshwater flow. In these cases the system did not converge to steady state within the run time available for the simulation.
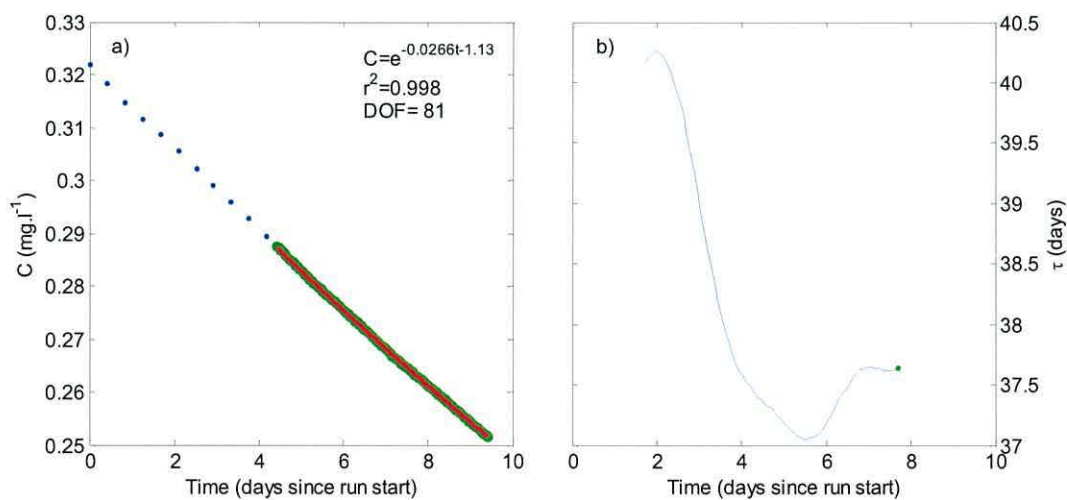
Figure 8:3 – Flushing time calculation for U_{M2}=0.25 m.s^{-1} and Q_r=3200 m^{3}s^{-1}: a) concentration of passive tracer, C, as function of time (unused data blue dots, used data in green, regression model in red); b) variation of flushing time using a 5-day running window (unused data in blue and used value in green).

In Figure 8:4, the resulting 16 flushing times are mapped against their modelled tidal

velocity amplitude and freshwater river discharge. Several response patterns can be identified in Figure 8:4. Flushing increases with forcing when factors act separately. The lowest value of τ =24 days occurs at maximum river runoff while a minimum of τ = 37 days is found at maximum tidal forcing with no river runoff. This indicates a greater exchange efficiency of buoyancy driven flow in comparison with tidal diffusive and advective processes.

For every value of river runoff greater than $\sim 10^2$ m^3.s^{-1}, the rise in tidal forcing has the initial effect of extending τ, further rise in U_{M2} causes flushing time to decrease reaching a local minimum at maximum tidal range. Throughout the plain in Figure 8:4 there are examples of non-linear progression of τ with the increase of one of the forcing terms. For example, for maximum U_{M2}, τ increases initially with Q_r to ~ 45 days and then decreases from $\sim 10^2$ m^3.s^{-1} onwards.

In terms of the wet season mean flushing time, the Delft3D-Flow result for $Q_r \sim 10^2$ m^3.s^{-1} and $U_{M2} \sim 0.6$ m.s^{-1} is ~ 50 days.
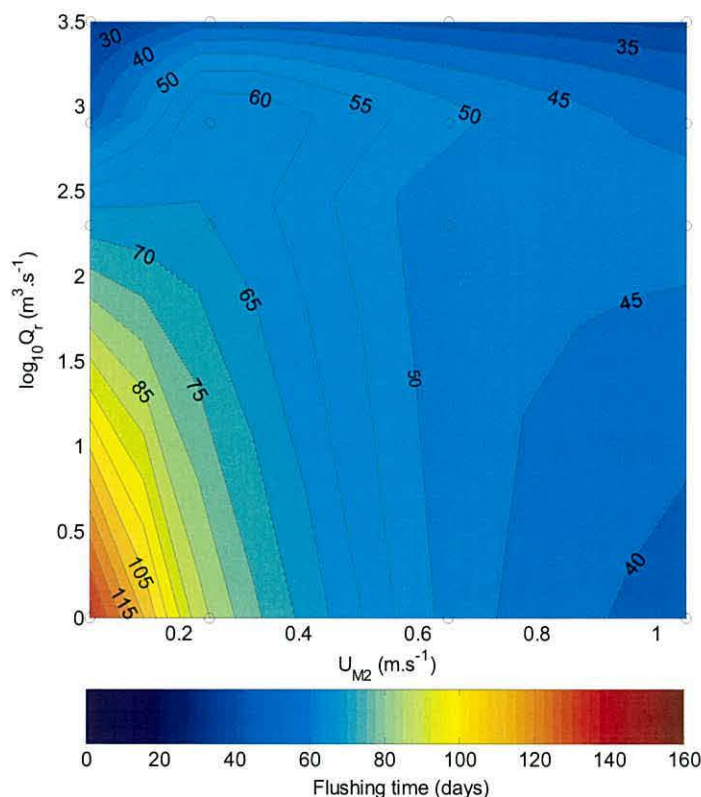
Figure 8:4 – Delft3D-Flow flushing time calculation results: flushing time τ plotted against tidal velocity amplitude and freshwater discharges.

These results show that, although flushing increases with both controls separately, there are regions where tidal stirring seems to interfere in the buoyancy driven circulation, thus reducing flushing relatively to cases with the same amount of freshwater but with lower stirring.

8.3 Diffusive box model

Using the analysis of the observed and modelled density structure behaviour under different tidal and freshwater input condition as a starting point, deductions can be made on the mechanisms controlling that structure and consequent exchange characteristics. During the dry season, in the absence of a density structure, the transport mechanism must be largely due to tidal shear dispersion and residual tidal rectification. By contrast, when freshwater input is high and stirring is weak, the ventilation of the bay is done by flow associated with the gravitational circulation (Hansen and Rattray, 1965). In between these two extremes, stirring and buoyancy compete for the principal role in the flushing. To illustrate the relative importance of tidal shear diffusion, a flushing model was devised where horizontal diffusion is dependent on tidally oscillating vertically sheared currents and the steady-state salinity gradient, leaving out estuarine circulation and all advection processes such as tidal rectification and straining.
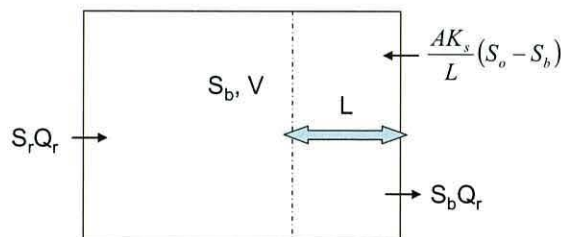
Figure 8:5 – Schematic representation of the diffusive box model of Maputo Bay.

Consider a rectangular region of volume V open to the ocean at one end where the salinity is S_o and fed with freshwater from a source at the opposite end as in Figure 8:5. If the river discharge is at a rate Q_r with $S_r=0$, volume conservation requires that an equal volume of water leaves the bay with the bay's salinity S_b. This loss of salt is

assumed to be opposed by a diffusive input with diffusivity K_s through a cross-sectional area A so that the equation for salinity is just :

Equation 8:13
$$V \frac{\partial S_b}{\partial t} = \frac{A K_s}{L}(S_o - S_b) - Q_r S$$

where L is the distance over which the salinity difference acts. Equation 8:13 can be written as :

Equation 8:14
$$\frac{\partial S_b}{\partial t} + \alpha S_b - \beta S_o = 0$$
$$where \quad \alpha = \frac{Q_r + A K_s / L}{V}, \quad \beta = \frac{A}{VL} K_s,$$

which has a solution:

Equation 8:15
$$S_b = \frac{\beta S_o}{\alpha} + B e^{-\alpha t},$$

where B is a constant set by the initial conditions. If, as in the previous models, the bay is filled with a passive tracer with initial concentration $C_{i=1}$ mg.l^{-1}, if $C_o = C_r = 0$ mg.l^{-1} and loss by diffusion across the river-bay interface is considered negligible, Equation 8:13 simply becomes:

Equation 8:16
$$\frac{\partial C_b}{\partial t} = -\frac{K_s A / L + Q_r}{V} C_b$$

as the terms containing C_o become null. The solution of Equation 8:16 is Equation 8:10 with the difference that now

Equation 8:17
$$\tau = \frac{1}{\alpha} = \frac{V}{K_s A / L + Q_r},$$

still remaining the time taken for $C_b = (1/e)C_i$.

To estimate K_s, exchange is assumed to be dominated only by tidal shear diffusion in which case the diffusivity, according to Fisher *et. al.* (1979), will be controlled by:

Equation 8:18
$$K_s = \frac{u_t^2 h^2}{4 \pi^2 k_z} = \gamma \frac{\hat{U}^2 h^2}{k_z},$$

where u_T is a measure of the shear in the tidal stream assuming a cosine velocity profile, h is the depth, k_z is the vertical eddy diffusivity and the constant $\gamma = 1.01 \times 10^{-3}$ relates u_T to the depth mean tidal stream velocity, $\hat{U}$, via a tidal velocity profile (Bowden and Fairbairn, 1953).

The vertical eddy diffusivity under well mixed conditions is taken as $k_{z0} = 3.3 \times 10^{-1} \hat{U} h$ (Bowden, 1953). Under stratified conditions, the diffusivity is reduced by buoyancy forces, an effect which is represented through the Richardson number parameterisation of Pacanowski and Philander (1981).

Equation 8:19
$$k_z = \frac{k_{z0}}{(1 + 5 Ri_E)^3}$$

where the Richardson number is assumed to be an estuarine Ri defined as:

Equation 8:20
$$Ri_E = g \frac{\Delta \rho}{\rho} \frac{Q_r h}{2\varepsilon \, c_d A_b \hat{U}^3} = b \frac{Q_r}{\hat{U}^3},$$

where $\Delta \rho$ is the density difference between freshwater and water in the open sea and A_b is the area of the embayment over which it is assumed that the incoming buoyancy due to Q_r is distributed. The factor ε is a mixing efficiency representing the fraction of energy available for increasing the potential energy of the water column (Simpson and Bowers, 1981) and $c_d = 2.5 \times 10^{-3}$ the drag coefficient.

With these assumptions, K_s can be determined and hence the parameter τ for the case of diffusive exchange by shear diffusion. The result using representative numerical values for Maputo Bay (Figure 8:6), where $b = 1.1 \times 10^{-4}$ s^{-2}, show how the flushing time varies with the runoff rate Q_r and the amplitude of the tidal stream $\hat{U}$. For low $\hat{U}$ and low runoff τ is very large, >200 days, but decreases dramatically as Q_r increases above 30 m^3 s^{-1}. At low values of runoff, flushing increases with $\hat{U}$ as expected, but at high Q_r the rise in $\hat{U}$ decreases flushing.
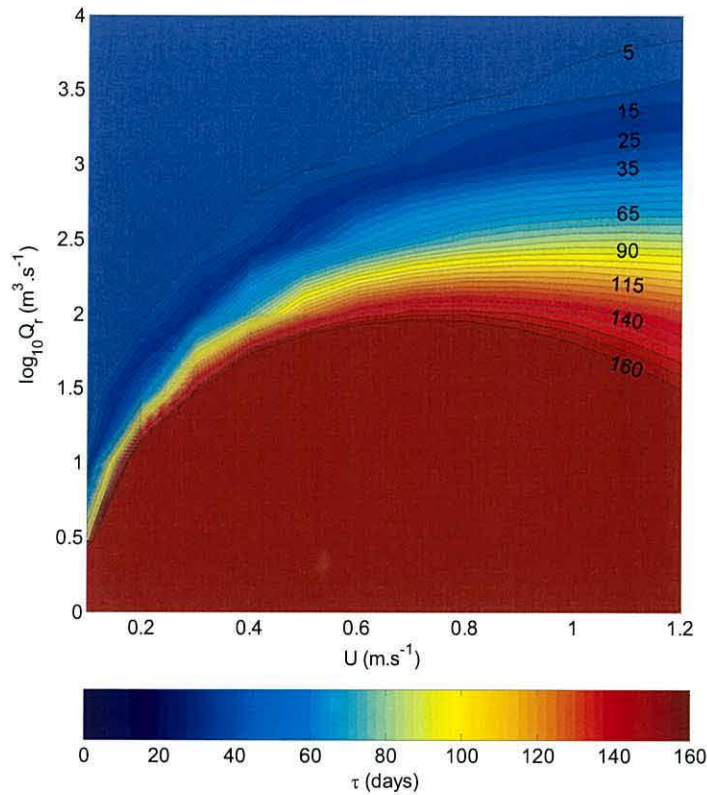
Figure 8:6 – Diffusive model results for K_s. Flushing time τ plotted against tidal velocity amplitude and freshwater discharges.

Generally the flushing times are too long $(\sim 10^2$ days) for $(\hat{U}, Q_r) = (0.6 m.s^{-1}, 10^2 m^3 s^{-1})_r$ in relation to the estimates of the wet season τ obtained from observation $(\sim 9 - 17$ days) even though the tidal shear values used in constructing Figure 8:6 are increased by a factor of 2.2 relative to the Bowden profile. When freshwater was absent, conditions for which the Delft3D-Flow model is most reliable, the diffusive box model predicted $\tau > 160$ days against ~ 70 days of the numerical model. The clear inference is that tidal shear dispersion alone cannot account for the flushing of the bay, and that the advective processes associated to tidal rectification play a major role in the exchange between the shelf and the bay

8.4 Summary of main results

Three models are presented which address the flushing time in terms of the exponential decay of the bay-mean concentration C of a passive tracer.

A tidal prism model was used to calculate the wet season mean flushing time, τ, using

the mean values for 2003-2004 wet season. This yielded $\tau \approx 9$ and 17 days for a return

fraction of bay water $\beta = 0.8$ and 0.9 respectively.

The Delft3D-Flow calibrated model was used to populate a 3-dimensional space

where flushing varies with tidal stream velocity and freshwater input. A passive tracer

was distributed uniformly inside the bay and at all depths, with no additional tracer

added during the simulation, and flushing time τ was calculated by least squares

fitting the simulated passive tracer concentration to the expected exponential decay

curve. Flushing is shown to increase with forcing when factors act separately. The

lowest value of $\tau = 24$ days occurs at maximum river runoff while a local minimum of

$\tau = 37$ days is found at maximum tidal forcing with no river runoff. This indicates a

greater exchange efficiency of buoyancy driven flow in comparison with tidal

diffusive and advective processes. For every value of river runoff greater than $\sim 10^{2.5}$

$m^3.s^{-1}$, the rise in tidal forcing has the initial effect of extending τ, further rise in U_{M2}

causes flushing time to decrease reaching a local minimum at maximum tidal range.

The Delft3D-Flow experiments show a wet season mean flushing time of ~ 50 days,

$\sim 3 - 6$ times longer than the value returned by the observational based calculations.

A demonstrative diffusion box model is presented starting by applying tidal shear

diffusion at the bays mouth. In comparison to the Delft3D-Flow experiment, tidal

shear diffusion was shown to account for only a fraction of the transport during the

dry season, implying that the advective processes associated to tidal rectification play

a major role in the exchange between the shelf and the bay.

9 Summary and discussion

This dissertation used observations and complementary modelling to determine the main controls on exchange in Maputo Bay. Previous observational work was limited to a small amount of uncoordinated series of elevation and current data together with occasional density profile sampling. The observational effort undertaken in the course of this PhD programme strived to present the first coordinated characterisation of the circulation dynamics in Maputo Bay, sampling for 15 month continuously water properties and dynamics with a limited amount of moored instruments and performing regular surveys to determine the season evolution of the density field. These objectives were only partially attained, thus a set of modelling exercises were undertaken to fulfil the observational gaps.

9.1   Principal findings

One of the most remarkable aspects of the oceanography of Maputo Bay is the large neaps springs variation in tidal forcing as noted in previous observational studies for surface elevation (Hoguane *et. al.*1999) and velocity (Saide, 1995). The tide here is strongly semidiurnal and the relatively small value of the M_2 tidal constituent, in relation to the rest of the semidiurnal constituents, results in the observed high spring to neaps ratio of $\sim 0.5 - 3$ m in height range and $\sim 0.1 - 1.3$ m.s^{-1} in velocity amplitude. The energy dissipated trough bottom roughness follows this rise in velocity from $\sim 10^{-4}$ Wm^{-3} in neap tides to $\sim 10^{-1}$ Wm^{-3} during springs.

Residual flow was found to rise with tidal range reaching ~ 0.2 m.s^{-1}. The local character of the residual flow and its proven direct dependence on the magnitude of tidal forcing is consistent with the tidal rectification definition proposed by Robinson (1983).

The seasonal temperature cycle in Maputo Bay shows a peak in heat flux ~50 days

before the summer solstice and the equal heat storage lead in relation to the summer equinox. The bay averaged temperature ranges from 28 °C on 28/03/2003 to 20 °C on 28/07/2004. The smaller heat storage capacity in the bay results in a difference in temperature between shelf and the bay which reaches a maximum of ~0.9 °C, setting a horizontal temperature gradient between these regions.

Towards the end of the wet season the salinity in Maputo Bay was observed to fall as low as 2 PSU below the salinity of the adjacent ocean. The bay averaged salinity ranges from 35.7 PSU in day 343 to 33.5 in day 450. During early summer episodes of hyper-saline conditions up to 0.5 PSU above the adjacent ocean salinity were found.

Stratification in Maputo Bay follows the salinity cycle reaching a maximum of 80 $J.m^{-3}$ of Φ at neap tides during the wet season, when the freshwater fraction of the bay is near its maximum. Observations show that both surface distributed heat and bay-shelf differential heating were weak contributors to stratification during the dry season. Heat is also a negligible contributor to Φ during the wet season given that maximum heat storage was attained 7 days after the first freshwater inflow.

At spring tides transient stratification was found and a Φ model was used to prove conclusively that this was mainly due to strain-induced periodic stratification, SIPS (Simpson $et\ al.$, 1990) reaching ~10 Jm^3 at the end of the ebb.

During the wet season freshwater contribution to buoyancy exceeds greatly the surface heat input given that maximum heat storage is reached 7 days after the first freshwater pulse.

During the dry season the absence of a conservative tracer such as freshwater prevented an observational based calculation of flushing time. However, the Delf3D-Flow platform was considered robust enough for this calculation in dry conditions, yielding a flushing time of ~ 40 – 160 days for spring and neap tides respectively.

During the wet season no conclusive results were found for flushing time, given that the Delft3D-Flow model failed to simulate the dynamics accurately in the presence of freshwater and that the modified tidal prism (MTP) model portrayed the recovering of salinity to shelf values faster than observed. The results for the wet season mean flushing time were 9 – 17 days and ~ 50 days for the MTP and Delft3D-Flow model respectively.

The main control of exchange during the dry season is tidal forcing mainly through rectified currents that increase in direct proportion to tidal range.

During the wet season, tidal forcing and estuarine circulation control exchange. These controls generate a neap to spring cycle in the efficiency of exchange, which varies inversely with the strength of the tide.

9.2   Controls on exchange

Due to the instrumentation limitations, there were no direct measurements of exchange across the mouth of the bay, such as significant number of current meter moorings or cross-sections of towed ADCP (Acoustic Doppler Current Profiler) profiles. Hence, the dynamics of exchange are inferred from the character of residual velocity at a single location at the mouth and from theoretical and empirical relations between the evolution of the density field and the nature of the flow.

9.2.1 Dry season

During the dry season, observational evidence shows that tidal range is the only candidate forcing mechanism significantly correlated with residual flow. This MS_f constituent of velocity is not mirrored by subtidal elevation and does not lag significantly with tidal range. Furthermore, there is no evidence of fortnightly imposed slopes from the shelf, implying that this neap to spring cycle of residual circulation is locally produced.

Tidally rectified flows are approached by Zimmerman (1980), Robinson (1983) and more recently by Li and O'Donnell (1997). As in Speer and Aubrey (1985), these authors argue that the interaction between a rapidly varying bathymetry and tidal currents give way to residual circulation due to the non-linear terms in the equations of movement, with particular relevance to the quadratic bottom friction term. Li and O'Donnell (1997), use a rectangular model of a tidal embayment with triangular cross-section to investigate the generation of residual currents by tidal forcing. Their depth-averaged formulation yields three residual velocity terms: i) an landward Stokes flux arisen from quadratic friction which generates the partially progressive character of the tide; ii) a pressure gradient due to setup at the head of the embayment cause by the Stokes flux; iii) and a weak momentum advection term that is considered negligible. They show that the depth dependence of these terms drives an organised residual circulation pattern proportional to tidal forcing. The depth-averaged quadratic friction term is more important in shallow water, increasing in the shoals the inland Stokes flux term. In the deeper part of the cross-section the weaker influence of the Stokes flux and of the depth-averaged bottom friction, allows the flow, caused by the inland setup, to return to the mouth. This will drive a residual gyre solely due to bottom friction and cross-sectional varying depth. Although their analytical solution is derived from a simple geometry configuration Li and O'Donnell (1997) argue that these three terms will always be present in complex topographies.

In Maputo Bay there was no significant evidence of an along bay slope. Furthermore, tidally induced residual circulation predicted by Delft3D-Flow and partially observed in the field shows inflow through the deep channel and outflow in the shoals. This opposes the results obtained by Li and O'Donnell (1997). The topography of Maputo Bay is far from the idealised setup by Li and O'Donnell (1997) so that the three rectification terms will assume different proportions at specific locations in the bay, thus generating a complex residual flow field resultant from the adjustment of the

pressure field to locally varying depth-averaged bottom friction and Stokes flux.

An additional candidate control on exchange during the dry season is tidal shear diffusion. The observational programme did not provide direct measurement of the tidal shear diffusion coefficient, usually inferred from the observed evolution of a dye patch, but something can be learned from the modelling exercises. Given that the Delft3-Flow simulations represented satisfactory tidal and subtidal features of the flow during dry season, it is reasonable to assume that flushing times they predict for dry season conditions are of the same order as the ones occurring in field. However, the two mechanism promoting exchange from tidal related terms are, as when using observational data, bundled together in the Delft3D-Flow simulation. A conclusive proof that tidal shear diffusion plays a modest role in controlling flushing time and hence the exchange regime in dry conditions comes from the diffusive box model presented in Section 8.3. Even when using the realistic upper bound value for vertical velocity shear, the diffusive model yields flushing times larger than 160 days when the Delf3D-Flow simulation predicts ~50 days. Hence, the numerical model is attributing a large portion of exchange to tidal rectification, either through organised advection or, in conjunction with tidal velocity, through chaotic dispersion as referred in Ridderinkhof and Zimmerman (1992).

It is therefore reasonable to conclude that the main control of exchange during the dry season is tidal forcing mainly through rectified currents that increase in direct proportion to tidal range.

9.2.2 Wet season

In addition to tidal shear diffusion and tidal rectification, during the wet season estuarine circulation is also a candidate exchange mechanism as the salinity in the bay decreases. The current meters at M01 show significant baroclinic response during neap tides once the horizontal density gradient is established. This baroclinicity was

mirrored by the Delft3D-Flow simulation and is consistent with the Linden and Simpson (1986) flume experiments where they found that vertical mixing inhibits the development of density currents and when mixing is switched on and off for equal times, the exchange through a cross-gradient section increases with the period of the mixing cycles.

During spring tides, the observations show transient stratification. In Section 7.1.2, a Φ model was used to prove conclusively that the main term influencing stratification at spring tides is tidal straining of the density field. Tidal stirring and estuarine circulation were shown to play a limited part on the production and erosion of stratification. Estuarine circulation was only present about slack water when N_z was small enough to allow it.

The production and erosion of the density structure by SIPS, when tidal shear acts up or down a density gradient respectively, could be mistakenly taken as a curiosity with no relevance for the exchange regime if the dynamics that accompany this structural change are not taken into account. The model used in Section 7.1.2 when calculating SIPS, makes N_z dependent only on tidal velocity, ignoring its dependence on water column structure. This simplification overlooks the fact that when straining acts to increase water column stratification in SIPS, Ri_E increases and N_z will decrease. Given that estuarine circulation is inhibited by turbulence (Hansen and Rattray, 1965; Linden and Simpson, 1986), a cycle of N_z symmetrical with straining will promote estuarine circulation throughout the ebb, increasing exchange. This will have a positive feedback effect on the stratification. In Stacey *et al.* (2001), a similar explanation is put forward when analysing a pulse like nature of exchange flow, considering this feedback effect an important control on exchange. An effective approach to modelling the relation between straining and estuarine circulation has to include a turbulence closure scheme where N_z is dependent of the evolution of the

density field. Without resorting to a complex 3-dimensional model, a less computer intensive simulation can be performed using a 1-dimensional model such as the one used by Simpson and Sharples (1991) for Liverpool Bay.

During neap tides, the values of Φ, both recorded and modelled, were up to 80 Jm^{-3}, revealing a stable stratification of the water column. However important SIPS is in promoting estuarine circulation at spring tides, it only occurs during part of the cycle. As in the Linden and Simpson (1988) experiments, the Delft3D-Flow *basecase* simulation shows that the estuarine plume is arrested during high mixing at spring tides and that it rapidly spreads offshore forming a coastal density current at neap tides. Unlike tidal shear, the elastic component in this mechanism is small once the plume has extended away from the reach of tidal excursion. In addition to this advection of estuarine water, an equivalent amount of shelf water enters the bay to preserve volume continuity. The Delft3D-Flow experiments show this increase in exchange across the mouth during neap tides. Hence, there is a neap to springs cycle of estuarine circulation modulating the efficiency of exchange in the wet season, which decreases with the amount of tidal forcing.

9.3 Delft3D-Flow performance

The numerical model setup using the Delft3D-Flow software was considered calibrated to the first degree when it showed to represent satisfactory tidal motion and dissipation. This was achieved by increasing the bottom roughness parameter above the usually applied for environments such as Maputo Bay to match the energy flux obtained from observations.

Throughout this dissertation the Delf3D-Flow simulations were compared to observations to assert its ability to reproduce the main features of the system dynamics. The model was capable of reproducing satisfactory the dry season regime at tidal and subtidal frequencies of such features as tidal rectification and shallow

water velocity harmonics. The dry season results were consistent with the 2-dimensional numerical modelling exercise by Canhanga and Dias (2005).

The tuning of bottom roughness improved the relation between water level and velocity. However, its increase led to the overestimation of vertical mixing. The model shows over-mixing while failing to represent SIPS at spring tides during the wet season, a clear feature of the observed density structure where straining leads to Φ ~ 10 J.m^{-3}. The maximum Φ predicted by the model under the same conditions was ~ 2 J.m^{-3}. During neap tides, when tidal mixing was subdued, the numerical model was able to represent accurately the average stratification at a representative sampling section.

The overestimation of the wet season mean flushing time by the Delft3D-Flow experiments is most likely due to the overestimation of vertical mixing, preventing the model from reproducing the increase in stratification and the consequent increase in estuarine circulation due to the aforementioned N_z cycle associated with SIPS.

The overestimation of the salinity deficit in the bay, up to ~6 PSU when only ~ 2 PSU were observed, is consistent with the overestimation of flushing time. This artificial storage of freshwater in the bay led to an overestimation of the horizontal density gradient and consequent exaggeration of the estuarine circulation during neap tides as noted in Chapter 6. Added to this, freshwater loss by evaporation was not accounted for since evaporative processes were exclude from the salt mass continuity equation, and used only to account for latent heat loss.

The works of Canhanga and Dias (2005) and IIP (2001), used a 2D approach to the numerical modelling of Maputo Bay. This strategy only simulates correctly the dry period of the season cycle in Maputo Bay given that it is shown throughout this dissertation that the flow during the wet season in Maputo Bay is clearly a three-dimensional problem. In spite of the misrepresentation of the interaction between

stirring and the density field, the present dissertation advances in relation to the previous modelling exercises in identifying the main dynamic forcing of the bay during the wet season and the difficulties involved in their simulation.

9.4 Limitations to the observational work

Several aspects made the analyses of the system dynamics difficult, namely the incomplete gauging of the rivers, the bay-wide CTD sampling carried out only in spring tides, the decaying of the conductivity signal in the moorings and the placement of the M05 top current meter below the pycnocline. Added to the already sparse availability of resources, the vandalism of the inner M01 mooring with the loss of one current meter eliminated any chance of deploying a third mooring and the possibility of one of the Catchement2Coast partners supplying an ADCP never materialised. Furthermore, bureaucratic impediments and the shortness of technical staff plagued the execution of the observational programme, delaying the acquisition of the instruments, their deployment and servicing.

In hindsight and in view of the obstacles encountered, an observational programme in a developing country such as the present day Mozambique should be planned taking into account the following:

- Local funds mobilisation and customs will most likely delay import, so that at least one to two months should be given for the import-export process.

- Local instrumentation resources are often limited and poorly serviced so that project partners should be prepared to supplement the instrumentation pool with their own instruments.

- Long-term deployments should be minimised and resources placed on frequent sampling with ship-mounted ADCP's and CTD's. In this way, vandalising is minimised and project partners will feel more assured when their instruments

are needed to supplement the local instrumentation pool.

- Technical and scientific staff availability is scarce and often overcommitted. When setting up a new project, local human resources should be recruited in advance and enrolled in skills transfer such as a MSc programme, exposing them to the international scientific community and encouraging the individual to use the project results in their own research.

9.5   Knowledge gaps and future work

In spite of the three different approaches to calculating the flushing time of Maputo Bay, this exchange indicator was not conclusively determined. Flushing time, τ, was defined as the time taken for initial concentration of a passive tracer to drop by a factor of $1/e$. The first approach using a simple modified tidal prism model reproduced a recover of the system's salinity to shelf values that was much too fast in comparison to observed salinity values with $\tau \sim 9 - 17$ days. Despite the high return fraction of bay water, up to $\beta = 0.9$, a model relying only on tidal advection was shown to be too simplistic. The second approach using the Delft3D-Flow platform, while being able to reproduce the dry season dynamics to the known extent, it proved to return wet season values for flushing time that exceeded the ones calculated with the first approach by up to 6 times with $\tau \sim 50$ days. This underestimation of exchange is justified by the vertical over-mixing explained earlier in this chapter. All the discrepancies in the calculation of the flushing time show that this is an explicit spatial problem. This is valid both in the dry season, where bathymetry and flow interact to generate localised residuals, as in the wet season where the 3-dimensional evolution of the density field and the turbulent mixing interact to determine the amount of estuarine circulation present in the neap to spring cycle. The observational work in Maputo Bay was very limited spatially. In future work, the M05 mooring should be maintained to provide temporal continuity, but the relation between the

density field and flow has to be accessed using simultaneous CTD and bottom looking ADCP sampling.

Another region of uncertainty pertains the nature of the atmospheric forcing. During the course of the sampling a diurnal breeze was present in most days together with the resulting sea surface agitation. These short period waves were significant enough to double the time taken to cross the CB section once the afternoon breeze was blowing. Nevertheless, this work found no strong relation between the winds measured at Mavalene airport and the bay dynamics. To overcome the eventuality of significant differences in the atmospheric regime between the airport and the bay, in future work a basic weather station should be placed in the existent large navigation signalling platform in the middle of the bay. As for remote atmospheric forcing, there was an attempt to use QuickScat data but daily instantaneous sampling provided by the instrument was found insufficient to produce a meaningful series. The deployment of an offshore weather boy would overcome this difficulty and would provide further insight into remote forcing mechanisms.

One of the possible responses to offshore imposed slopes was found in the ~ 10 day period oscillation of surface elevation. An eventual forcing by coastal trapped waves (CTW) was discarded as the Agulhas Current seems to damp the northward propagating CTW north of Durban (Goschen and Schuman, 1990; Shuman and Brink, 1990; Brink, 1990). Another possible source of offshore forcing is the well documented Delagoa Bight Eddy (DBE). This feature has a relatively stable position and can have up to ~ 1 m of amplitude variation in a monthly timescale (Lutjeharms and Jorge da Silva, 1988; Grundlingh et. al., 1991; Quartly and Srokosz, 2004). In future studies satellite altimetry can be used to compare the oscillations of the DBE with the data from tide gauges deployed in Maputo Bay.

References

Bendat, J. S. and A. G. Pierson (1986). Random Data. New York, Wiley & Sons.

BHP, Billiton Aluminium (2003). Mozal Expansion Project Produces First Aluminium.
http://www.bhpbilliton.com/bb/investorsMedia/news/2003/mozalExpansionProjectPr
oducesFirstAluminium.jsp. (15/08/2007)

Bos, K. J., J. A. Roelvink and M. W. Dingemans (1996). Modelling the impact of detached breakwaters on the coast. 25th International Conference on Coastal Engineering., Orlando, USA.

Bowden, K. F. (1953). Note on wind drift in a channel in the presence of tidal currents. *Proceedings of the Royal Society of London* **A219**: 426-446.

Bowden, K. F. and L. A. Fairbairn (1952). A determination of the frictional forces in a tidal current. *Proceedings of the Royal Society of London* **A212**: 371-392.

Brink, K. H. (1990). On the Damping of Free Coastal-Trapped Waves. *Journal of Physical Oceanography* **20**(8): 1219-1225.

Canhanga, S. and J. M. Dias (2005). Tidal characteristics of Maputo Bay, Mozambique. *Journal of Marine Systems* **58**: 83-97.

Chao, S.-Y. (1990). Tidal modulation of estuarine plumes. *Journal of Physical Oceanography* **20**(7): 1115-1123.

Cooper, J. A. G. and O. H. Pilkey (2002). The Barrier Islands of Southern Mozambique. *Journal of Coastal Research*(Special Issue 36): 164-172.

de Booer, W. F. (2002). The rise and fall of the mangrove forests in Maputo Bay, Mozambique. *Wetlands Ecology and Management* **10**: 313-322.

de Booer, W. F., L. Rydberg and F. V. Saide (2000). Tides, tidal currents and their effects on the intertidal ecosystem of the southern bay, Inhaca Island, Mozambique. *Hydrobiologia* **428**: 187-196.

Dyer, K. R. (1973). Estuaries: A Physical Introduction. London, Wiley.

FCO, Foreign and Commonwealth Office (2007). Country Profiles, Mozambique.
http://www.fco.gov.uk/servlet/Front?pagename=OpenMarket/Xcelerate/ShowPage&c
=Page&cid=1007029394365&a=KCountryProfile&aid=1019744977697.
(23/10/2007)

Fisher, H. B., E. J. List, R. C. Y. Koh, J. Imberger and N. H. Brooks (1979). Mixing in Inland and Coastal Waters. New York, Academic Press.

Fujiwara, T., L. P. Sanford, K. Nakatsuji and Y. Sugiyama (1997). Anti-cyclonic circulation driven by the estuarine circulation in a gulf type ROFI. *Journal of Marine Systems* **12**: 1-4.

Gill, A. E. (1982). Atmosphere-ocean dynamics. San Diego, CA, USA, Academic Press.

Goschen, W. S. and E. H. Schumann (1990). Agulhas Current Variability and Inshore Structures Off the Cape Province, South-Africa. *Journal of Geophysical Research-Oceans* **95**(C1): 667-678.

Gründlingh, M. L., R. A. Carter and R. C. Stanton (1991). Circulation and water properties of the southwest Indian Ocean, Spring 1987. *Progress in Oceanography* **28**: 305-342.

Hansen, D. V. and M. Rattray (1965). Gravitational Circulation in Straits and Estuaries. *Journal of marine research* **23**(2): 104-122.

Hill, A. E. (1994). Fortnightly Tides in a Lagoon with Variable Choking. *Estuarine Coastal and Shelf Science* **38**(4): 423-434.

Hoguane, A. M. (1996). Hydrodynamics, temperature and salinity in mangrove swamps in Mozambique. PhD Thesis. University of Wales, Bangor. UK

Hoguane, A. M., A. E. Hill, J. H. Simpson and D. G. Bowers (1999). Diurnal and Tidal Variation of Temperature and Salinity in the Ponta Rasa Mangrove Swamp, Mozambique. *Estuarine, Coastal and Shelf Science* **49**(2): 251-264.

Howarth, M. J. and D. T. Pugh (1983). Observations of tides over the continental shelf of North-West Europe. Physical Oceanography of Coastal and Shelf Seas. B. Johns. Amsterdam, Elsevier. **35:** 135-188.

IIP (2001). Sistema de modelos matemáticos para a gestão integrada da Baía de Maputo. Maputo, IIP.

James, I. D. (1997). A numerical model of the development of anticyclonic circulation in a gulf-type region of freshwater influence. *Continental Shelf Research* **17**(14): 1803-1816.

Kalnay, E., M. Kanamitsu, R. Kistler, W. Collins, D. Deaven, L. Gandin, M. Iredell, S. Saha, G. White, J. Woollen, Y. Zhu, M. Chelliah, W. Ebisuzaki, W. Higgins, J. Janowiak, K. C. Mo, C. Ropelewski, J. Wang, A. Leetmaa, R. Reynolds, R. Jenne and D. Joseph (1996). The NCEP/NCAR 40-year reanalysis project. *Bulletin of the American Meteorological Society* **77**(3): 437-471.

Kjerfve, B. and K. E. Magill (1989). Geographic and Hydrodynamic Characteristics of Shallow Coastal Lagoons. *Marine Geology* **88**(3-4): 187-199.

Lencart e Silva, J. D. (2001). Exchange processes between the Atlantic Ocean and the Ria Formosa coastal lagoon, Portugal. MSc Thesis. University of Wales, Bangor. Bangor, UK.

Lesser, G. R., J. A. Roelvink, J. A. T. M. van Kester and G. S. Stelling (2004). Development and validation of a three-dimensional morphological model. *Coastal Engineering* **51**: 883-915.

Li, C. Y. and J. O'Donnell (1997). Tidally driven residual circulation in shallow estuaries with lateral depth variation. *Journal of Geophysical Research-Oceans* **102**(C13): 27915-27929.

Linden, P. F. and J. E. Simpson (1988). Modulated mixing and frontogenesis in shallow seas and estuaries. *Continental shelf research* **8**(10): 1107-1127.

Lutjeharms, J. R. E. and A. J. d. Silva (1988). The Delagoa Bight eddy. *Deep-Sea Research* **35**(4): 619-634.

Monteiro, P. and S. Matthews (2003). Catchement2Coast: making the link between coastal resource variability and river inputs. *South African Journal of Science* **99**: 299-301.

Mussa, A., J. A. Mugabe, F. M. Cuamba and S. Haldorsen (2003). Late Weichselian to Holocene evolution of the Maputo Bay, Mozambique. XVI International INQUA Congress, Reno, USA.

Nicholson, J., I. Broker, J. A. Roelvink, D. Price, J. M. Tonguy and L. Moreno (1997). Intercomparison of coastal area morphodynamic models. *Coastal Engineering* **31**: 97-123.

Nikuradse, J. (1932). Gesetmassigkeiten der turbulente stomung in glatten rohren. *Ver.Deut. Ing. Forschungsheft* **356**.

Officer, C. B. (1976). Physical oceanography of estuaries (and associated coastal waters). New York, Wiley.

Pacanowski, R. C. and S. G. H. Philander (1981). Parameterization of Vertical Mixing in Numerical-Models of Tropical Oceans. *Journal of Physical Oceanography* **11**(11): 1443-1451.

Pingree, R. D. and D. K. Griffiths (1979). Sand transport paths around the British Isles resulting from MS2 and MS4 tidal interactions. *Journal of Marine Biological Association, UK* **59**(2): 407-513.

Pugh, D. T. (1987). Tides, surges, and mean sea-level. Chichester ; New York, J. Wiley.

Quartly, G. D. and M. A. Srokosz (2004). Eddies in the southern Mozambique Channel. *Deep-Sea Research* **51**: 69–83.

Ridderinkhof, H. and J. T. F. Zimmerman (1992). Chaotic Stirring in a Tidal System. *Science* **258**(5085): 1107-1111.

Roberts, R., Maputo Port (2007). Maputo Port operations info. Personal e-mail. (10/09/2007)

Robinson, I. S. (1983). Tidally induces residual flows. Physical Oceanography of Coastal and Shelf Seas. B. Johns. Amsterdam, Elsevier: 321-356.

Saide, F. V. (1995). Tidal Currents in Maputo Bay. Nansen Courses in Environmental Physics. T. Gammelsrød. Nansen Courses in Environmental Physics, Institute of Marine Research.

Schumann, E. H. and K. H. Brink (1990). Coastal-Trapped Waves Off the Coast of South-Africa - Generation, Propagation and Current Structures. *Journal of Physical Oceanography* **20**(8): 1206-1218.

Sete, C., J. Ruby and V. F. Dove (2002). Seasonal Variation of Tides, Currents, Salinity and Temperature Along the Coast of Mozambique. Maputo, CENADO: 72.

Simpson, J. H. (1997). Physical processes in the ROFI regime. *Journal of Marine Systems* **12**: 1-4.

Simpson, J. H., C. M. Allen and N. C. G. Morris (1978). Fronts on Continental-Shelf. *Journal of Geophysical Research-Oceans and Atmospheres* **83**(C9): 4607-4614.

Simpson, J. H. and D. Bowers (1981). Models of Stratification and Frontal Movement in Shelf Seas. *Deep-Sea Research* **28**(7A): 727-738.

Simpson, J. H. and D. Bowers (1984). The role of tidal stirring in controlling the seasonal heat cycle in shelf seas. *Annals of Geophysics* **2**(6): 411-416.

Simpson, J. H., J. Brown, J. Matthews and G. Allen (1990). Tidal straining, density currents, and stirring in the control of estuarine stratification. *Estuaries* **13**(2): 125-132.

Simpson, J. H. and J. R. Hunter (1974). Fronts in the Irish Sea. *Nature* **250**: 404-406.

Simpson, J. H. and J. Sharples (1991). Dynamically-active models in prediction of estuarine stratification. Dynamics and Exchange in Estuaries and Coastal Zone. D. Prandle. Washington, D.C., AGU. **40:** 101-113.

Simpson, J. H., J. Sharples and T. P. Rippeth (1991). A Prescriptive Model of Stratification Induced by Fresh-Water Runoff. *Estuarine Coastal and Shelf Science* **33**(1): 23-35.

Speer, P. E. and D. V. Aubrey (1985). A study of non-linear tidal propagation in shallow inlet/estuarine systems. Part II: theory. *Estuarine Coastal and Shelf Science* **21**: 205-224.

Stacey, M. T., J. R. Burau and S. G. Monismith (2001). Creation of residual flows in a partially stratified estuary. *Journal of Geophysical Research-Oceans* **106**(C8): 17013-17037.

Swallow, J., M. Fieux and F. Schott (1988). The boundary currents east and north of Madagascar 1. Geostrophic currents and transports. *Journal of Geophysical Research-Oceans* **93**: 4951-4962.

UNESCO (1981). Tenth report of the joint panel on oceanographic tables and standards. UNESCO Technical Papers in Marine Science No. 36. Paris, UNESCO.

UNESCO-WWAP (2006). The 2nd United Nations World Water Development Report "Water, a shared responsibility". Mexico City, The 4th World Water Forum.

Vaz, Á. C. and P. v. d. Zaag (2003). Sharing the Incomati waters: cooperation and competition in the balance. *Water Policy* **5**(4): 349-368.

WL|Delft-Hydraulics (1996). Delft3D-FLOW User Manual Version 3.05. Delft, Netherlands, WL|Delft Hydraulics.

Zimmerman, J. T. F. (1980). Vorticity Transfer by Tidal Currents over an Irregular Topography. *Journal of Marine Research* **38**(4): 601-630.

Annex 1 – Station positions

Table A1 – Geographic coordinate of station positions

Station Name	Station position	
	Lon (dec °)	Lat (dec °)
A1	32.5317	-25.9617
A2	32.5917	-25.9900
A3	32.6333	-25.9900
A4	32.6833	-25.9900
A5	32.7333	-25.9900
A6	32.8100	-25.9900
A7	32.8817	-25.9900
B1	32.6750	-25.9250
B2	32.6833	-25.9500
B3 (A4)	32.6833	-25.9900
B4	32.6833	-26.0033
B5	32.6867	-26.0833
B7	32.6833	-26.1167
C3	32.7667	-26.0083
C2	32.7667	-25.9667
C1	32.7667	-25.9250
CB1	32.8864	-25.9508
CB2	32.8625	-25.9351
CB3	32.8275	-25.9059
CB4	32.8001	-25.8897
CB5	32.7527	-25.8673
TG1	32.6000	-25.9800
TG2	32.8969	-26.0383
M01	32.6818	-25.9535
M05 (1)	32.8786	-25.9349
M05 (2)	32.8587	-25.9245

Annex 2 – Instrument specifications

Table A2.1 – Aanderaa RCM9 MkII Current Meter

Parameter	Sensor Type	Range	Resolution	Accuracy
Current speed	Doppler current sensor	0 - 3 ms^{-1}	3x10^{-4} ms^{-1}	1%
Direction	Magnetic compass		0.35°	5° - 7.5°
Temperature	Thermistor	9.81°-36.66°	2.7x10^{-3}°	0.05°
Conductivity (mS.cm-1)	Inductive cell	0-74	7.5x10^{-3}	15x10^{-3}
Pressure	Sillicon piezoresistive bridge	0-700 kPa	0.07 kPa	1.75 kPa
Sampling	Sampling frequency	2 Hz		
	Averaging interval	10 minutes		
	Sampling interval	10 minutes		

Table A2.2 – Hydrotide Recording Tide Gauge

Sensor	Semiconductor strain gauge with atmospheric venting
Range	0 - 10 m
Resolution	0.0015% of range
Accuracy	0.025% of range
Clock accuracy	± 1 s.year^{-1}
Sampling frequency	4Hz burst
Averaging interval	10 s
Sampling interval	10 minutes
	22000 records (138 with 10 minutes sampling
Endurance	interval)

Table A2.3 – SBE 19plus CTD

Parameter	Measurement Range	Initial Accuracy	Typical Stability	Resolution
Conductivity (S/m)	0 - 9	0.05%	0.03%	0.005%
Temperature (°C)	-5 to +35	0.5%	0.0002 °C.month^{-1}	0.01%
Pressure Strain Gauge	0 - 60 m	0.1% of range	0.1% range.year^{-1}	0.002% of range
Sampling	Sampling mode	Profiling		
	Sampling frequency	4 Hz		
	Pump delay	40 s		

Annex 3 – Delft3D modelling specifications
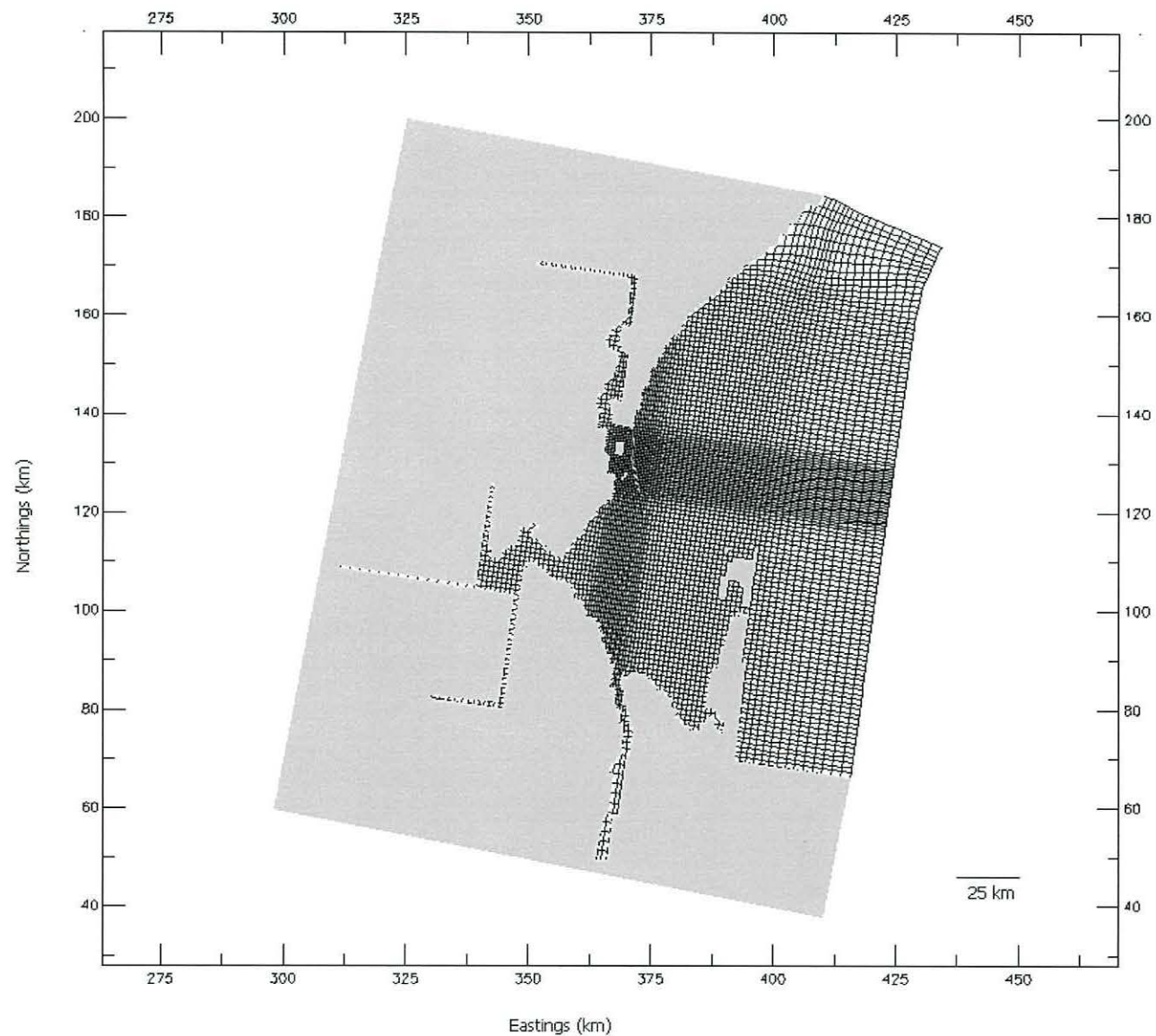
Figure G – Grid for the full Delf3D modelling domain
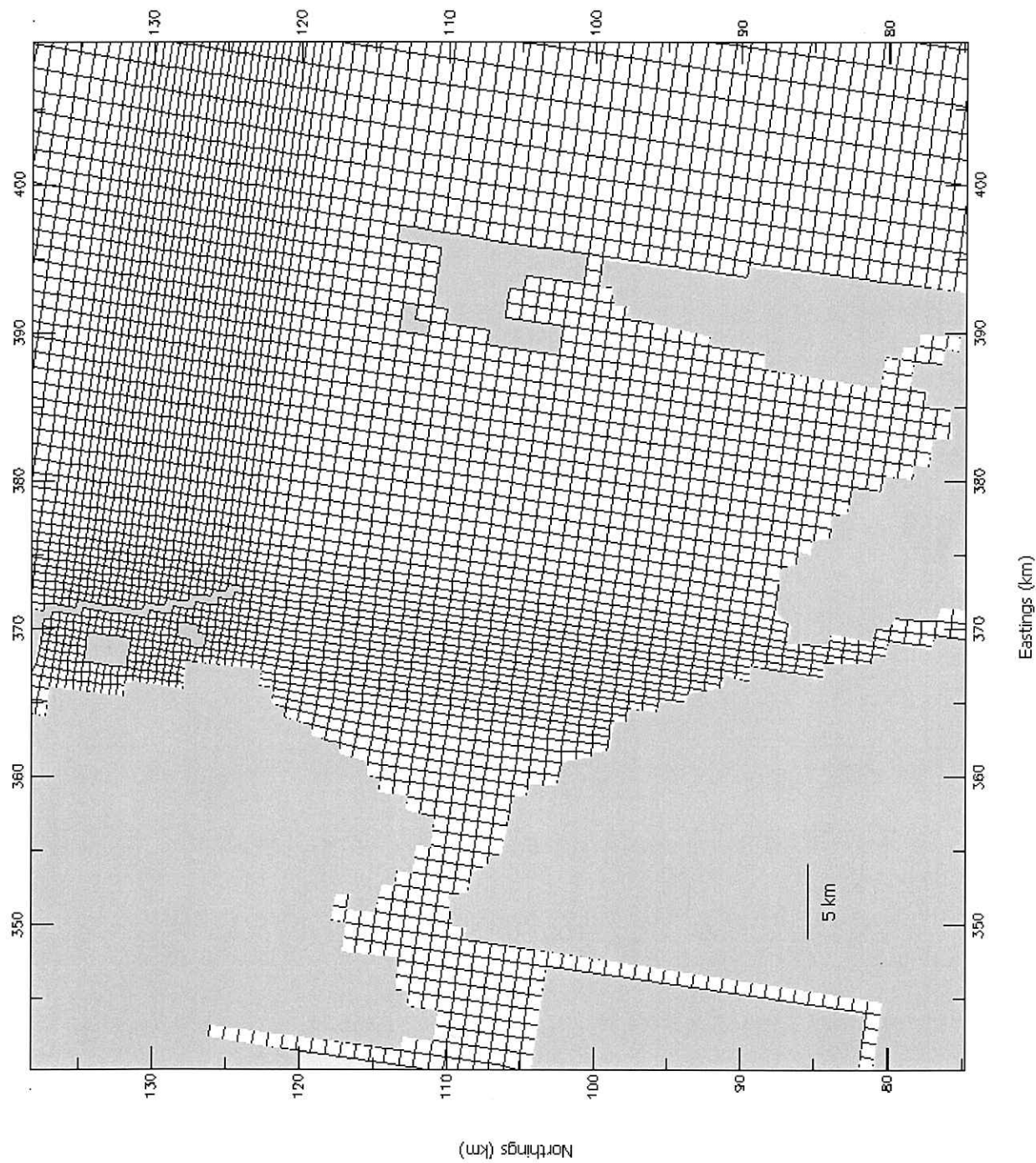
Annex 3 – Delft3D modelling specifications

Controls on Exchange in a Subtropical Tidal Embayment

Figure H – Delft3D grid detail for Maputo Bay.Table E – Common specification for all Delf3D modelling runs.

Table F – Delft3D modelling specifications common to all runs

Layers: 5 sigma (bottom following) layers equally spaced
Timestep: 5 minutes
Constituents: Salinity, Temperature, Passive Tracer
Wind: No
Waves: No
Initial conditions: Hot start from 3 month long run in dry conditions
Boundary forcing: Water levels forced by harmic constituents adapted from TG1
Reflection parameter alpha: 100
Bottom roughness method: 0.15 White-Colebrook Uniform
Wall slip condition: free
Background Horizontal eddy viscosity/diffusivity: 10 m2s-1
Background Vertical eddy viscosity/diffusivity: 0 m2s-1
Turbulence closure: k-Epsilon
Drying and flooding Threshold: 0.1 m
Temperature: From heat flux model
Heat flux model: Absolute flux, net solar radiation

Table G – Diagnostic runs specifications

Run nº	Name	Index	Notes	Duration (days)	Incomati Flow Value (m³s⁻¹)	Incomati Flow Duration (days)	Maputo Flow Value (m³s⁻¹)	Maputo Flow Duration (days)	Wind Value (ms⁻¹)	Wind Duration	Tide
1	Dry steady	D11		31	-	-	-	-	-	-	Full Harmonics
2	Wet steady	D12		31	600	first 15 (1st -15th 03)	400	first 15 (1-15th 03)	-	-	Full Harmonics
3a		D13	Incomati ST	31	1000	3 (8th -10th 03)	-	-	-	-	Full Harmonics
3b		D14	Incomati NT	31	1000	3 (1st - 3rd 03)	-	-	-	-	Full Harmonics
3a2		D23	Incomati ST	31	3000	3 (8th -10th 03)	-	-	-	-	Full Harmonics
3b2	Pulse FW	D24	Incomati NT	31	3000	3 (1st - 3rd 03)	-	-	-	-	Full Harmonics
3c		D15	Maputo ST	31	-	-	3000	3 (8th - 10th 03)	-	-	Full Harmonics
3d		D16	Maputo NT	31	-	-	3000	3 (1st - 3rd 03)	-	-	Full Harmonics
4a	Wind Steady	D17	NE	31	-	-	-	-	10	first 20 days	Full Harmonics
4b		D18	SE	31	-	-	-	-	10	first 20 days	Full Harmonics
5	Wind Diurnal	D19	NE	31	-	-	-	-	10	1200 to 2100	Full Harmonics

Table H – Flushing time experiment specifications

Run nº	Name	Index	Duration (days)	Incomati Flow Value (m^3s^{-1})	Incomati Flow Duration (days)	Maputo Flow Value (m^3s^{-1})	Maputo Flow Duration (days)	Tidal velocity Amplitude (ms^{-1})	Tidal velocity Const.	Wind (ms^{-1})
6		R01	20	0	-	0	-	0.05	M_2	0
7		R02	20	0	-	0	-	0.25	M_2	0
8		R03	20	0	-	0	-	0.65	M_2	0
9		R04	20	0	-	0	-	1.05	M_2	0
10		R05	20	120	20	80	20	0.05	M_2	0
11		R06	20	120	20	80	20	0.25	M_2	0
12	Flushing	R07	20	120	20	80	20	0.65	M_2	0
13	Time	R08	20	120	20	80	20	1.05	M_2	0
14	Modelling	R09	20	480	20	320	20	0.05	M_2	0
15		R10	20	480	20	320	20	0.25	M_2	0
16		R11	20	480	20	320	20	0.65	M_2	0
17		R12	20	480	20	320	20	1.05	M_2	0
18		R13	20	1920	20-	1280	20	0.05	M_2	0
19		R14	20	1920	20-	1280	20	0.25	M_2	0
20		R15	20	1920	20-	1280	20	0.65	M_2	0
21		R16	20	1920	20-	1280	20	1.05	M_2	0